Stability and Decomposition Kinetics of Alloyed Perovskite Semiconductors for Next-Generation Photovoltaics

Spencer G. Cira

A dissertation
submitted in partial fulfillment of the
requirements for the degree of

Doctor of Philosophy

University of Washington

2025

Reading Committee:

Hugh W. Hillhouse, Chair

J. Devin MacKenzie

David S. Bergsman

Cody W. Schlenker

Program Authorized to Offer Degree:

Chemical Engineering

University of Washington

Abstract

Stability and Decomposition Kinetics of Alloyed Perovskite Semiconductors for Next-Generation Photovoltaics

Spencer G. Cira

Chair of the Supervisory Committee:

Hugh W. Hillhouse
Chemical Engineering

Organic-inorganic metal halide perovskite semiconductors have captured the attention of the global scientific community for the past decade plus due to their excellent optoelectronic characteristics and ease of fabrication. These characteristics make them promising for application in low-cost, high efficiency solar cells. Despite their many favorable characteristics, the inherent instability of halide perovskites remains a significant hurdle that presently inhibits their commercialization. Although much work has been done to gain insight into stability of the most promising perovskite compositions, a comprehensive understanding of the chemical reaction landscape that governs decomposition has not been fully elucidated. The work presented here is focused on measuring and modeling decomposition reactions and, where appropriate, linking them to declines in relevant physical properties.

First, I study the decomposition of $FA_{0.8}Cs_{0.2}Pb(I_{0.83}Br_{0.17})_3$, a promising composition for application in perovskite-on-silicon tandem solar cells, under combined light and heat stress. These conditions represent the limiting case of a well encapsulated solar cell, and thus, such tests probe the most basic hurdles that a viable absorber layer material must pass for photovoltaic applications. Through combined structural and optical characterization, we find that films degrade rapidly under illumination in an inert N_2 environment, with notable generation of reduced lead species. Using *in situ* measurements of ambipolar diffusion length and photoluminescence, I show that film optoelectronic degradation is altered when oxygen is present in the ambient at sufficient concentrations. I then measure the kinetics of reduced lead species formation with *in situ* sub bandgap absorption measurements and model the observed kinetics.

Next, I extend the kinetic studies of $FA_{0.8}Cs_{0.2}Pb(I_{0.83}Br_{0.17})_3$ thin films to the photooxidation regime. Under ambient conditions in which the partial pressure of oxygen is >3 kPa, photooxidation decomposition dominates. *In situ* above bandgap absorbance measurements reveal two dominant modes of photooxidation: dry-photooxidation and water-accelerated photooxidation. Interestingly, the presence of water vapor in the ambient is found to increase the rate (posited and modeled to be via water-accelerated photooxidation) at lower temperatures but decreases the rate (posited and modeled to be the result of hydrate formation) at higher temperatures compared to dry conditions. I then derive a rate expression and fit relevant parameters for the three processes assumed to be at play: dry-photooxidation, water-accelerated photooxidation, and hydrate formation. The derived model fits the data well across a range of conditions (<15% median error).

Finally, I consider the effects that varied bromide X-site concentration has on stability, an important lever for tuning the bandgap of halide perovskites. I find that, under combined light and

heat stress, the rate of increase of sub bandgap absorption, an indicator of reduced lead species formation, is faster in compositions with greater X-site bromine concentration. This finding is correlated with *in situ* measurements of ambipolar diffusion length during light heat stress. I also test the stability of the films in the presence of I_2 vapor, a known byproduct of light induced decomposition and photooxidation, finding that the inverse is true: higher bromide fractions impart greater stability.

Collectively, the work included in this dissertation demonstrates significant progress toward the understanding of the full decomposition landscape of alloyed lead halide perovskites.

TABLE OF CONTENTS

LIST OF FIGURES

LIST OF TABLES

ACKNOWLEDGEMENTS

I am very grateful and feel quite lucky to have had such a great support network of friends, family, colleagues, and mentors to rely on during my Ph.D. journey. I would like to acknowledge many of those who have supported me and helped make this accomplishment possible.

I am incredibly indebted to my advisor, Dr. Hugh W. Hillhouse, for his outstanding support of my growth as a scientist and as a person. Dr. Hillhouse sets a high standard for all his students, and it was a privilege to learn under his guidance. I would not be the scientist I am today if it weren't for his guidance and belief in me. I am especially appreciative of Dr. Hillhouse's deep curiosity about the broader aspects of life that inspire and give purpose to our work. It was always a pleasure to discuss not only science but also the deeper ideas that make our efforts meaningful. Thank you, Dr. Hillhouse.

I would also like to thank the other members of my committee for making themselves available to attend the exams during my PhD. Dr. David Bergsman, Dr. Cody Schlenker, and Dr. Devin Mackenzie, thank you for providing thoughtful feedback and encouragement during my general exam and holding me to a high scholarly standard.

I would also like to acknowledge the many lab mates and collaborators in the Hillhouse group that I was lucky to work alongside. Dr. Wiley A. Dunlap-Shohl, you were instrumental in my progress during the first few months of my PhD and were my first mentor as a PhD student. Your deep curiosity and passion for scientific exploration and discovery are inspiring. Thank you for being a role model for me. Dr. Yuhuan Meng, thank you for holding me to a high standard and for taking part in thoughtful discussions about my work. Your discipline and work ethic always encouraged me to keep at it. Dr. Preetham P. Sunkari, thank you for being a great role model; your

diligent work and presentation skills were always something I looked up to. Dr. Yuhang Yang, thank you creating a nice lab atmosphere and for thoughtful discussions about our work and life. William Heins, thank you for being an excellent student and researcher; the future will no doubt have great things in store for you. Jordi Folch, thank you for being a curious and thoughtful mind.

I also would like to acknowledge the Department of Energy SunShot program, the University of Washington Chemical Engineering Department, and the Clean Energy Institute (via the Washington Research Foundation) for financial support, without which this work would not have been possible.

Lastly, I would like to thank my friends and family who have all been an incredible support network for me.

To my friends in Seattle, Scott Beinlich, Aneesh Deshpande, Adithya Boddhu, Nick Hoyer, Kevin Zhao, Abby Martin, Emily Grossman, and John Landy, thank you all for being such great friends to me. You are all wonderful people, and I deeply appreciate our friendships and the many great memories that I have with each of you. To my partner, Vivien, your immediate support and love has been so wonderful to experience, and I can't wait to see where the next few years take us. I feel incredibly grateful to have you by my side.

To my siblings, Sophia, Sydney, and Samantha, thank you for your words of encouragement and cheering me on the whole way. To my parents, Greg and Jennifer Cira, thank you for everything. You both have put so much into providing for your children, and I know I wouldn't be half the person I am today without all that you have done for me throughout my life.

DEDICATION

This dissertation is dedicated to my parents, Greg and Jennifer. Thank you for providing the endless support and means by which I could pursue my passions and find meaning in my life.

1 Introduction and Motivation

This chapter introduces the motivations underlying this work. The research presented here contributes to the ongoing global transition toward sustainable energy, aiming to shift infrastructure away from incumbent fossil fuels and toward renewable technologies with substantially lower embedded carbon footprints. Among these technologies, next-generation photovoltaics (PV) based on hybrid metal halide perovskite semiconductors have emerged as a focal point of global research and development.

1.1 Historical Context and Impact of Industrialization

The Industrial Revolution marked a profound turning point in human history, driving unprecedented gains in productivity and quality of life.[1] Advances in manufacturing efficiency enabled the transition from an agrarian global society to one dominated by mechanized industry, spurring economic development. This transition, however, did not occur without certain externalities, most notably environmental degradation and societal disruption, that continue to shape global challenges today. This era also marked humanity's increasing dependence on fossil fuels as the dominant energy source, a dependency that persists today and underpins many of the environmental, economic, and geopolitical challenges faced by modern societies.[2]

Many of the acute societal costs associated with early industrialization, including local air pollution creating smog-filled cities, acid rain, and contaminated waterways, have been mitigated.[3,4] Yet, the environmental impacts born from this era tied to fossil fuel dependence have continued and now represent the most significant and enduring legacy of industrial development.[5] Chief among concerns associated with fossil fuel consumption is global warming, driven by the accumulation of greenhouse gases, primarily carbon dioxide, in the atmosphere.[6]

The Earth's climate is governed by a delicate radiative energy balance between incoming solar radiation and outgoing thermal radiation.[7] Greenhouse gases strongly absorb outgoing thermal radiation from Earth in the near infrared ($T_{earth,avg}$~288 K). This absorption increases the optical opacity of the atmosphere in these wavelength regions, reducing the amount of thermal radiation that escapes to space, creating a net positive heat flux and gradual warming of the planet's surface.[8] As global population, industrial activity, and energy demand have expanded, greenhouse gas emissions have continued to rise,[9] elevating their atmospheric concentrations and intensifying anthropogenic climate change.

1.2 The Moral and Practical Imperative

From a moral perspective, humanity bears a clear responsibility to protect and preserve the environment for future generations. Allowing climate change to progress unchecked poses hazards not only to the current generation, through disruptions to ecosystems and economic stability, but especially to future generations who will face compounding climate burdens.[10] There are also compelling near-term practical reasons to decarbonize global energy systems, namely cost.[11] Their widespread adoption can lower energy costs for consumers, enhance national energy security, and reduce dependence on finite and geopolitically sensitive fossil fuel reserves.[6] Such happenings could reduce economic uncertainty and strengthens confidence across sectors.[12]

1.3 The Promise and Challenges of Renewable Energy Technologies

1.3.1 Overview of Major Renewables

A variety of renewable energy technologies are currently employed or under active development, including geothermal, nuclear, solar, hydroelectric, wind, and biomass. The ideal renewable energy source for the modern energy economy should satisfy several key criteria: it

must be scalable, capable of meeting rapidly growing global energy demand, and economically viable, requiring relatively low capital expenditure for deployment and operation.[2]

Among renewable energy technologies, solar photovoltaics (PV), solid-state devices that convert sunlight into electricity, stand out as one of the most promising solutions for large-scale clean energy generation. The solar resource itself is enormous: in roughly one hour, the Earth receives more energy from the Sun than humanity consumes in an entire year.[5] Beyond its abundance, solar power has become increasingly cost-effective, now approaching a levelized cost of electricity (LCOE) of 4 cents per kWh or less, undercutting the cost many traditional generation technologies.[11] LCOE represents the total lifetime cost of producing a unit of electricity, calculated as the sum of capital, operating, transmission, and decommissioning costs divided by the total energy produced over the system's lifetime. Lowering any component of cost, or increasing energy yield, reduces the LCOE, improving economic competitiveness and lowering costs for consumers.

1.3.2 Barriers to Solar Deployment

Large-scale solar PV deployment faces several persistent challenges. First, solar power is inherently intermittent: generation occurs only during daylight hours and fluctuates with weather conditions, requiring energy storage systems to be developed in parallel to ensure reliable, on-demand power delivery compatible with the existing electrical grid.[13] Solar PV installations also require additional electrical hardware, such as inverters for grid integration, and their performance depends strongly on local irradiance, yielding highest efficiency and economic returns in high-insolation regions like the southwestern United States.[14] Finally, the rapid growth of global electricity demand, projected to rise by 3% annually through 2035 and 3.5% annually through 2050,[15] necessitates swift, cost-effective expansion of manufacturing capacity, a challenge that remains a major bottleneck for current PV technologies.

To address these challenges, researchers in the photovoltaic community are developing new thin-film solar architectures that utilize inexpensive, earth-abundant materials and low-temperature fabrication methods.[16] These technologies, named "thin film" for their ability to absorb sunlight efficiently using layers only micrometers thick, offer potential advantages of low capital expenditure and high energy yield. Cadmium telluride (CdTe) photovoltaics have already achieved commercial success, most notably through First Solar in the United States.[17] However, emerging hybrid metal halide perovskite solar cells have demonstrated exceptional power conversion efficiencies, tunable optoelectronic properties, and scalable processing routes, positioning them as a leading candidate for the next generation of high-performance, low-cost photovoltaics.[18]

1.4 Thin Film Photovoltaics as a Scalable Clean Energy Solution

1.4.1 Limitations of Crystalline Silicon PV

Crystalline silicon photovoltaics (c-Si PV) dominate the global market, accounting for over 95% of PV production in 2024**,**[19] and are exceptionally stable, with operational lifetimes exceeding 30 years, a key factor in their bankability and low LCOE. However, achieving high efficiencies requires extremely pure, defect-free silicon, and producing such material involves energy and capital intensive processes (high temperature single crystal growth, precise wafering) driving up the capital expenditure (CapEx) of silicon PV manufacturing.[20] Additionally, silicon PV carries a relatively high embedded carbon footprint, as the energy-intensive upstream processing, particularly in regions with coal-dominated electricity grids, contributes significant greenhouse gas emissions, reducing its overall decarbonization potential compared to thin-film alternatives.[16]

1.4.2 Thin Film PV Advantages

Thin-film photovoltaics, including those based on metal halide perovskite semiconductors, represent a newer generation of solar technologies that are far easier and less expensive to manufacture than crystalline silicon. These materials can be deposited at low temperatures using solution or vapor-based methods, eliminating the need for high-purity crystal growth and lowering capital costs. Many thin films possess direct bandgaps and partial ionic bonding, yielding strong optical absorption and defect tolerance that enable efficient performance despite moderate imperfections.[21] Together, these properties reduce material use and energy input, making thin-film photovoltaics, particularly those based on hybrid metal halide perovskites, among the most promising candidates for scalable, high-efficiency, and low-cost solar modules.

1.5 Why Perovskite Photovoltaics Are Especially Promising

Hybrid organic–inorganic metal halide perovskites represent an exceptional class of semiconductor materials that combine compositional tunability, strong optoelectronic performance, and low-cost processability. These materials adopt the general chemical formula ABX_3, where the A-site is occupied by a monovalent cation, typically cesium (Cs^+), formamidinium (FA^+), methylammonium (MA^+), or rubidium (Rb^+), the B-site by a divalent metal cation such as lead (Pb^{2+}) or tin (Sn^{2+}), and the X-site by halide anions (I^-, Br^-, or Cl^-) (see Fig 1.1). Compositional mixing at any of these three sites allows for fine-tuning of key material properties. Perovskite semiconductors have demonstrated remarkable performance across a range of optoelectronic applications, most notably in photovoltaics, where they are poised to complement or replace existing technologies.[18]

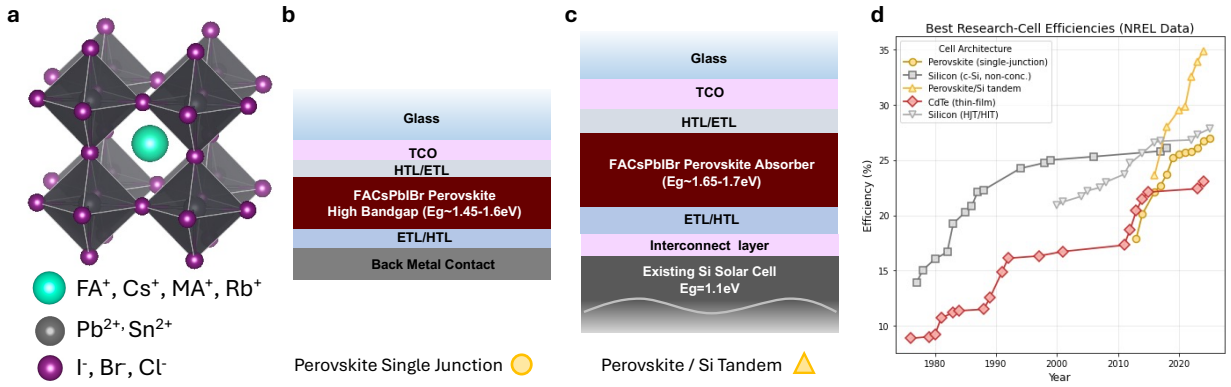

Figure 1.1. **Perovskite solar cells.** (a) Hybrid metal halide perovskite crystal structure. Schematic of solar cell architecture for (b) perovskite single-junction and (c) perovskite/silicon tandem cell. (d) Best research cell efficiency over time for various commercialized (Si, CdTe) and emerging (perovskite SJ, perovskite/Si tandem) solar cell technologies (data retrieved from NREL[22]).

1.5.1 Low Carbon Footprint, Energy Security, and Resource Independence

Among the most compelling advantages of perovskite-based photovoltaics is their potential for a low embedded carbon footprint and minimal environmental impact. The constituent elements are earth-abundant, and device fabrication can occur at low processing temperatures (~100°C), Manufacturing facilities for perovskite solar modules can be established in a wide range of regions with minimal infrastructure investment. This decentralized manufacturing potential reduces dependence on the highly specialized supply chains that currently dominate silicon and other semiconductor industries. In the United States and allied nations, the development of domestic perovskite PV manufacturing capacity could therefore enhance energy security, strengthen local economies, and mitigate reliance on imported solar modules.

1.5.2 Multijunction Perovskite Photovoltaics

Metal halide perovskites exhibit highly tunable electronic and optical properties, with achievable bandgaps ranging approximately from 1.2 eV to 2.3 eV.[23] This broad range encompasses the optimal bandgaps for both single-junction (Fig 1.1b) and multijunction

photovoltaic architectures (Fig 1.1c).[24] In multijunction solar cells, layers of semiconductors with different bandgaps are stacked to absorb complementary portions of the solar spectrum, thereby reducing thermalization losses and increasing overall power-conversion efficiency. Perovskites are especially well-suited for this approach because their bandgap can be precisely engineered through halide or cation substitution. Such perovskite-based tandem devices have already demonstrated efficiencies exceeding the Shockley–Queisser limit for single-junction cells (~33%).

1.5.3 Performance of Perovskite Solar Cells

Laboratory-scale perovskite solar cells have achieved remarkable efficiency gains over the past fifteen years, far outpacing the historical development trajectories of previous photovoltaic technologies (Fig 1.1d). Most halide perovskites are nearly intrinsic semiconductors and thus rely on bulk heterojunction structures in solar cells (either in the p-i-n or n-i-p configuration). As of October 2025, certified single-junction perovskite solar cells have reached power conversion efficiencies approaching 27%, while perovskite–silicon tandem architectures have demonstrated efficiencies nearing 35%.[22] This unprecedented rate of improvement contrasts sharply with the multi-decade timescales typically required for comparable advancements in established photovoltaic systems such as silicon or CdTe.

1.5.4 Stability Concerns Limit Perovskite Photovoltaics Commercialization

Despite their many advantages, metal halide perovskites remain hindered by stability challenges that currently prevent their large-scale commercial deployment.[25] Owing to their predominantly ionic nature, these materials are prone to chemical decomposition reactions and phase transformations under environmental or operational stress, limiting the longevity of the devices they comprise.[26] To date, despite extensive progress in encapsulation and interface engineering, no perovskite photovoltaic modules have demonstrated operational lifetimes

exceeding several years under standard outdoor conditions.[27] Degradation in perovskite devices typically originates from reactions within the perovskite absorber layer itself. These mechanisms are diverse and will be discussed in detail in the experimental sections of this work. Other degradation pathways, including chemical reactions with metallic electrodes, ion migration at interfaces, and mechanical delamination of device layers, also contribute to performance loss.[28] However, the intrinsic stability of the absorber material remains a central determinant of device longevity and is the focus of this dissertation.

1.6 Predicting Solar Cell Lifetime

It is worth briefly discussing how the stability and lifetime of photovoltaic modules are typically assessed. A common metric used across the solar industry is the T80 time, defined as the duration required for a device or module to degrade to 80% of its initial (or peak) power-conversion efficiency under controlled testing conditions. To evaluate long-term performance within practical timeframes, researchers often conduct accelerated aging tests, in which devices are subjected to elevated stressors such as higher temperature, humidity, or illumination intensity. The acceleration factor quantifies how much faster degradation proceeds under these elevated conditions relative to standard operation. By establishing such factors for each dominant stressor, accelerated tests provide a means to infer expected device lifetime from shorter-term experiments.

1.6.1 Empirical Stability Measurements and Predictions

Historically, most studies have relied on empirical stability measurements to predict photovoltaic degradation. In these approaches, performance loss is monitored over time under specific test conditions, and the results are fit with mathematical models, typically exponential or logarithmic functions, to extract degradation rates. These empirical models can describe observed

behavior within the test window and, when combined with acceleration factors, are often extrapolated to estimate field lifetimes.

While useful, such empirical predictions are inherently limited: they treat degradation as a purely phenomenological process and often fail to capture the coupling between environmental variables and the underlying physical or chemical mechanisms of failure. As a result, their extrapolations can lack robustness when applied across diverse climates or device architectures. Importantly, however, the accurate determination of acceleration usually requires multidecade investigation and requirements, putting limitations on consumer confidence for rapidly scaled PV technologies. The learning curve associated with this is best demonstrated by the Jet Propulsion Laboratory's "block buy" program.[29]

1.6.2 Physics and Chemistry Informed Predictions

An emerging and more predictive approach involves physics-informed lifetime modeling, which seeks to describe degradation on the basis of the fundamental physical and chemical processes driving material and device failure. These models integrate mechanistic understanding, such as defect formation, ion migration, and interfacial reactions, into rate expressions that can be parameterized experimentally.[30]

When coupled with accurate climate and operational data (e.g., temperature, humidity, and solar irradiance), physics-informed models can generate geographically specific lifetime projections for photovoltaic modules. For instance, degradation rates often exhibit Arrhenius-type temperature dependence, such that measurements at multiple temperatures can yield an effective activation energy for performance decline and provide a mechanistic basis for temperature-related acceleration factors. Similar frameworks can be applied to degradation processes governed by light-induced or defect-mediated reactions.

Although developing comprehensive physics-informed models remains challenging, owing to the multitude of concurrent degradation pathways, they represent the most robust avenue for achieving predictive reliability in photovoltaic lifetime assessment. Consequently, understanding and quantifying the fundamental degradation mechanisms of perovskite materials is essential for constructing accurate, mechanistically grounded models that can guide the design of stable, long-lived solar technologies.

1.7 Scope and Objectives of This Work

PV modules composed of metal halide perovskite semiconductors represent prime candidates for third-generation commercial photovoltaics. These materials are low-cost, earth-abundant, and readily fabricated into high-efficiency devices using scalable processing methods. However, their stability and durability remain key limitations to widespread commercialization. Beyond engineering and encapsulation improvements, achieving stable perovskite photovoltaics requires a fundamental understanding of the chemical and physical processes that govern material degradation. Elucidating these mechanisms is not only essential for improving intrinsic material stability but also provides the foundation for developing physics and chemistry informed lifetime models capable of predicting long-term performance under real-world conditions.

The goal of this dissertation is to contribute to the growing body of literature on perovskite semiconductors by identifying and quantifying the decomposition pathways and reaction kinetics that dictate their stability. Particular emphasis is placed on the most promising compositions for near-term commercialization in perovskite solar cells, where understanding degradation mechanisms is critical to translating laboratory-scale performance into reliable, long-lived devices. In this chapter, I have provided the background and motivation of this work.

In Chapter 2, I provide an overview of the experimental and analytical methods used throughout this thesis. A materials-science-driven approach is employed to elucidate the chemical and structural changes occurring within perovskite materials under various environmental and operational conditions. These changes are ultimately correlated with device-relevant performance metrics, including quasi-Fermi-level splitting and carrier diffusion length, to establish direct links between material degradation and photovoltaic function.

In Chapter 3, I present a detailed investigation of the light-induced decomposition mechanisms in mixed-cation mixed-halide lead perovskite. The composition studied is representative of those targeted for near-term commercialization in perovskite–silicon tandem architectures, offering an ideal optical bandgap for sub-cell pairing with silicon. Under combined light and thermal stress, we observe the formation of reduced lead species that are detrimental to optoelectronic performance. Optical and structural characterization reveal the emergence of metallic lead at extended degradation times. Furthermore, by quantifying sub-bandgap optical absorption, we model the formation kinetics of these reduced lead species, providing mechanistic insight into the fundamental chemical processes driving perovskite degradation.

In Chapter 4, I extend the kinetic analysis of the representative mixed-cation mixed-halide perovskite to the photooxidation regime, which dominates under appreciable oxygen partial pressures. In this regime, photoexcited electrons are posited to be diverted away from lead reduction pathways and instead drive alternative oxidative decomposition reactions. To investigate these processes, we conduct a comprehensive study of absorber degradation under combined light, heat, oxygen, and water exposure. The resulting kinetic data reveal that three concurrent processes, dry photooxidation, water-accelerated photooxidation, and hydrate formation, govern the decomposition of the perovskite absorber under these conditions. Using elementary step reaction

mechanisms and applying the rate-determining-step approximation, we develop a quantitative model that accurately describes the coupled kinetics of these processes. The model performs well across a broad range of illumination intensities, temperatures, and oxygen and water partial pressures, capturing the essential physics and chemistry that dictate perovskite degradation under realistic operating environments.

In Chapter 5, I extend the analysis introduced in Chapter 3 to examine a broader range of perovskite compositions with systematically varied halide content. As previously discussed, halide perovskites are highly tunable materials, and one of the most effective means of tuning their optoelectronic properties is through bandgap adjustment via halide alloying, typically by varying the relative proportions of iodide and bromide. For photovoltaic applications, such compositional tuning enables optimization of absorption characteristics and energy-level alignment. In this chapter, we find that higher-bromide compositions form reduced lead defects, as quantified through sub-bandgap optical absorption, at faster rates than compositions with lower-bromide content. This compositional dependence correlates with a more rapid decline in carrier diffusion length, suggesting a coupling between halide composition, defect formation kinetics, and charge-transport degradation. We also investigate the response of these materials to iodine vapor (I_2), an important product of both light-induced decomposition and photooxidation and observe that bromine-rich compositions exhibit enhanced resistance to I_2 vapor-induced degradation.

Finally, in Chapter 6, I provide concluding remarks and an outlook on the commercialization prospects of halide perovskite photovoltaics, emphasizing the importance of mechanistic understanding and predictive modeling in enabling stable, scalable solar technologies.

2 Methods

This chapter provides a concise overview of the experimental and analytical methods employed throughout this thesis. While some descriptions may be partially redundant with those presented in later chapters, this section serves as a centralized reference to contextualize the experimental design and provide theoretical background for the key characterization techniques used.

2.1 Solar Cell Operation

A solar cell is a solid-state device that converts sunlight into electrical energy. Its operation relies on the absorption of photons in a semiconductor, the generation of electron-hole pairs, and the subsequent transport and collection of these charge carriers at the electrodes. By doping the semiconductor, or by forming junctions or interfaces with other materials, an internal electric field is established within the device. When light is absorbed and carriers are excited, this built-in field drives electrons and holes (positively charge quasi-particles) toward their respective contacts, producing an electrical current.

When the external circuit is shorted (the electrodes are directly connected), the measured current is the short-circuit current density (J_{sc}). Conversely, when the circuit is open (no current flows), the voltage developed across the contacts is the open-circuit voltage (V_{oc}). Under intermediate load conditions, where the applied voltage lies between 0 and V_{oc}, the solar cell delivers both current and voltage, generating electrical power. The point at which the product of current and voltage is maximized defines the maximum power point (MPP), a key performance metric that determines the overall power conversion efficiency (PCE) of the solar cell.

2.2 Photoluminescence and Quasi-Fermi Level Splitting

An ideal semiconductor for photovoltaic applications should be both an efficient absorber and emitter of light. When a semiconductor absorbs a photon with energy greater than its bandgap, an electron is excited from the valence band to the conduction band, leaving behind a hole. These excited charge carriers can subsequently relax to the ground state through either radiative or nonradiative recombination processes. Photoluminescence (PL) refers to the emission of light that occurs when these excited carriers recombine radiatively. In semiconductors, this process involves three fundamental steps: band-to-band absorption, carrier thermalization, and band-to-band radiative emission. Quantifying the net radiative emission, and analyzing its spectral shape, provides valuable insight into the optoelectronic quality of a semiconductor, most notably through the determination of the quasi-Fermi level splitting (QFLS). In this work, measurements of PL are done with a wide-field PL microscope as well as with a modified confocal microscope, enabling spectrally resolved PL.

In the dark, the carrier populations in a semiconductor can be described by a single Fermi level that defines the equilibrium occupation of both the conduction and valence bands. Under photoexcitation, however, the electron and hole populations depart from equilibrium and are instead described by two distinct energy levels: the quasi-Fermi level for electrons in the conduction band and the quasi-Fermi level for holes in the valence band. The absolute energy difference between these two levels is referred to as the quasi-Fermi level splitting (ΔE_F). Importantly, the QFLS represents the maximum achievable open-circuit voltage of a photovoltaic device comprised of the semiconductor material under steady-state illumination (more strictly, $V_{oc,max} = \Delta E_F/q$) providing a direct measure of the electronic quality and recombination losses.

Thus, accurately assessing the QFLS and its evolution over time under stress is essential for evaluating the optoelectronic quality and stability of absorber materials.

The fraction of absorbed photons that are reemitted radiatively is known as the photoluminescence quantum yield (PLQY). The external PLQY ($PLQY_{ext}$) of a semiconductor film is related to the quasi-Fermi level splitting (QFLS) through the Ross relation[31]: $QFLS_{act} = QFLS_{SQ} + k_B T \ln(PLQY_{ext})$, where $QFLS_{SQ}$ is the Shockley–Queisser (detailed balance) limit of the quasi-Fermi level splitting for an ideal, radiatively limited semiconductor. Measurements of $PLQY_{ext}$, therefore, provide direct insight into the optoelectronic quality and recombination dynamics of the material. Beyond the absolute intensity of emitted photons, the spectral shape and the absolute intensity at each wavelength also provide valuable information about the QFLS and can offer improved accuracy in cases where sub-bandgap absorption is significant.

Our research group, led by Professor Hugh W. Hillhouse, at the University of Washington has previously established a method fitting the full absolute photoluminescence spectrum using a unified model that explicitly accounts for sub-bandgap absorption and emission, a notoriously challenging feature to model accurately. This approach, described in detail by Katahara and Hillhouse,[32] is used in Chapter 3 to quantify the quasi-Fermi level splitting under one-sun illumination. By incorporating sub-bandgap contributions to the emission spectrum, this model provides a more rigorous and accurate estimate of the QFLS than the conventional Ross relation.

2.3 Photoconductivity and Ambipolar Diffusion Length

An ideal photovoltaic absorber must not only absorb and emit light efficiently, indicating the ability to sustain high densities of photoexcited carriers with minimal nonradiative recombination, but must also transport those charges effectively to the device contacts. To assess

the charge transport properties of photovoltaic-grade semiconductors, photoconductivity measurements are commonly employed. Photoconductivity is the net additional conductivity under illumination: $\sigma_{ph} = \sigma_{light} - \sigma_{dark}$. It is related to the charge carrier mobility by the following (in the high injection regime): $\sigma_{ph} = q(\mu_n + \mu_p)\Delta n$. Our group has developed a two-point photoconductivity method for this purpose, enabling quantitative evaluation of carrier transport dynamics under controlled illumination.

For intrinsic semiconductors such as those studied in this thesis, measurements of photoconductivity, when combined with a known carrier generation rate, can be used to quantitatively determine the ambipolar diffusion length, as originally derived by Stoddard:[33] $L_D = \sqrt{\frac{\sigma_{ph} kT}{2q^2 G}}$. This relatively simple two-point photoconductivity technique therefore encodes valuable information about charge-carrier dynamics, providing a direct measure of the material's transport efficiency. The stability of this parameter is critically important, as maintaining a consistent diffusion length over time is essential for achieving long photovoltaic device lifetimes.

2.4 In situ Absorbance Measurements to Determine Chemical Decomposition Rate

While photoluminescence and photoconductivity measurements provide critical insights into the optoelectronic properties of perovskite semiconductors, they offer limited information about changes in chemical composition. To complement these techniques, much of the experimental work presented in this thesis combines optoelectronic characterization with *in situ* optical absorbance measurements to directly monitor the evolution of chemical species during degradation.

The Beer–Lambert law relates a material's absorbance to the quantity of absorbing species along the optical path, expressed as: $Absorbance = \log_{10}(e) \cdot \alpha \cdot l$, where A is the absorbance,

α is the absorption coefficient, and l is the optical path length. By taking the time derivative of absorbance, rearranging, and incorporating the material's physical properties, the rate of chemical decomposition can be expressed as a surface-normalized rate: $rate\ (mol \cdot m^{-2} \cdot s^{-1}) = \frac{\rho \cdot log_e 10}{M \cdot \alpha_o} \frac{dA}{dt}$. This method was originally developed by Siegler et al.[34] to study the decomposition of methylammonium lead triiodide perovskite and later adapted by Meng et al.[35] for investigations of low-bandgap tin perovskites. The same approach is employed extensively in Chapters 3 and 4 to quantify the defect formation kinetics of reduced lead species and the photooxidation reaction kinetics of alloyed lead halide perovskites, respectively.

3 Light Induced Degradation of Mixed Cation Mixed Halide Perovskite: Observed Rates and Influence of Oxygen

This chapter describes experiments undertaken on $FA_{0.8}Cs_{0.2}Pb(I_{0.83}Br_{0.17})_3$ perovskite thin films under combined heat, light, and oxygen stresses. Optical, structural, and charge transport properties are tracked over the course of exposure to these stresses, identifying relevant decomposition products, and linking these products to optoelectronic performance loss. The kinetics of reduced lead species formation, a critical defect in lead halide perovskites, are uncovered using *in situ* sub bandgap absorbance measurements. This chapter was adapted from a publication in the Journal of Materials Chemistry A.[36] Reproduced with permission[36]; Copyright 2025 RSC Publishing.

3.1 Abstract

Formamidinium-rich lead halide perovskite semiconductors comprise the absorber layer in the most efficient single-junction perovskite solar cells (PSCs) but suffer from chemical instability when exposed to high temperatures, moisture, oxygen, and light. Light-induced degradation (LID) is unavoidable in PSCs and can be slowed only by limiting the escape of decomposition products. Here, we study the LID of $FA_{0.8}Cs_{0.2}Pb(I_{0.83}Br_{0.17})_3$ thin films using *in-situ* and *ex-situ* optical spectroscopy, microscopy, and x-ray diffraction. The results reveal that the primary decomposition products under LID conditions are reduced lead-containing species that have broadband optical absorption. XPS reveals the presence of Pb^0, but it may coexist with partially reduced lead-containing species. We use *in-situ* sub-bandgap optical absorbance measurements to selectively probe and quantitatively measure the formation rate of reduced lead species. We derive a rate law for reduced-Pb formation (r_{Pb^0} estimated at ~3x10^{-10} mol/(m^{2}s) at 25 °C in N_2 under 1 sun photon

flux that would result in complete conversion of a 300 nm film in ~78 days), determine an activation energy (~0.61 eV), determine an effective reaction order with respect to the flux of above bandgap photons ($r_{Pb^0} \propto I_{in}^{0.72}$), and find that the wavelength of above bandgap photons minimally affects the rate, suggesting that PbI_2 photolysis is not the mechanism for the formation of decomposition products. These observations represent the first quantitative measurements of the rate of formation of reduced lead species in perovskites and emphasize a unique interplay among environmental stressors and degradation pathways for commercially relevant perovskite materials.

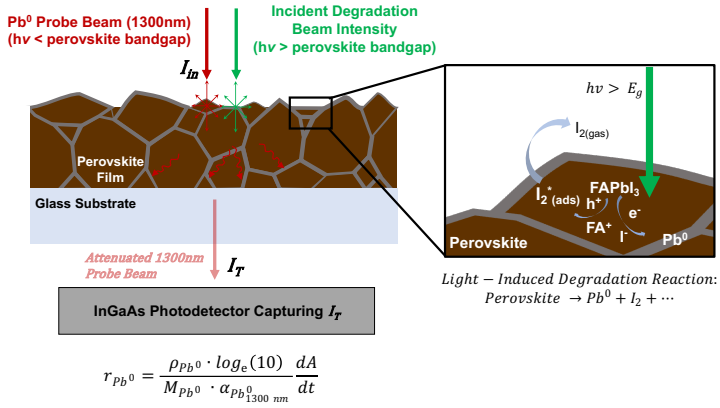

Figure 3.1. **Light Induced Degradation of Mixed Cation Mixed Halide Perovskite: Observed Rates and Influence of Oxygen**

3.2 Introduction

Hybrid organic-inorganic perovskites with the chemical formula ABX_3 are a unique class of semiconductors that exhibit simultaneous ease of fabrication (solution and/or vapor processing[37]) and excellent optoelectronic quality (long diffusion lengths and carrier lifetimes,[38] high absorption coefficients,[39] and tunable bandgap[40]). Perovskite single-junction and perovskite-on-silicon tandem photovoltaic (PV) cells have achieved 26.7% and 34.6% power conversion efficiency[41], respectively, as of December 2024. Despite their high defect concentration (~10^{15}-

10^{16} cm^{-3}) compared to conventional covalent semiconductors such as c-Si or GaAs (<10^{12} cm^{-3}),[42–44] the ionic nature of halide perovskites causes most of the defect energy levels to lie near the band edges or within the bands, giving these materials their notable defect tolerance.[45] However, halide perovskites are notoriously unstable in the presence of excess heat, above-bandgap photons, oxygen, and moisture. In contrast to current commercial PV materials, halide perovskites readily undergo chemical decomposition reactions when exposed to these stressors that can degrade optoelectronic performance and have, up to this point, limited the lifetime of PSCs well below the multidecade timescale necessary for commercial viability.[46] Stability of the absorber is thus a primary factor hindering PSCs from realizing their commercial potential.

Mixed-cation, mixed-halide perovskites in which the A-site comprises mixtures of formamidinium (FA), methylammonium (MA), and/or cesium, and the X-site comprises mixtures of iodide and bromide, form the absorber layer in some of the most efficient lead-based PSCs and display significant improvements in thermal stability and performance compared with the archetypal perovskite $MAPbI_3$.[47–50] These compositions nevertheless exhibit low chemical stability relative to conventional inorganic semiconductors.[51] While strong encapsulation may prevent the ingress of oxygen and moisture for some time during the deployment of a PSC module,[52] illumination is necessary for electrical energy production. Thus, studies of perovskite degradation in inert environments under illumination are vital to probe what may represent the ultimate performance-limiting case.

Previously, we reported the degradation kinetics of $MAPbI_3$[34] and the low bandgap lead-tin perovskite composition $FA_{0.75}Cs_{0.25}Pb_{0.5}Sn_{0.5}I_3$[35] in response to oxygen, moisture, and illumination. While measurable LID was not observed in these previous compositions, initial investigations into the degradation of $FA_{0.8}Cs_{0.2}Pb(I_{0.83}Br_{0.17})_3$ (referred to as FACsPbIBr) revealed

that unencapsulated films placed in an inert environment undergo decomposition when exposed to illumination alone. In this study, we investigate this decomposition pathway with the aims of identifying decomposition products and quantifying the rate of perovskite loss as a function of environmental stressors, since quantitative kinetic measurements of light-induced degradation do not currently exist in the literature.

The FACsPbIBr films used throughout this study were fabricated by an antisolvent wash method (described in SI section 3.7.1). The pristine films are of high optoelectronic quality. Characterization by x-ray diffraction (XRD), scanning electron microscopy (SEM), UV-Vis-NIR spectroscopy (UV-vis), and photoluminescence (PL) spectroscopy are shown in SI Figure 3.7. The films have an optical bandgap of ~1.66 eV and display steady-state quasi-Fermi level splitting of 1.29 eV under 1 sun equivalent illumination, which is >90% of the radiative limit (1.38 eV). Single-junction solar cells made from the films with a p-i-n architecture (ITO/Poly-TPD/perovskite/C_{60}/BCP/Ag) have efficiencies of ~17% (SI Figure 3.8).

3.3 Effects of LID on Mixed-cation, Mixed-halide Thin Films

To identify the hallmarks of this decomposition pathway, we performed *ex-situ* characterization of the FACsPbIBr films over a period of LID. SI section 3.7.2 (Figure 3.9b) includes the spectra of all illumination sources with a description of calibration procedures. Sources are calibrated such that the incident above bandgap absorbed photon flux is identical to that of the AM1.5 G solar spectrum (1.5 x 10^{21} photons/m^2/s for a 1.66 eV absorber).

Unencapsulated FACsPbIBr films deposited on glass substrates were placed in a chemically inert environment (dry N_2 glovebox) on a hotplate (shown schematically in Fig 3.9a) set to 65^{o}C under 1 sun equivalent photon flux from a broad-spectrum 'white' LED (emission from 400-700 nm) and were periodically removed for characterization. Figure 3.2 shows the changes of

the internal absorbance spectrum (see SI section 3.7.4 for further analysis), absolute intensity photoluminescence spectrum (AIPL), XRD pattern, and morphology over the course of degradation and demonstrates that optical absorption is a leading indicator of this decomposition mode. The mean PL peak (Figure 3.2b) redshifts modestly (~20 meV). The intensity drops rapidly, and a low energy shoulder develops as degradation proceeds. Since the Br content is relatively low, we do not expect this low energy shoulder to be a result of halide segregation but rather of shallow defect states.[53] The XRD patterns (Figure 3.2c) show that, over long periods of degradation, crystalline domains of metallic lead (Pb^0) begin to form, which first become discernable at the 13-hour timepoint. Aside from small peaks associated with PbI_2 (001-plane reflection at ~12.6°) and α-$FAPbBr_3$ (001-plane reflection at ~14.8°) at very late stages of degradation, no other solid degradation products are observed in the XRD patterns (zoomed-in plots and reference patterns are presented in SI section 3.7.3 and SI Figure 3.10). We also confirmed the presence of Pb^0 in degraded films with x-ray photoelectron spectroscopy (XPS) (SI Figure 3.11). The morphology, while minimally affected during early degradation times, becomes riddled with micron sized features during later times (Figure 3.2d), and the changes become most obvious on similar timescales as those for which Pb^0 begins to appear in the XRD pattern.

The absorbance measurements appear to be the most sensitive for identifying this decomposition mode (Figure 3.2a), as indicated by the increase in sub-bandgap absorbance within the first 30 minutes (inset of Figure 3.2a). The only plausible species that could absorb sub-bandgap photons is a reduced lead species. XRD and XPS provides insight that Pb^0 is present at advanced stages of degradation, but we cannot preclude the presence of other reduced lead species, especially at earlier degradation times.[54] After 120 minutes of exposure, the excess absorbance

spectrum (spanning regions both above and below the perovskite bandgap) closely resembles that of a ~5 nm film of elemental Pb^0 (see SI Figure 3.12 for the absorption spectrum of Pb^0 thin films). In summary, the optoelectronic properties of the perovskite film degrade significantly as defects associated with reduced lead species are generated during LID. Notably, substantial losses in PL intensity occur well before any significant changes in morphology or crystal structure are detectable, highlighting the importance of optical measurements as essential early indicators of this degradation pathway. The QFLS calculated from the PL quantum yield decays almost linearly, and while a solar cell using the films under study as absorbers would limit degradation by trapping decomposition products and extracting reactive charge carriers, reduced lead species formed during LID would deteriorate photovoltaic performance via increased trap assisted recombination (resulting in V_{oc} decline) and parasitic absorption (resulting in J_{sc} decline).[55]

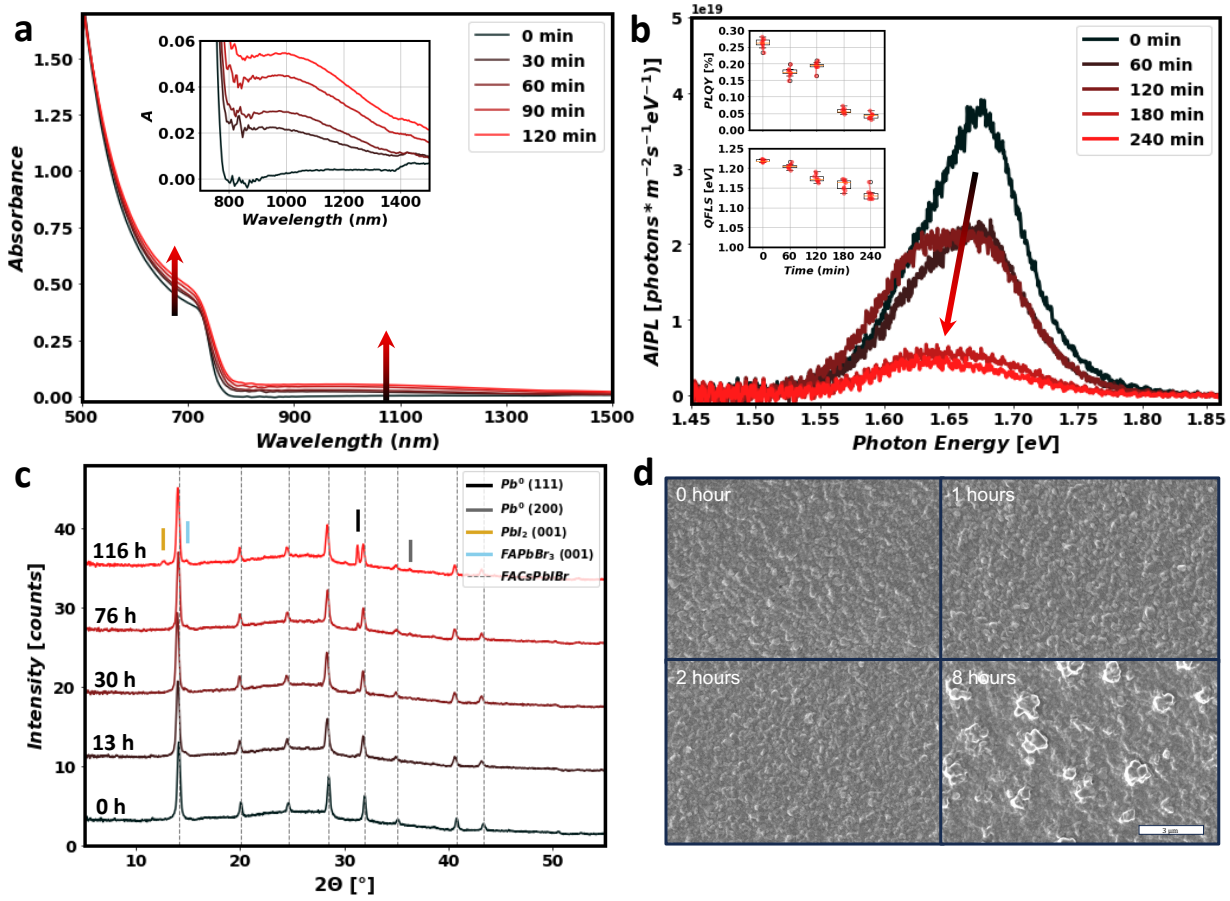

Figure 3.2 ***Ex-situ*** **characterization during degradation under 1 sun photon flux from a broad-spectrum LED at 65°C in a dry N_2 atmosphere.** The changes in (a) absorbance, (b) AIPL spectrum ($\lambda_{excitation} = 532\,nm$; 1 sun equivalent photon flux), (c) XRD pattern, and (d) morphology (SEM images). Inset in panel (a) is a magnified view of the sub-bandgap region. Insets in panel (b) are the *PLQY* and QFLS determined from the Ross relation (refer to SI section 1 for these calculations). Special care is taken to ensure that samples are outside of a controlled N_2 environment for as little time as possible (typical ambient lab conditions are ~40% relative humidity, 20°C; exposure during measurements is <30 minutes for XRD, <10 minutes for UV-Vis-NIR, <10 minutes for SEM, and 0 minutes for AIPL). SEM measurements are taken on separate samples to avoid conflating morphological effects of prolonged periods of vacuum exposure with LID.

3.4 Mechanism of Light-Induced Degradation.

The first reports of LID were of $MAPbI_3$ under vacuum.[56,57] However, FA-rich compositions are also susceptible to LID[58] with several reports observing hole trapping at grain boundaries which results in halide gas loss (X_2) and Pb^{2+} reduction to Pb^0.[59–61] Material quality

plays an important role in both initial optoelectronic device performance and stability.[62,63] Defect-dense and/or heterogenous films have reduced barriers for atomic, ionic, and molecular transport which increases the rate of material decomposition and device performance degradation.[64–66] While many of these prior reports suggest that Pb^{2+} in the perovskite lattice is directly reduced to Pb^0 during LID, other reports argue that the photolysis of intermediate PbI_2 is the pathway to form Pb^0 (some noting that it is possible[67]).[54,55,68]

Kerner et al.[69] hypothesized that halide oxidation ($h^+ + X^- \leftrightharpoons X^\cdot \leftrightharpoons \frac{1}{2}X_2$) by valence band holes (photoexcited or injected) can substantially increase halide species mobility (neutral $X^\cdot$ and X_2 are assumed to be much more mobile than perovskite bound X^-) which can yield two related but distinct phenomena. (1) If the halides settle in different domains, phase segregation results. The perovskite lattice remains intact, but different domains of varying halide concentration exist. Evidence of this behavior is typically observed with photoluminescence and electroluminescence spectroscopy[70–72], and it is usually reversible after the incident light is removed.[53] (2) If halides escape the perovskite lattice in the form of diatomic halide gases (X_2), decomposition occurs as the perovskite is irreversibly converted to other chemical species.[73,74] It is worth noting that the thermodynamics of halide vacancies[75] and the kinetics of species diffusion[76,77] are temperature dependent with the latter following Arrhenius behavior. These prior reports provide insights into the chemical processes that may be used to propose specific reaction pathways that in turn can be used to derive rate expressions for this decomposition mode. Given that many other studies report the formation of Pb^0 during LID, we operate under the assumption that the majority of the light-induced defects are Pb^0, accounting for most of the near-infrared light absorption.

3.5 Influence of Oxygen on LID

Before proceeding with further investigations into the LID of FACsPbIBr films, we seek to address how oxygen presence influences the degradation pathway. While O_2 and H_2O vapor may be kept out of a PSC during fabrication and for some time with encapsulation, even rigorous glass-glass encapsulation strategies with polyisobutylene (PIB) edge seals cannot fully prevent diffusion of gaseous small molecules.[78,79] It is thus important to understand how degradation will proceed if an environmental reactant diffuses through packaging to meet the perovskite layer. To do so, we analyzed the change in optical absorbance when films were subjected to various concentrations of ambient O_2 (0%, 3%, 10.5%, and 21%). In these experiments, we placed FACsPbIBr films in environmental control chambers and illuminated them with a broad-spectrum white LED (SI Figure 3.9a). We measured the surface temperature with a contact thermocouple and found it to be stable at 35ºC. The flow rate of inlet gases is 3 L/min with the desired oxygen concentration being achieved by mixing dry air and dry N_2.

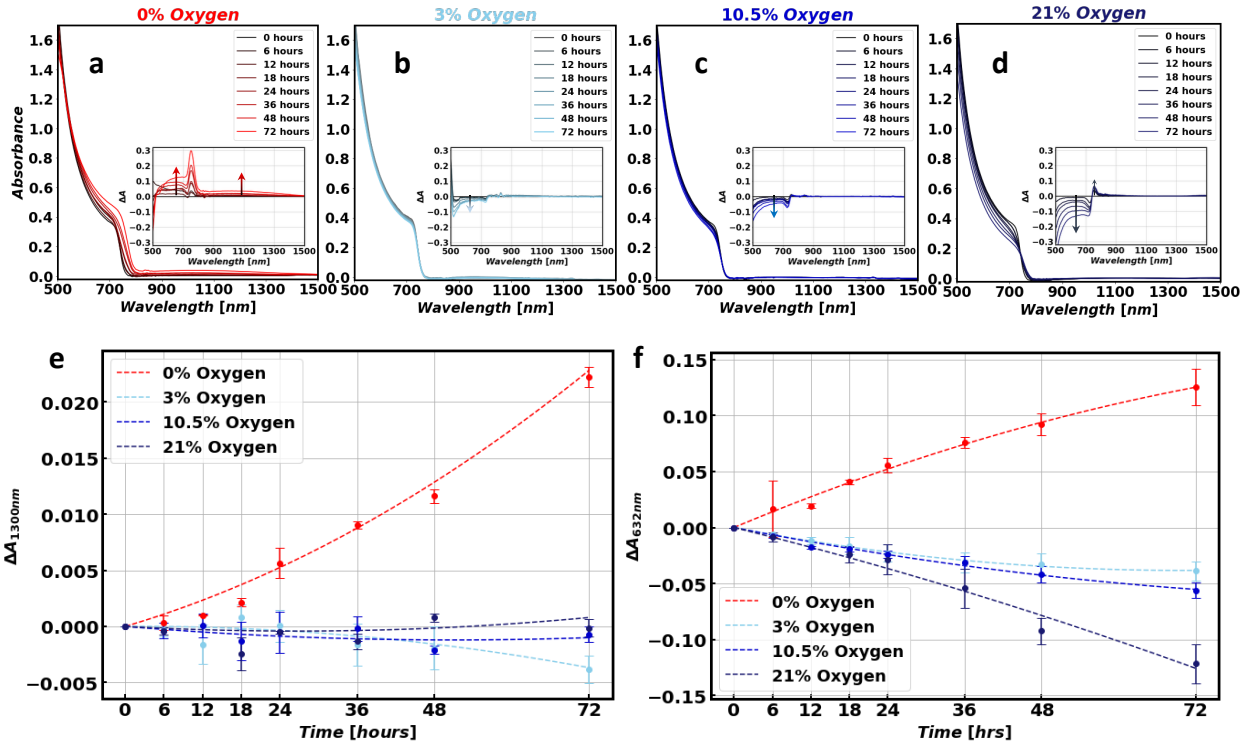

Figure 3.3. ***Ex-situ*** **UV-Vis-NIR measurements during degradation at 35ºC under 1 sun equivalent illumination**. Film absorbance over the course of degradation in dry atmospheres of (a) 0%, (b) 3%, (c) 10.5%, and (d) 21% oxygen. Insets in a-d are the change in absorbance from the initial time point with narrower vertical axes to emphasize the spectral changes over time. The timeseries absorbance values at (e) 1300 nm and (f) 632 nm. Parabolic fits to the timeseries data are included as dashed lines in (e) and (f) to guide the eye. Uncertainty is quantified by the standard deviation (σ) of film absorbance change for 3 samples.

The results of these experiments are shown in Figure 3.3, demonstrating that 3% O_2 in the ambient atmosphere is sufficient to prevent the accumulation of defects with near-infrared absorptivity (Pb^0). Although none of the samples degraded in oxygen-containing environments accumulated detectable levels of Pb^0, we infer that photooxidation processes did take place as evidenced by decreases in above bandgap absorbance, with higher oxygen concentrations yielding higher rates of decomposition. We speculate on the reason for O_2 preventing Pb^0 formation in SI section 3.7.8 and hypothesize that it scavenges photogenerated electrons that would otherwise reduce Pb^{2+}. Interestingly, examining Figure 3.3a and 3.3b reveals that the net effect of adding small amounts of oxygen to an otherwise inert atmosphere is a slower rate of film decomposition. The inset in Figure 3.3a reveals an outsized increase in absorption as LID proceeds in the 700-800 nm region. This behavior is observed to a lesser degree for degradation in 21% oxygen (inset of Fig. 3.3d). We attribute this to an increase in disorder of the semiconductor (either static or dynamic) resulting in increases in sub bandgap absorption in the region just below the bandgap (within ~0.1 eV).[80,81] As such, we do not observe measurable absorption increases in this region for the films degraded in 3% or 10.5% oxygen atmospheres because they degrade less significantly (and thus induce less additional disorder) than the films in 0% or 21% oxygen atmospheres. Importantly, the excess absorption beyond ~800 nm shown in the inset of Figure 3.3a agrees with the Pb^0 absorption spectrum shown in SI Figure 3.12, indicating that absorption measurements in the region >800 nm are accurate for quantitative measurements of Pb^0 formation.

While film absorbance measurements provide valuable information about absorbing species present in the film, the exact effect of any given degradation pathway on device relevant optoelectronic properties is unknown from absorption measurements alone. To address this missing link, we conducted *in situ* measurements of film ambipolar diffusion length (L_D) and photoluminescence quantum yield ($PLQY$) over the course of degradation in the same conditions as the *ex situ* experiments shown in Figure 3.3. To perform these measurements, we use a calibrated widefield microscope for $PLQY$ measurements and deposit gold contact pads on the FACsPbIBr films with a thin channel (0.01 cm) for simultaneous two-point photoconductivity measurements (Figure 3.4a,b). From photoconductivity measurements, we can obtain an estimate for the L_D based on sample geometry and photogeneration rate, which we have detailed in prior reports.[82,83] The results of these experiments are shown in Figure 3.4. Diffusion length is a good proxy for how we expect the film degradation to affect device performance as it unites both carrier transport and carrier lifetime. The $PLQY$ serves as a proxy for carrier lifetime alone, which helps disentangle changes in diffusion length due to lifetime from those caused by changes in carrier mobility.

Degradation in pure N_2 results in monotonic decreases in both L_D and $PLQY$. The evolution of the L_D is strongly correlated with that of the $PLQY$, suggesting that it may be almost entirely explained by Pb^0 trap state formation. In contrast, the films placed in oxygen containing atmospheres see an initial period of passivation (increasing L_D due to increasing minority carrier lifetime) followed by degradation (decreasing L_D attributable to reduction in effective mobility that likely arise from the buildup of insulating phases at grain boundaries). The kinetics of this behavior accelerate as the environmental oxygen content increases, consistent with a photooxidation mechanism that generates insulating byproducts that impede carrier transport.[82,84]

Note that the $PLQY$ generally rises for each of the oxygen containing runs, indicating that the local minority carrier lifetime is constant or increasing and suggesting that defect formation is not a critical issue in these cases. While these photooxidation phenomena are not unique to these perovskite compositions and have been reported previously for $MAPbI_3$,[76] the stark differences in optoelectronic decay from relatively small differences in ambient atmosphere contents for this perovskite composition is important because it indicates that relatively small amounts of oxygen are sufficient to shift the dominant mode of decomposition. Again, this may signify a role of oxygen as a particularly efficient scavenger of photogenerated electrons.[85] From the data shown in Figures 3.3 and 3.4, we infer that there is likely an oxygen concentration between 0% and 3% at which both mechanisms occur simultaneously but that concentrations $\geq$3% appear to prevent Pb^0 formation and are within the regime of purely photooxidation decomposition (all Pb^{2+} remains oxidized). However, it is important to note that even for low-oxygen environments in which LID is suppressed, apparent mobility losses can still quickly reduce the perovskite's optoelectronic quality, highlighting the importance of retarding photooxidation as well as LID.

To assess and compare the relevant time scales of diffusion length decay among the different degradation conditions, we define metrics of TL_D-80 and TL_D-90 which are defined as the time it takes for the diffusion length to decrease to 80% and 90% of its original value, respectively. The average TL_D-80 and TL_D-90 times ($\pm\sigma$) are displayed in Table 3-1. Importantly, the films placed in 0% O_2 reach L_D-90 faster on average than the films placed in any of the oxygen containing environments, highlighting the rapid optoelectronic performance decline that occurs during LID.

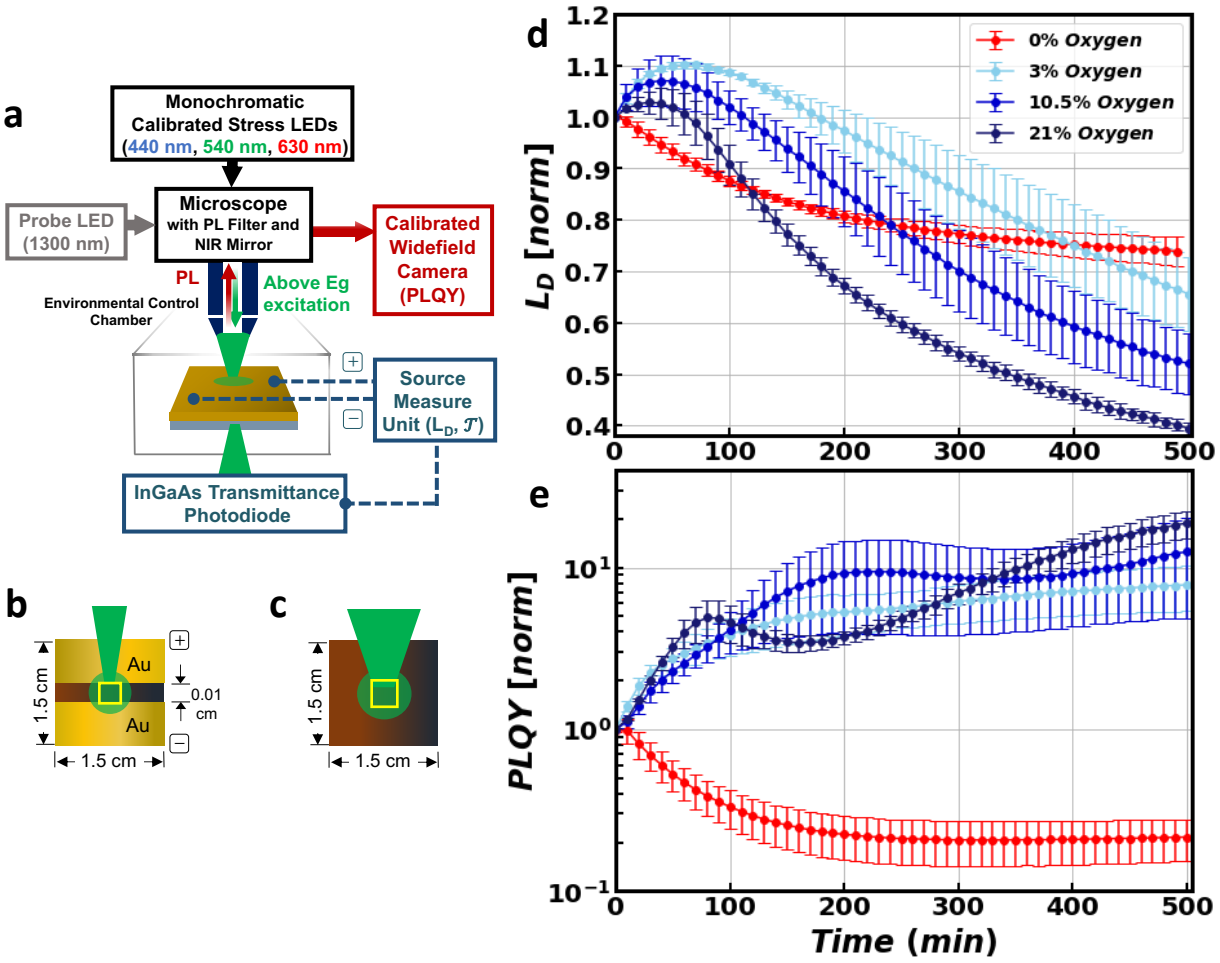

Figure 3.4. ***In-situ*** **optoelectronic performance trends for degradation in atmospheres of varying oxygen concentration**. (a) Schematic of the *in-situ* microscope degradation experimental apparatus which features a calibrated LED light source fed through an upright microscope and shone through an objective lens onto the sample. Top-down view of perovskite samples with (b) gold contacts (used for simultaneous collection of $PLQY$ and L_D) and (c) bare (used for $\mathcal{T}_{1300\,nm}$ measurements). The normalized (d) ambipolar diffusion length and (e) photoluminescence quantum yield under 10 sun equivalent photon flux at 65ºC. Uncertainty is quantified by the standard error of the mean ($\sigma/\sqrt{n}$) for 3 samples.

Table 3-1. $\boldsymbol{TL_D}$**-80 and** $\boldsymbol{TL_D}$**-90 Times for Degradation at 65ºC, 1 sun under Different Ambient Oxygen Concentrations**

$[O_2]$	TL_D-90 [min]	TL_D-80 [min]
0%	78 ± 20	293 ± 179

3%	285 ± 95	363 ± 115
10.5%	186 ± 74	242 ± 85
21%	97 ± 22	132 ± 20

3.6 Measuring the Kinetics of Light-Induced Defect Formation.

Having established that light-induced defect formation dominates the optoelectronic evolution of FACsPbIBr films in an inert N_2 atmosphere under illumination, we proceed with the aim of measuring and predicting the formation rate of these defects (with the assumption that most are Pb^0). We propose an overall net reaction for this process that uses $FAPbI_3$ as an approximation of the mixed-cation, mixed-halide composition. We do not expect the Cs or Br minorities to participate in important ways. To test this assumption, we also test the photostability of $FA_{0.8}Cs_{0.2}PbI_3$ and $FAPbI_3$ thin films (SI Figure 3.14). We observe that the absorbance of both compositions increases in the sub bandgap region after a period of photo-stress, indicating the universal susceptibility to LID of FA-rich compositions. Notably, the rate of sub-bandgap absorption increase is slower for these compositions compared to mixed-halide FACsPbIBr which agrees with the finding that halide alloying with bromine yields less photostable materials.[86] Thus, the net total LID reaction can be written as the following:

$$FAPbI_3 + h\nu \rightleftharpoons Pb^0_{solid} + I_{2,gas} + 3V_I + V_{Pb} + V_{FA} + \text{volatile organics} \qquad \text{(LID)}$$

SI section 3.7.5 discusses a plausible complete reaction mechanism with elementary steps for the LID reaction. We arrive at a functional form for a mathematical expression to describe the initial rate of Pb^0 formation (r_{Pb^0}) as a function of temperature and photon flux. Note that this

equation also happens to be identical to an empirical expression that could be written for the total LID reaction.

$$r_{Pb^0} = k_{0,LID} exp\left(-\frac{E_{A,LID}^{eff}}{k_B T}\right) I_{in}^{n} \quad (1)$$

Here, $k_{0,LID}$ is a temperature independent prefactor, $E_{A,LID}^{eff}$ is the effective activation energy, I_{in} is the incident above bandgap photon flux, and n is the effective order of illumination.

We next proceed to measure the kinetics of the LID reaction to determine the various unknown parameters contained within equation 1 for FACsPbIBr. We use a similar technique as in our previous kinetic studies[34,35] on initial perovskite decomposition rate to determine the rate of Pb^0 formation (r_{Pb^0}). Information regarding the initial perovskite reaction rate has been shown to be highly relevant for understanding and predicting device stability.[82,87] In short, we measure the sample transmittance ($\mathcal{T}$) at 1300 nm (where reflectance changes minimally over the early times of degradation, SI Figure 3.13) in an *in situ* degradation chamber (Figure 3.4a,c) to obtain an estimate for initial rate of absorbance change $\left(\frac{dA}{dt}\right)$. This allows us to quantify r_{Pb^0} by the following:

$$r_{Pb^0} = \frac{\rho_{Pb^0} \cdot log_{\mathrm{e}}(10)}{M_{Pb^0} \cdot \alpha_{1300\mathrm{nm}}} \cdot \frac{dA}{dt}$$

where ρ_{Pb^0} is the density, M_{Pb^0} is the molecular weight, and $\alpha_{1300\mathrm{nm}}$ is the absorption coefficient at 1300 nm for Pb^0. Refer to SI section 3.7.4 for a detailed discussion of this derivation.

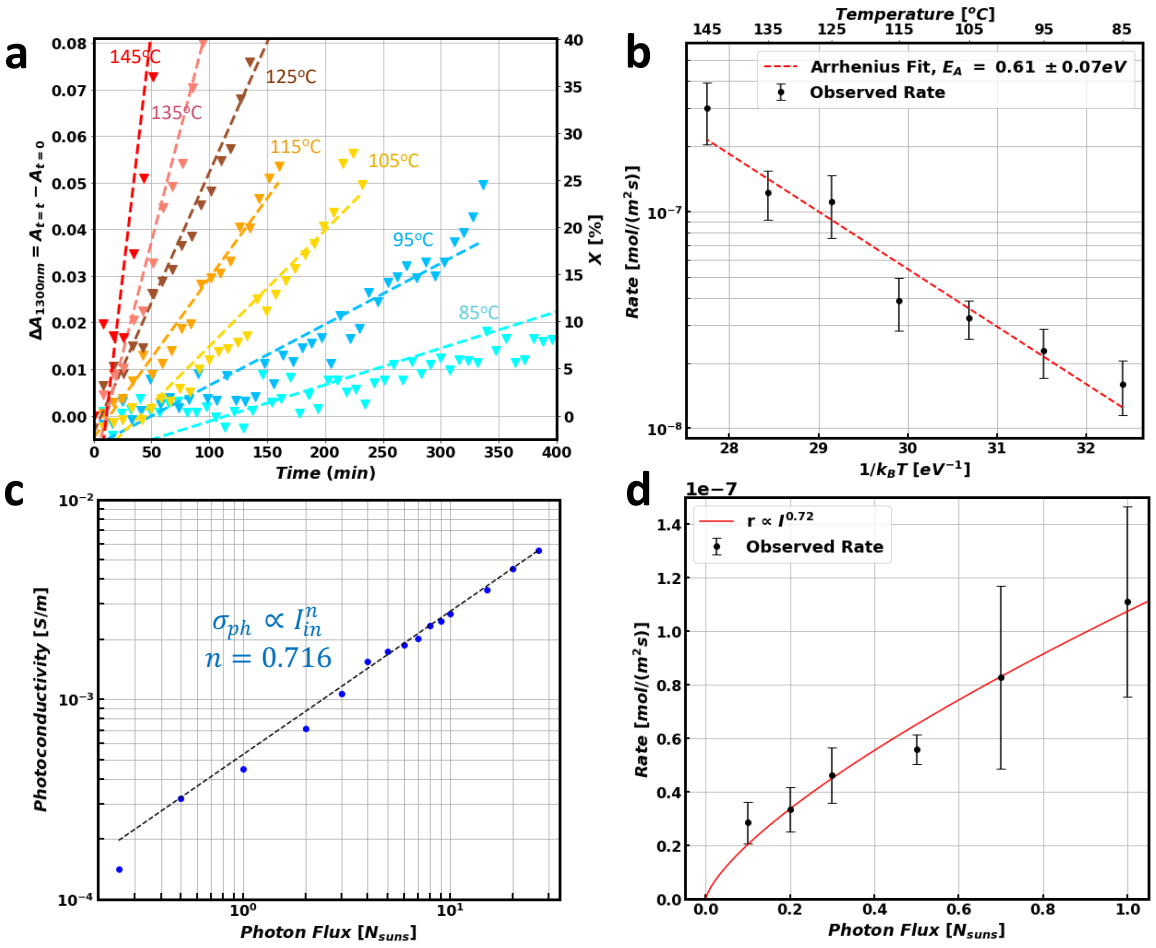

Figure 3.5. **Determining model parameters**. (a) Change in absorbance over time (with linear fits to the data used to determine $\frac{dA}{dt}$) during degradation with 1 sun photon flux. Percent film conversion to Pb^0 (X) is displayed on the right vertical axis. (b) Arrhenius plot for degradation experiments under 1 sun illumination at varying temperatures. (c) Photoconductivity versus photon flux with sublinear fit. (d) Initial Pb^0 formation rate as a function of incident photon flux at 125°C with fit (exponent fixed to 0.72).

Table 3-2. **Best-Fit Parameters for the Light-Induced Pb^0 Formation Kinetic Model**

Parameter	Value	Unit
$E_{A,\,LID}^{eff}$	0.61 ± 0.07	eV
$k_{0,LID}$	(3.55 ± 0.58) · 10^{-15}	mol ·m^{-2}·s^{-1}·(photons·m^{-2}·s^{-1})$^{-0.72}$

$\boldsymbol{n}$	0.72	unitless

To determine parameters that define equation 1 ($E_{A,LID}^{eff}$, n, $k_{0,LID}$), we used monochromatic 540 nm illumination over a range of temperature and illumination conditions. We choose to measure the rate of degradation at elevated temperatures (85 -145°C) due to the relatively slow rate of this reaction. We observe an Arrhenius relationship with respect to the effect of temperature on r_{Pb^0} which suggests that this reaction is thermally activated. Thus, we expect the experimentally determined parameters at elevated temperatures to remain accurate across a wide range of temperature and illumination conditions. We demonstrate that decomposition due to elevated temperature exposure, resulting in apparent loss of formamidinium, is negligible in comparison to LID in SI section 3.7.9 (particularly with regards to its effects on film optical properties, SI Figure 3.17).

Figure 3.5a displays typical data for the change in 1300 nm absorbance over time with linear fits to that data. Degradation experiments from 85-145°C under 1 sun equivalent photon flux are used to determine the activation energy as ~0.61 eV (Figure 3.5b). To determine the effective order of above bandgap photons (n), we performed photoconductivity measurements as a function of incident photon flux (Figure 3.5c). We have shown previously that the activity of a photoexcited species is directly proportional to the incident above bandgap photon flux raised to a constant value.[34] Additional information on the relationship between photoconductivity and photoexcited species activity is included in SI section 3.7.6. Here, we determine this value to be ~0.72 when measuring across a range of photon fluxes (0.25 to ~29 suns). To confirm that this exponent accurately captures the change in hole activity (posited to be the relevant photoexcited species)

during light-induced degradation, we measure r_{Pb^0} as a function of photon flux from 0.1-1 suns at 125ºC (Fig. 3.5d). A fit of the data is excellent (refer to SI section 3.7.7 for further fitting details), indicating that we have accurately captured the incremental activity of holes for increases in photon flux with our power law model.

To determine $k_{0,LID}$, we take all degradation runs used to determine $E_{A,LID}^{eff}$ (1 sun, 85-145ºC, 540 nm) and all runs used to confirm n (125ºC, 0.1-1 sun, 540 nm) and perform a minimization on the sum of the squared errors, which gives a result of $3.55 \times 10^{-15} \frac{mol}{m^2 s(photons \cdot m^2 s)^{0.72}}$. The dataset used for this fitting is referred to as the 'training dataset' (42 samples). The best-fit parameters for the kinetic rate model for Pb^0 formation are displayed in Table 3-2. Note that the uncertainty estimates for $E_{A,LID}^{eff}$ and $k_{0,LID}$ are quantified by the standard error of the linear fits to the Arrhenius plot and to the complete training dataset, respectively.

As mentioned previously, the debate around PbI_2 photolysis remains unanswered in the perovskite community. First, we note that significant Pb^0 is formed during irradiation with 540 nm light (E_{photon}=2.30 eV) which itself cannot excite PbI_2 by a band-to-band transition since it has an energy below the bandgap of PbI_2 (E_g ~ 2.35 eV). Thus, while PbI_2 photolysis may occur in perovskite samples with excess PbI_2 impurities, we note that this is not necessary to induce Pb^0 formation in our films and is not the mechanism that we observe since Pb^0 is formed even when the incident beam has photon energies less than the bandgap of PbI_2. To confirm this finding, we collected a new dataset (referred to as the 'test dataset' (28 samples)) that incorporates alternate temperatures and illumination conditions for 540 nm illumination as well as 440 nm (well above PbI_2 bandgap) and 630 nm illumination (well below PbI_2 bandgap). SI section 3.7.7 provides

further explanation of the conditions for the testing and training datasets and an expanded discussion of the fitting procedure for the parameters of equation 1.

Figure 3.6a shows the results for the training dataset with median and mean error of 34% and 71%, respectively. Figure 3.6b shows the results for the test dataset with median and mean error of 41% and 41%, respectively. Despite some sample-to-sample variation, we see that the model determined from the training dataset, which only considers a relatively small sliver of the parameter space, can accurately predict r_{Pb^0} for varying temperatures, photon fluxes, and photon energies. We emphasize that illumination wavelength within the visible regime minimally influences the degradation rate. Figure 3.6c shows the degradation data for the 630 nm and 440 nm illumination. This plot further emphasizes the goodness of the model fit and suggests that, if anything, the lower energy 630 nm light produces higher degradation rates than 440 nm. These results highlight that PbI_2 photolysis is not the mode of degradation that we observe en route to Pb^0 formation and suggest that degradation mitigation strategies outside that of the PbI_2 photolysis suppression framework must be considered to enhance perovskite longevity.

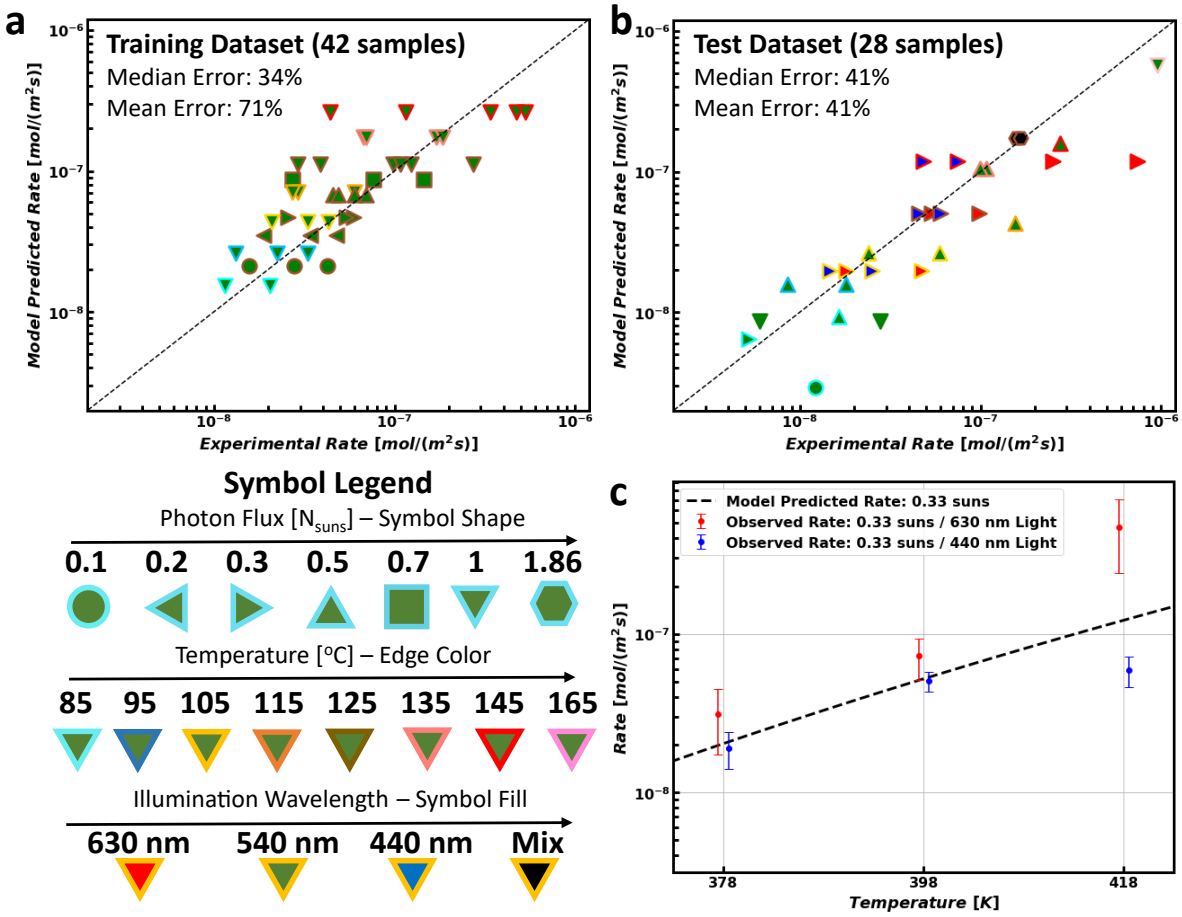

Figure 3.6. **Light-induced Pb^0 formation rate model performance**. (a) Parity plot for the training dataset and (b) for the test dataset. (c) Comparison of 630 nm monochromatic illumination (red) and 440 nm monochromatic illumination (blue) on Pb^0 rate. 630 nm and 440 nm photon fluxes are both set equal to 0.33 suns (5 x 10^{20} photons/m^2/s). Datapoints are sightly offset along the temperature axis for clarity.

3.7 Conclusion

Mitigation strategies for suppressing halide segregation and LID center around reducing halide mobility and escaping tendency from the perovskite. Device stacks with strong encapsulation will certainly slow volatile halide species loss and thus promote reverse decomposition reactions (e.g. $Pb^0 + I_2 \rightleftharpoons Pb^{2+} + 2I^-$), slowing LID processes. We demonstrate that encapsulation slows Pb^0 formation in SI section 3.7.10. However, the intrinsic material

instability related to mobile and reactive ions will remain and prevent the realization of multidecade module service lifetimes if a promising solution cannot be found. Promising paths towards reducing halide movement are via passivation (which will necessarily slow diffusion due to fewer vacancies present in the lattice[88,89]) and by tin substitution for lead (which shifts the valence band maximum above the halide defect energies and slows halide oxidation[90,91]). Ultimately, mobile halides that facilitate decomposition present a significant challenge for lead-based perovskite photovoltaic commercialization. We also would like to emphasize that the trapping of volatile I_2 vapor can promote other decomposition pathways (not just the reverse LID reaction) in a complete device stack.[92,93] As such, a complete picture of PSC device degradation under inert conditions would include LID, its reverse reaction, and I_2 related oxidation reactions with the perovskite itself and other layers in the device stack.

In summary, we report, for the first-time, quantitative measurements of light-induced degradation in a halide perovskite semiconductor. The degradation products of LID are reduced lead species with broadband optical absorption and are very likely fully reduced Pb^0. We have studied the effects of oxygen on this decomposition pathway and have derived a rate law for the initial rate of Pb^0 formation and fit it to our quantitative measurements. We also show that the wavelength distribution of the incident above bandgap photons negligibly influences the formation rate. This work raises important questions regarding how to address oxygen ingress through advanced encapsulation techniques, as well as how to manage the iodine species generated during LID, both of which remain significant challenges for enhancing the stability of perovskite-based devices.

3.8 Supporting Information

3.8.1 Experimental Methods; Film and Device Characterization

Sample Preparation: $FA_{0.8}Cs_{0.2}Pb(I_{0.83}Br_{0.17})_3$ precursor inks were prepared by dissolving stoichiometric CsI (FISHER SCIENTIFIC, 99.998%), FAI (Greatcell Solar Materials, >99.99%), PbI_2 (TCI AMERICA, 99.99%, trace metals basis) and $PbBr_2$ (TCI AMERICA, >98.0%) at 1 M concentration in 1/1 vol/vol N-methyl-2-pyrrolidone (NMP)/dimethylformamide (DMF), then allowed to dissolve overnight at 25°C. Glass substrates (15mm square) were cleaned with a four-step procedure by sonicating for 10 minutes each in (1) Alconox and DI water, then (2) DI water, then (3) acetone, and finally (4) 2-propanol. Shortly before spin coating, the substrates were cleaned for 10 minutes in an air plasma. $FA_{0.8}Cs_{0.2}Pb(I_{0.83}Br_{0.17})_3$ thin films were fabricated via spin coating in a N_2-filled glovebox. Before spin coating, the precursor inks were filtered through a 0.2 μm PTFE filter. 50 μL of the filtered precursor ink was spin coated at 4000 rpm for 45 sec. With 15 seconds remaining in the spin cycle, an antisolvent wash of 0.6 ml of toluene was dripped onto the sample to induce crystallization. Upon completion of the 45 second spin cycle, the films were annealed on a ceramic hotplate at 120°C for 15 minutes. Films averaged ~280 nm in thickness as measured with a Bruker OM-DektakXT stylus profilometer. For degradation experiments in which diffusion length measurements are also taken, 80nm Au contact pads (separation of 0.01 cm) were deposited via thermal evaporation at a rate of 2 Å/s. The $FAPbI_3$ and $FA_{0.8}Cs_{0.2}PbI_3$ films (discussed in SI section 5) were fabricated in the same way as the $FA_{0.8}Cs_{0.2}Pb(I_{0.83}Br_{0.17})_3$ with the adjustment of precursor solution inks to match the desired film composition. Additionally, to achieve the black alpha phase of FAPbI3, these films were annealed at 180°C for 15 minutes as opposed to 120°C. This is necessary to crystallize the alpha phase for pure (undoped) $FAPbI_3$ films.

Perovskite Film Characterization: Scanning electron microscopy (SEM) micrographs were obtained using a FEI XL30 SEM (SI Figure 3.7d) and a ThermoFisher Scientific Apreo SEM (Figure 3.2d).Thin film X-ray diffraction (XRD) measurements were collected with a Bruker D8 Discover instrument equipped with a Pilatus 100K large area 2D detector and a Cu anode (wavelength 1.542 Å, Kα radiation). The X-ray beam size was defined with a 0.3 mm collimator. X-ray photoelectron spectroscopy (XPS) measurements were taken on a ThermoScientific ESCALAB 250 with a monochromatic Al x-ray source and a 500-micron spot size. The binding energy scales were referenced to the C 1s peak at 284.8 eV. Optical absorbance spectra were collected from a PerkinElmer Lambda 1050 UV/vis/NIR spectrometer with an integrating sphere in laboratory atmosphere. Absorbance was calculated from separate measurements of sample percent transmittance and sample percent reflectance. Absorptance was calculated as $\mathcal{A} = 1 - \mathcal{T} - \mathcal{R}$. Absolute intensity confocal photoluminescence was collected as described previously.[83] PL spectra were obtained with a modified Horiba LabRAM HR-800 with 532 nm laser excitation and a 10x objective lens. The adjustable confocal hole was set to 800 μm, and a 150 gr/mm Czerny−Turner monochromator blazed at 500 nm was used. The photon detection rate was calibrated using a blackbody source (IR- 301, Infrared Systems Development) at 850, 950, and 1050 °C with a 10 μm pinhole (the calibration factor was averaged between the three temperatures to minimize error). To calculate 1 sun excitation flux, an Oriel optical power meter and Thorlabs

beam profiler were used to set the photon flux equal to above bandgap photon flux of the AM1.5 GT solar spectrum for a 1.66 eV material. Note that we can simply integrate the AIPL spectra to get a value for total emitted photon flux. Dividing this value by in incident photon flux gives us the external photoluminescence quantum yield ($PLQY$). From the $PLQY$, we can calculate an estimate for the quasi-fermi level splitting ($QFLS_{act}$) using the Ross relation: $QFLS_{act} = QFLS_{SQ} + k_B T \ln(PLQY)$ where $QFLS_{SQ}$ is the detailed balance limit QFLS for an absorber at a given bandgap.[31] The bandgap is set equal to the peak PL emission energy such that changes in material bandgap (although small) can be accounted for to give a better estimate of the true quasi-fermi level splitting in the material.

***In-situ* Optoelectronic Degradation Experiments**: For these degradation experiments, we place the sample, prepared as described above (with Au contact pads), in a Linkam Scientific LTSE420-P environmental test chamber, outfitted with an electric heater, gas ports, electrical probes, and windows above and below the sample. The atmosphere was controlled by connecting cylinders of N_2 (99.998%, 4.8 grade, Praxair) and dry air (0.0 grade "Extra Dry," Praxair via twin Omega FMA5400/5500 mass flow controllers to the gas port on the Linkam chamber, allowing the O_2 content to be varied while maintaining constant total gas flow set at 3.0 L/min. We use a calibrated 540 nm LED (Lumencor SpectraX Light Engine) as the light source in a metallurgical upright microscope (Olympus BX53M, equipped with a 100x Mitutoyo Plan Apo NIR HR objective lens), and adjust the input power based on the sample band gap to obtain the desired 1 sun equivalent flux of above-band gap photons under the AM1.5G spectrum. Because only a small region of the film surface is illuminated, thermal energy can dissipate laterally. Additionally, a constant flow of gas across the surface helps keep the illuminated area at the same temperature as the dark regions. Photoconductivity was measured by connecting Au contacts to a Keithley 2420 source meter and sourcing + or – 3V while measuring current. The polarity of the applied voltage is switched every measurement to prevent artifacts from ion migration and buildup over the duration of the experiment due to consistent applied voltage. Photoluminescence quantum yield (PLQY) measurements are obtained simultaneously under 10 sun equivalent excitation. All data collected is automated with a Python master control program that takes measurements every 5 minutes. This general procedure has been described previously.[82]

***In-situ* Metallic Lead Formation Rate Experiments**: Bare samples (without contacts) were used for measurements of metallic lead *in-situ*. For a typical degradation experiment, we place the sample prepared as describe above in a Linkam Scientific LTSE420-P environmental test chamber, outfitted with an electric heater, gas ports, and windows above and below the sample to allow light transmission. The test chamber is placed on a computer controlled XY stage. The nitrogen atmosphere was maintained by connecting a N_2 gas cylinder (99.998%, 4.8 grade) and setting the flow rate to 3L/min. with an Omega FMA5400/5500 mass flow controller. For these measurements, we use an Olympus 5x objective lens to degrade the sample. Periodically (every 8 minutes), we switch off the degradation beam and collect a measurement of transmittance with a 1300 nm monochromatic light source. The transmittance is measured by short-circuit current measurements from a Thorlabs InGaAs photodiode (FGA10) placed underneath the sample. To account for differences in responsivity as diode temperature fluctuates over the course of a degradation experiment due to natural thermal fluctuation in the lab, we also collect a '100%

transmittance' measurement off the sample by moving the XY stage briefly such that the 1300 nm light is focused directly onto the photodiode (not passing through the sample). In this way, we can account for small changes in diode responsivity from time point to time point. All data collected is automated with a Python master control program.

Photovoltaic device fabrication and characterization: For fabrication of ITO/Poly-TPD/ $FA_{0.8}Cs_{0.2}Pb(I_{0.83}Br_{0.17})/C_{60}$/BCP/Ag perovskite solar cells, ITO-coated glass substrates (1.5x1.5 cm, 15 Ω sq^{-1}, Yingkou Shangneng Photoelectric Material Co.) were sonicated in Alconox detergent solution, deionized water, acetone, and isopropanol for 10 min each, rinsing in deionized water in between each step. After the the last sonication, the substrates were dried with pressurized nitrogen and plasma cleaned in argon for 10 minutes. The substrates were then transferred to a nitrogen-filled glovebox, where they were spin-coated with a solution of ~1g/ml Poly-TPD (Poly[*N*,*N*′-bis(4-butylphenyl) -*N*,*N*′-bis(phenyl)-benzidine], Sigma Aldrich, M_W >20,000 g/mol) in ethanol at 3000 rpm for one minute. The substrates were then annealed in the glovebox at 600 °C for 10 minutes to drive off excess solvent. After Poly-TPD deposition, a monolayer of PFN-P2 (Poly(9,9-bis(3'-(*N*,*N*-dimethyl)-*N*-ethylammoinium-propyl-2,7-fluorene)-alt-2,7-(9,9-dioctylfluorene))dibromide, Sigma-Aldrich) was deposited by dynamically spin-casting a precursor of ~0.5 mg/ml of PFN-P2 in methanol at 5,000 rpm. Residual solvent is allowed to evaporate for 30 minutes before proceeding to the next step. Next, a 1 M solution of perovskite precursor ink (see S1.1 above) dissolved in 1:1 v:v dimethyl formamide and and *N*-methyl-2-pyrrolidone was spin-cast onto the Poly-TPD-coated substrates at 4000 rpm for 45 s. 15 seconds prior to the end of the spin step, 700 µL of toluene (Sigma Aldrich, anhydrous grade) was dropped onto the substrate. The films were annealed on a hot plate at 120 °C for 15 min. After the perovskite deposition, the substrates were transferred to a separate glovebox with a thermal evaporator (Angstrom Engineering Nexdep). 40 nm of C_{60} (Lumtec), followed by 7 nm of bathocuproine (Sigma Aldrich, sublimed grade) were evaporated from tungsten boats at maximum deposition rates of 0.5 and 0.3 Å s^{-1}, respectively. The substrates were then placed beneath a shadow mask to deposit patterned Ag (Kurt Lesker, 99.99%) contacts at a maximum rate of 2 Å s^{-1}. Current voltage (*J-V*) curves of single-junction $FA_{0.8}Cs_{0.2}Pb(I_{0.83}Br_{0.17})_3$ devices were measured under simulated AM1.5 G solar illumination with 0.2 V/s sweep rate for forward and reverse sweeps. The light source is an Oriel VeraSol-2 AAA Solar Simulator. An OSI Optoelectronics UV-100DQ Si photodiode was used to set the lamp intensity to equal the integrated above-bandgap AM1.5GT photon flux for a 1.66 eV bandgap material. A mask area of ~0.0453 cm^2 was used.

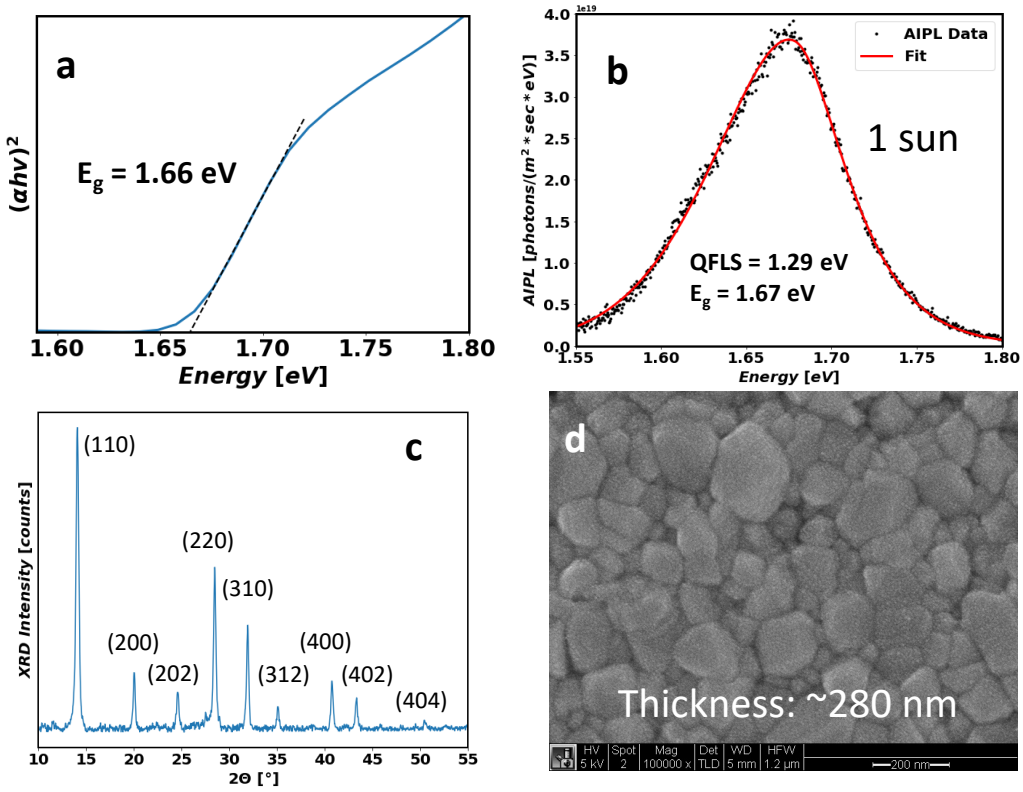

Figure 3.7. **Characterization of $FA_{0.8}Cs_{0.2}Pb(I_{0.83}Br_{0.17})_3$ thin film.** (a) Tauc plot with optical bandgap extrapolation, (b) absolute intensity photoluminescence (AIPL) spectra with full peak fit[32] to determine quasi-fermi level splitting (QFLS) under 1 sun equivalent photon flux, (c) x-ray diffraction pattern, and (d) scanning electron microscope image at 100kx magnification. QFLS under 1 sun equivalent illumination is equal to 93% of the radiative limit. The perovskite displays a strong absorption onset at the bandgap energy with clean morphology and diffraction pattern indicative of a single perovskite phase.

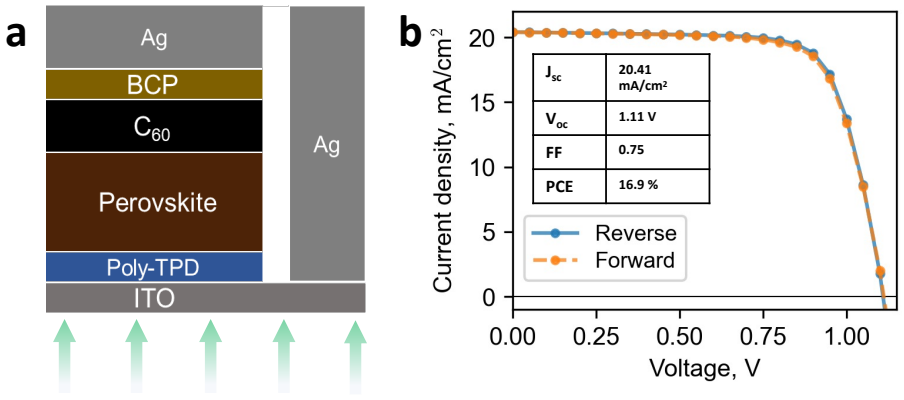

Figure 3.8. **Device characterization of $FA_{0.8}Cs_{0.2}Pb(I_{0.83}Br_{0.17})_3$ devices.** (a) Schematic of p-i-n device architecture, (b) current-voltage characteristic of the devices under 1 sun equivalent

illumination. The devices made from the mixed cation, mixed halide films have good power conversion efficiency and an open-circuit voltage that is 81% of the radiative limit. Despite the films being thinner than desirable for high efficiency device fabrication, short-circuit current is still >86% of the radiative limit.

3.8.2 ***Light Sources Used for All Degradation Experiments***

We aim to replicate conditions of normal solar illumination (Standard AM 1.5 Global Spectrum). To do so, we integrate the AM1.5 G spectrum above the bandgap of the perovskite to determine that the equivalent photon flux above the bandgap (1.66 eV) is 1.5×10^{21} photons/m^2/s. We perform calibration on each of the light sources as follows.

In-situ **Measurements**: All *in-situ* degradation measurements are taken on samples placed in an environmental control chamber in an upright microscope setup (Figure 3.4a provides a schematic of this setup). The incident beams are fed through via a liquid light guide cable from a Lumencor SpectraX Light Engine source. We use a Thorlabs Scanning Slit Optical Beam Profiler to assess the shape and distribution of the incident beam that is shown on the sample for each of the monochromatic LED emissions: red (~630 nm – red trace in Figure S3b), green (~540 nm – green trace in Figure S3b), and blue (~440 nm – blue trace in Figure S3b). We then assess the total power of the beam with an Oriel optical power meter. Homemade Python code is used to fit an appropriate distribution to the curves and determine the total equivalent photon flux (in units of photons/m^2/s) for the various LEDs and output settings. This procedure can be done for any objective lens to ensure proper calibration for both high magnification and low magnification lenses. The 1300 nm probe light is generated by a Thorlabs Fiber-Coupled LED (M1300F1-1300nm), and the emission spectrum is narrowed with a 1300 nm bandpass filter (Edmund Optics, 12nm FWHM).

Ex-situ **Measurements**: For *ex-situ* measurements, we illuminate perovskite samples in environmental control chambers with a broad-spectrum white LED that has emission between 400 and 700 nm (gold trace in Figure S3b). The resulting emission appears white to the eye. To ensure that the absorbed photon flux is close to that for those in the *in-situ* setup, we take single-junction perovskite solar cells (identical to those discussed in SI section 1) and determine the short circuit current under 1 sun equivalent illumination for the ~540 nm monochromatic LED in the microscope setup. We then take this identical device and place it under the broad-spectrum white LED and adjust the input power until identical short circuit current is reached. A standard silicon reference photodiode is used to ensure that the photon flux is the same for all *ex-situ* degradation experiments. In this way, we can achieve similar absorbed photon fluxes between the *in-situ* and *ex-situ* setups despite the varying spectral distributions of the light sources.

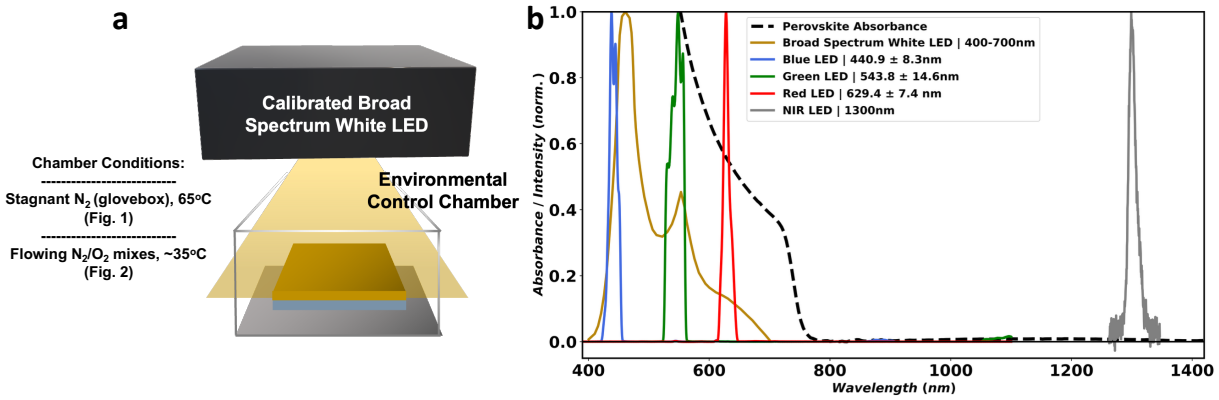

Figure 3.9. **Light sources used for degradation.** (a) Schematic of the *ex-situ* degradation setup. (b) Spectral distribution of LED light sources used for degradation (blue, green, red, and broad spectrum white) plotted with the $FA_{0.8}Cs_{0.2}Pb(I_{0.83}Br_{0.17})_3$ perovskite film absorbance and the 1300 nm near-infrared LED (used to probe Pb^0 formation but not used as a stressor). All degradation light sources are above the bandgap of the material while the 1300 nm probe beam is well below.

3.8.3 ***Identification of Degradation Products***

Here, we present zoomed in diffractograms along with reference patterns for identification of the crystalline degradation products that form during LID. The information is shown below in Figure S4 and is identical that shown in Figure 1c. As discussed in the main text, the primary crystalline degradation product that we observe is metallic lead (Pb^0) which is identifiable by the (111) and (200) reflections at 31.3° and 36.3°, respectively. At later stages of degradation, we also observe the (001) reflection of cubic $FAPbBr_3$ at ~14.8° and the (001) reflection of PbI_2 at 12.6°. The former may be the result of I_2 loss which leaves behind a top layer of Br enriched perovskite while the latter may form from simultaneous I_2 loss and consumption of organic formamidinium. We also observe a peak shift of the main (110) reflection of $FA_{0.8}Cs_{0.2}Pb(_{0.83}Br_{0.17})_3$ at ~14.1° to lower angles suggesting that the lattice is expanding as the material decomposes.

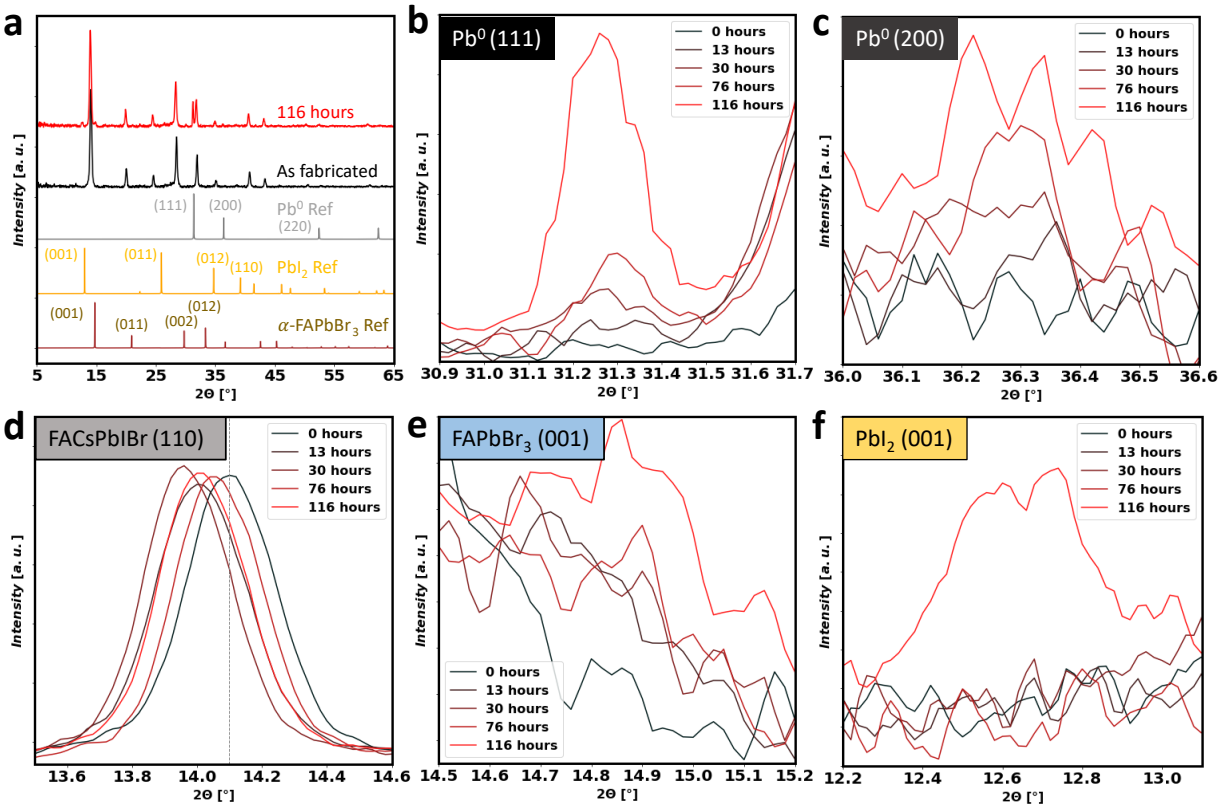

Figure 3.10. **Identification of crystalline degradation products during LID at 65ºC under 1 sun illumination.** (a) Diffraction patterns of samples as fabricated and after 116 hours of photo stress (background subtracted) along with simulated reference patterns for relevant degradation products (reference patterns: Pb^0: COD #1011119, PbI2: COD #1010062, α-$FAPbBr_3$: COD #7130785). (b-f) Zoomed-in look at the region of the diffractogram associated with plane reflections for (b) Pb^0 (111), (c) Pb^0 (200), (d) $FA_{0.8}Cs_{0.2}Pb(_{0.83}Br_{0.17})_3$ (110), (e) $FAPbBr_3$ (001), and (f) PbI_2 (001).

To further probe the chemical makeup of the FACsPbIBr films before and after LID, we performed x-ray photoelectron spectroscopy (XPS) on fresh and degraded films. Figure S5 presents the high resolution Pb 4f spectra from these measurements. A low energy shoulder, indicative of metallic lead, that is not present in the fresh film is observed in the degraded film. Voigt profile fits to the high resolution Pb 4f spectra indicate that only Pb^{2+} is present in the fresh film whereas both Pb^{2+} and Pb^0 are present in the degraded film. The broadening of the Pb^{2+} peaks after degradation

suggests the presence of lead atoms that are in intermediate oxidation states in addition to those in the pure 2+ and 0 state.[54]

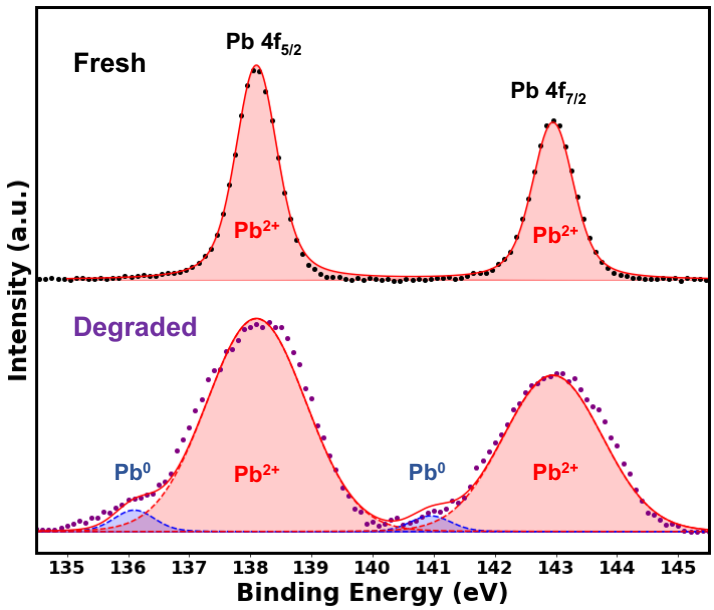

Figure 3.11. **XPS measurements of fresh and degraded films.** High resolution Pb 4f spectra for a fresh and degraded FACsPbIBr film. The degraded film was stressed at 145°C under 1 sun equivalent illumination for 5 hours.

3.8.4 ***Estimation of Initial Reduced Lead Formation Rate Calculated From 1300 nm Transmittance***

Internal optical absorbance A is defined in the following ways:

$$A = \log_{10}(e)\,\alpha l = -\log_{10}\left(\frac{\mathcal{T}}{1-\mathcal{R}}\right)$$

where α is the absorption coefficient at the measured wavelength, l is the path length of the absorbing medium (film thickness), $\mathcal{T}$ is the fractional transmittance of the film, and $\mathcal{R}$ is the fractional reflectance. Thus, internal absorbance measurements enable direct measurements of material thickness if the absorption coefficient is known. We can take the time derivative of absorbance $\left(\frac{dA}{dt}\right)$ to calculate a change in material thickness assuming that the absorbance change

is solely indicative of a singular species generation or consumption. If UV-Vis-NIR measurements are done such that we can obtain both $\mathcal{T}$ and $\mathcal{R}$ at a given wavelength at various time points during a degradation experiment, then the absolute internal absorbance is directly obtainable. If we have multiple time points, then we can simply fit a line to a plot of absolute internal absorbance versus time to determine $\frac{dA}{dt}$. This result is true for any species so long as the absorbance change calculated is attributable to that species alone. However, in our *in-situ* degradation setup, we can only obtain transmittance measurements. The setup is advantageous in that we can obtain data with high time resolution that does not require us to remove samples from a given environment. To determine rates, we aim rather to determine the change in absorbance with the following equation:

$$\Delta A = -\log_{10}\left(\frac{\mathcal{T}_{t=t}}{\mathcal{T}_{t=0}}\right) - \log_{10}\left(\frac{1-\mathcal{R}_{t=0}}{1-\mathcal{R}_{t=t}}\right)$$

If changes in reflectance are small, then the second term in the above equation vanishes and we arrive at an expression that relates transmittance changes alone to change in absorbance:

$$\Delta A = -\log_{10}\left(\frac{\mathcal{T}_{t=t}}{\mathcal{T}_{t=0}}\right)$$

Dividing ΔA by the time interval ΔT during early degradation periods gives $\frac{dA}{dt}$. From this and as described in previous publications on the chemical reaction kinetics of perovskite semiconductors,[34,35] we can then quantify the rate of chemical reaction for an absorbing species *i* by the following equation:

$$r_i = \frac{\rho_i \cdot log_e(10)}{M_i \cdot \alpha_i} \cdot \frac{dA}{dt}$$

where ρ_i is the density, M_i is the molecular weight, α_i is the absorption coefficient for the absorbing species i that is either being accumulated or depleted. $\frac{dA}{dt}$ is the rate of change of internal absorbance, calculated during 'early-times' (over the first ~120-240 minutes of a degradation experiment).

A necessary step to quantifying r_{Pb^0} is to determine α_{Pb^0} (density and molecular weight of Pb^0 are readily known but absorption coefficient is reported less). To determine the absorption coefficient of Pb^0 across the visible and near-infrared, we deposited thin films (50 nm) of Pb^0 on glass slides and measured the internal absorbance by UV-Vis-NIR (determined from transmittance and reflectance spectra). See Figure S6 below for the absorption coefficient spectrum determined for 3 films. Variation is generally small, so we averaged the 3 spectra and used the average as our experimentally determined absorption coefficient for Pb^0.

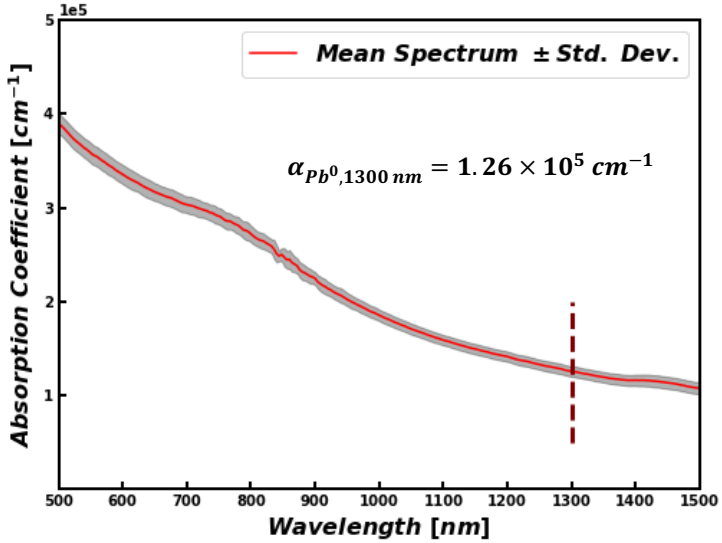

Figure 3.12. **Determination of Pb^0 Absorption Coefficient at 1300 nm.** UV-Vis-NIR absorbance measurement for metallic lead thin films (50 nm thickness). Thin films of lead were deposited by thermal evaporation on soda-lime glass substrates. Calibration of the tuning factor on the thermal evaporator was done by measuring film thicknesses with stylus profilometry. The absorption coefficient of metallic lead was determined to be 1.26 x 10^5 cm^{-1} at 1300 nm.

To determine the initial rate of lead formation *in-situ*, we focus on the sub perovskite bandgap (near-infrared) region of the electromagnetic spectrum for optical characterization. In this region, Pb^0 is the only species that will appreciably absorb light. Thus, sub bandgap absorbance changes indicate the formation of Pb^0 as the perovskite degrades during light-induced degradation. For accurate measurements, we need to select a wavelength that changes minimally in reflectance. To determine an appropriate wavelength, we obtained *ex-situ* UV-Vis-NIR measurements of transmittance, reflectance, and absorptance (calculated from $\mathcal{A} = 1 - \mathcal{T} - \mathcal{R}$) over the course of LID at 1 sun photon flux from a white LED at 65ºC in a N_2 filled glovebox. From these measurements, we determined that 1300 nm measurements were optimal for quantifying r_{Pb^0} *in-situ*. The results of this experiment are shown below in Figure S7.

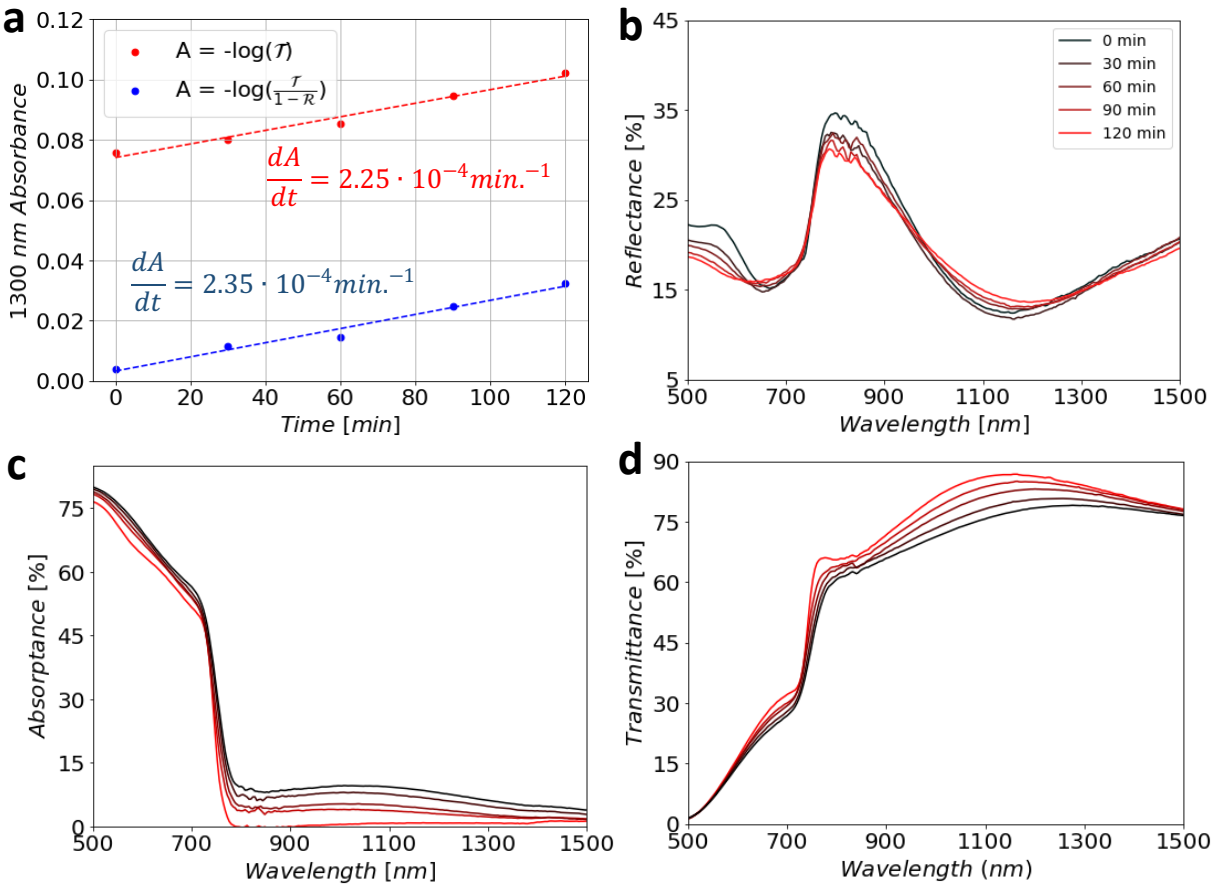

Figure 3.13. ***Ex-situ*** **UV-Vis-NIR measurements to determine appropriate wavelength for Pb^0 detection with *in-situ* transmittance.** (a) Absorbance at 1300 nm over time calculated from transmittance alone and with the effects of reflectance. Also included are (b) reflectance, (c) absorptance, and (d) transmittance spectra over the course of degradation. The conditions of this degradation experiment were 65°C under 1 sun equivalent illumination from a white LED (emission between 400nm and 700nm) in an N_2 filled glovebox. S5a shows that the reflectance changes are small during the early parts of degradation such that the rate of Pb^0 formation can be determined accurately from 1300 nm transmittance measurements alone. Percent error between the reflectance corrected and uncorrected fits is <5%.

3.8.5 ***Derivation of Rate Expression for Light-Induced Degradation Pathway***

The plausible complete chemical reaction pathway with elementary steps for the light-induced decomposition of $FAPbI_3$ is shown below. Here, we assume that FA^+ and I^- are much more reactive than Cs^+ and Br^-, respectively, such that during early times we can consider only the reactions of

FA^+, I^-, and Pb^{2+}. Thus, we have a rate expression that considers $FAPbI_3$ as the reacting perovskite species. The reaction yields the following net reaction of $FAPbI_3$ reacting with photons (via photoexcited electrons and holes) to produce Pb^0 and I_2 gas (FAI is assumed to be the volatile organic in this case):

$$FAPbI_3 + hv \rightarrow Pb^0 + I_2 + FAI \qquad \text{(LID)}$$

The reaction starts with photoexcitation and proceeds via oxidation of iodide interstitials:

$$hv \rightarrow e^- + h^+ \qquad \text{(1LID)}$$

$$FAPbI_3 \rightleftharpoons FAPbI_2^+ + I^- \qquad \text{(2LID)}$$

$$\mathbf{I^- + h^+ \rightarrow I^\cdot} \qquad \mathbf{(3LID)}$$

$$FAPbI_2^+ + e^- \rightarrow FAI + Pb^0 + I^\cdot \qquad \text{(4LID)}$$

$$2I^\cdot \rightarrow I_2 \qquad \text{(5LID)}$$

Now, we derive a mathematical form for r_{Pb^0} based on the proposed pathway. From this pathway, we begin with the following statement about r_{Pb^0}:

$$r_{Pb^0} = r_{4LID} = k_{4LID} a_{e^-} a_{FAPbI_2^+}$$

where a_{e^-} is the activity of electrons, $a_{FAPbI_2^+}$ is the activity of $FAPbI_2^+$ in the perovskite structure, and k_{4LID} is the temperature dependent rate constant for the forward reaction. We assume there to be a RDS (step 3LID) that (with note that we have 1:1 stoichiometry) allows us to write the following expression for r_{Pb^0}:

$$r_{Pb^0} = r_{3LID} = k_{3LID} a_{h^+} a_{I^\cdot}$$

where a_{h^+} is the activity of holes, a_{I^-} is the activity of iodide defects in the perovskite structure, and k_{3LID} is the temperature dependent rate constant for the forward reaction. If we assume that the equilibrium kinetics of step 2LID are much faster than consumption of I^- in step 3LID, we come to the final mathematical expression for r_{Pb^0}:

$$r_{Pb^0} = k_{0,LID} \exp\left(-\frac{E_{A,LID}^{eff}}{k_B T}\right) I_{in}^{n} \quad (1)$$

where $k_{0,LID}$ is the temperature independent prefactor, $E_{A,LID}^{eff}$ is the effective activation energy of the LID decomposition reaction, I_{in} is the incident above bandgap photon flux, and n is the effective order of the above bandgap photon flux.

Comments on assumptions for this degradation pathway

A primary assumption of the reaction pathway is related to the low electron affinity of Pb^{2+}. We assume that the rate of Pb^{2+} reduction to Pb^0 is determined by the loss of I_2 from the film. Effectively, Pb^{2+} (even in the presence of photoexcited conduction band electrons) is unlikely to be reduced. However, the relative ease of oxidation of halide species, followed by mass transport and removal from the film, creates an electrochemical driving force for electrons due to a charge imbalance that develops as holes are consumed. Here, we choose to consider only the 'early-time' periods of degradation such that the activity of all intrinsic material defects remains relatively constant. We also note that the final mathematical rate expression is identical to that which could be formulated by a simple empirical expression (with the assumption that perovskite activity is constant) from the net reaction equation.

Lastly, we mention the assumption that $FAPbI_3$ be considered the reactive perovskite unit where we ignore the small affects associated with Cs^+ and Br^-. To test this, we fabricated $FA_{0.8}Cs_{0.2}PbI_3$ (E_g~1.59 eV) and $FAPbI_3$ (E_g~1.51 eV) via the same methods as those use for the $FA_{0.8}Cs_{0.2}Pb(I_{0.83}Br_{0.17})_3$ films. To obtain the black α-phase of $FAPbI_3$, an anneal temperature of 180°C was used. All other steps in the fabrication procedures are the same as those described in SI section 1. We replicated the experimental conditions of Figure 1 in the main text (65°C, ~1 sun equivalent photon flux in a stagnant N_2 filled glovebox) to determine if LID proceeds in these compositions. We monitor the changes in the internal absorbance. Figure S8 shows the results of this experiment where we can clearly observe that the sub bandgap absorbance increases for both compositions after a 10-hour degradation period, suggesting that indeed Pb^0 is being formed during LID. It appears that the rate of sub-bandgap absorbance increase (and thus the rate of Pb^0 formation) appears to be slower in these compositions. The differences among the various FA-rich compositions will be the subject of future studies.

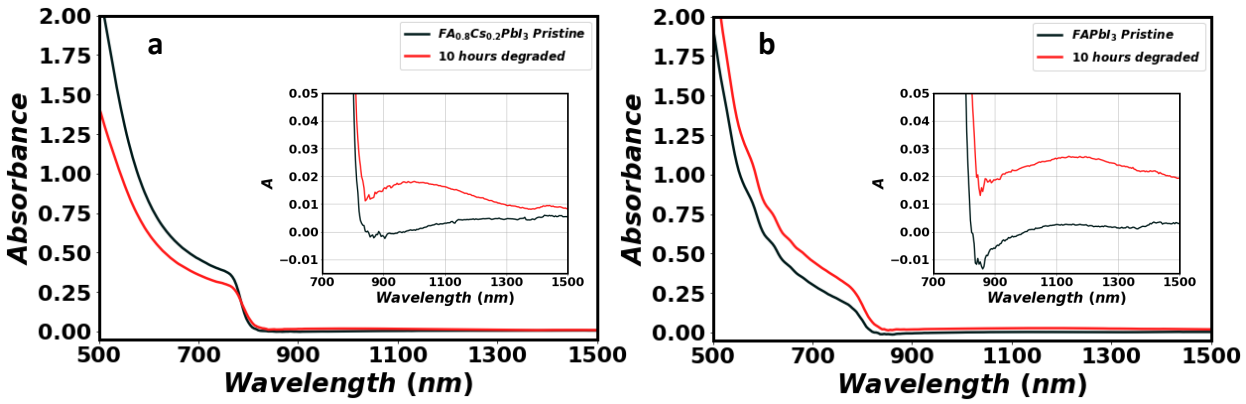

Figure 3.14. ***Ex-situ*** **UV-Vis-NIR absorbance of $FA_{0.8}Cs_{0.2}PbI_3$ and $FAPbI_3$ during LID. Absorbance of (a)** $FA_{0.8}Cs_{0.2}PbI_3$ and (b) $FAPbI_3$ films before (black trace) and after (red trace) a 10-hour period of light-induced degradation at 65°C in a N_2 glovebox. Insets are zoomed in regions from 700 to 1500 nm

3.8.6 ***Influence of Photon Flux on Photoactive Species Activity***

To determine the influence of above bandgap photon flux on photoexcited species activity, we performed photon flux dependent photoconductivity measurements (see Figure 4c in the main text). The justification for assigning the value n to this rate constant is explained in full in our prior paper on $MAPbI_3$ degradation.[2] In brief, we can conclude that photoconductivity is directly proportional to the photoactivity species activity with the following discussion.

By combining equations for the definition of thermodynamic activity of a species and assuming quasi-thermal equilibrium of an intrinsic semiconductor, we can write the activity of photoexcited holes in the perovskite under illumination as the following:

$$a_{h^+} = \exp\left(\frac{-k_B T(\ln p_h - \ln N_v) + E_v - \mu_h^0}{k_B T}\right)$$

where p_h, N_v, E_v, and μ_h^0 are the hole concentration, effective density of states in the valence band, valence band energy level, and chemical potential of holes under some standard thermodynamic condition, respectively. From this, we can pull out all constants into one (C) and conclude that activity of holes (a_h) is directly proportional to hole concentration:

$$a_{h^+} = C \cdot p_h$$

We also know that photoconductivity is directly proportional to concentrations of photoexcited species by the following equation:

$$\sigma_{ph} = q\,(\mu_h^{mob} p_h + \mu_e^{mob} n_e)$$

where q and n_e are the fundamental unit of electric charge and the electron concentration, respectively. μ_h^{mob} and μ_e^{mob} are the mobilities of holes and electrons, respectively (denoted as such so as not to confuse with chemical potential). For an intrinsic semiconductor under 1 sun illumination, the excited carrier populations should be much larger than the equilibrium populations, and thus $n_e \approx p_h$, so $\sigma_{ph} \approx q\left(\mu_h^{mob} + \mu_e^{mob}\right)p_h$. This allows us to conclude that photoconductivity is directly proportional to activity of holes.

Thus, the power law fit of photoconductivity versus photon flux should yield a parameter that accurately quantifies the incremental increase in photoexcited species activity with increases in above bandgap photon flux (photons that cannot be absorbed will obviously not influence photoexcited species activity). The absolute activity will be lumped into the pre-exponential factor of equation 1, $k_{0,LID}$. Again, note that this result matches experimental data of metallic lead rates quite well (figure 4d in the main text). The relationship between photoconductivity and incident photon flux in solids has been discussed previously by Schellenberg and Kao.[94] They concluded that it should take on the following form:

$$\sigma_{ph} \propto I^{\beta}$$

where β typically takes a value between 0.5 and 1 ($0.5 \leq \beta \leq 1$) for solid semiconductors. Our result of 0.72 in Figure 4c agrees with this earlier theoretical result.

3.8.7 ***Explanation of Procedure for Data Fitting and Testing***

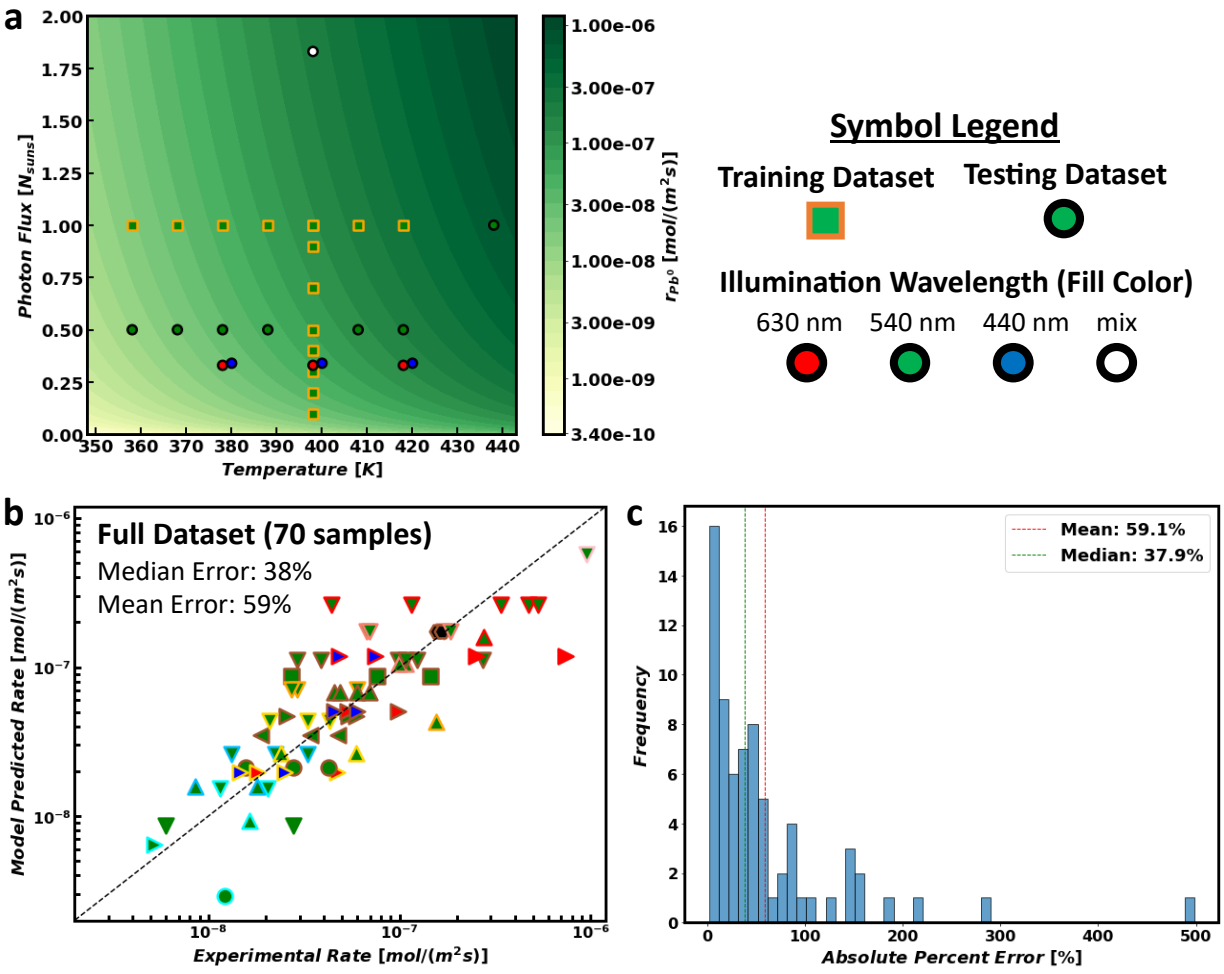

Figure 3.15. **Explanation of complete LID dataset.** (a) Contour plot of model predicted r_{Pb^0} over a range of temperatures and photon fluxes. On the contour plot are symbols that reference specific conditions associated with the training dataset and test dataset. The training dataset (orange squares) includes all runs degraded under 540 nm light that are at 1 sun *or* at 125°C (0.1-1 suns). The test dataset (black circles) includes 540 nm illumination runs at 0.5 suns over a range of temperatures (85, 95, 105, 115, 135, 145°C). It also includes 2 runs at 1.86 suns with a mixture of wavelengths (white filled), duplicates of runs at 0.33 suns and temperatures of 378, 398, and 418 K for 440 nm (blue filled) and 630 nm (red fill) illumination (these points are offset to be identifiable), and one run at 165°C, 1 sun to provide confidence in our hypothesis of Arrhenius behavior over a wide range of temperatures. (b) Parity plot for the complete dataset that consists of both training and test datasets combined (70 samples in total). (c) Histogram of the absolute percent error for the complete dataset.

To determine each parameter of the LID equation 1, we perform the following fitting procedures:

Activation Energy ($E_{A,LID}^{eff}$): The subset of the training dataset used for activation energy determination is runs at 1 sun, 540 nm light, over temperatures from 85-145ºC. From the averages of r_{Pb^0} for identical conditions, we perform an Arrhenius fit (Figure 4b) to determine the activation energy. The uncertainty associated with the activation energy is quantified by the standard error of this linear fit.

Effective Order of Illumination (n): As described in the main text and in section S6 above, we first perform photoconductivity versus photon flux measurements. With the knowledge that hole activity follows a sublinear relationship with incident photon flux ($a_{h^+} \propto I_{in}^n$), we fit photoconductivity data ($\sigma_{ph} \propto I_{in}^n$) over a range of illumination intensities (0.1 to ~29 suns) and find that the relationship can accurately be described for an n value of 0.72 (rounded from 0.716). To confirm that 0.72 is an appropriate exponent to quantify the role of illumination on hole activity, we performed a model fit (Figure 4d) in which the exponent is set to be 0.72 ($r_{Pb^0} = A * I_{in}^{0.72}$ where A is the only fitting parameter). We find that we can achieve an excellent fit to the data with an r^2 of 0.97. To additionally confirm that this exponent is proper, we performed a fit (Figure S7) to a model in which both the pre-exponent and n are fitting parameters ($r_{Pb^0} = A * I_{in}^n$). Here, we see that the fit results in an n of 0.718. Thus, we take 0.72 to be the value of n. The confirmation data is comprised of runs at 125ºC over a range of illumination intensities is also considered part of the 'training dataset.' All model fits are done with the curve_fit function within Python's SciPy library.

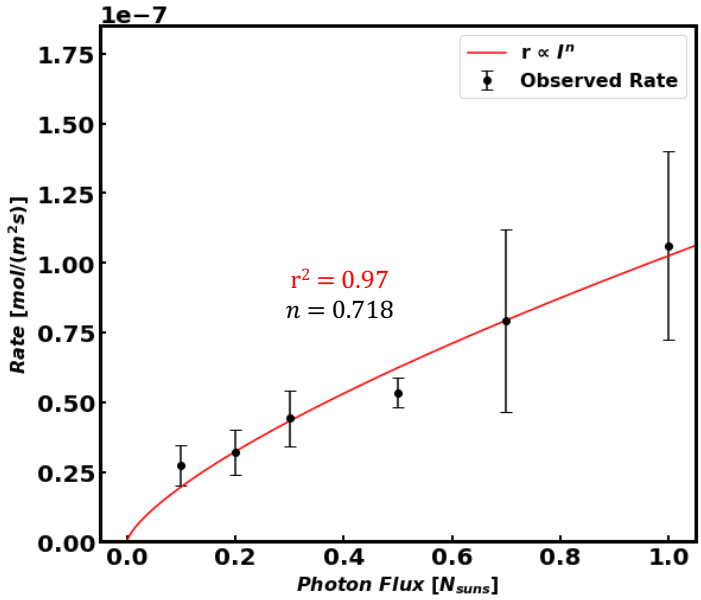

Figure 3.16. **Fit of r_{Pb^0} with varying photon flux.** Initial rate of Pb^0 formation versus photon flux (0.1-1 suns, 540 nm light) at 125°C . The exponent n is determined the be ~0.72, and r^2 of the fit is 0.97. Error bars quantify the uncertainty with the standard error of the mean for runs at identical conditions.

Preexponential Factor ($k_{0,LID}$): After setting the $E_{A,LID}^{eff}$ and n, we take the whole training dataset and calculate the preexponential that minimizes the sum of squared errors between the experimentally determined rates and the model predicted. This is a linear fitting procedure ($Observed\ rate = A \cdot \exp\left(\frac{-0.61\ eV}{k_B T}\right) * I_{in}^{0.72}$ where A is the only fit parameter). We quantify the uncertainty of this value with the standard error of the linear fit for A using the entire training dataset

3.8.8 ***Speculation on the Role of O2 in Preventing Pb^0 Formation***

O_2 presence in the ambient atmosphere, even in relatively small concentrations, alters the nature of the chemical reactions that the perovskite undergoes. We can visualize this by the different optical and optoelectronic progressions shown in Figures 2 and 3 in the main text. During

photoexcitation, photoexcited electrons are likely to be taken up by adsorbed O_2 (O_2^*) to form superoxide radicals ($O_2^{*-\cdot}$). Thus, the chemical plausibility of a reduction reaction (i.e., Pb^{2+} reduction to Pb^0) happening is substantially less likely based on this understanding alone. While it is not possible for us to explicitly answer how O_2 prevents Pb^0 formation, we can hypothesize some plausible reactions that may occur. Principally, we want to determine what the reduced species is since it is clearly not Pb^{2+}. Note that, in many forms of halide perovskite decomposition, I_2 is the oxidized decomposition product. When O_2 is absent from the ambient atmosphere, Pb^{2+} is reduced to Pb^0. O_2 is principally altering the species that is reduced (presumably by acting as a catalyst or being consumed itself). We hypothesize two potential pathways that each begin with superoxide radical formation: (A) proton abstraction from formamidinium to produce formamidine and (B) lead-oxide formation. The two hypothetical processes begin with the adsorption of O_2 onto a surface adsorption site followed by the uptake of a conduction band electron to form a superoxide radical:

$$h\nu \rightleftharpoons e^- + h^+ \tag{1O}$$

$$O_2 + [*] \rightleftharpoons O_2^* \tag{2O}$$

$$O_2^* + e^- \rightleftharpoons O_2^{*-\cdot} \tag{3O}$$

Rather than electrons flowing from the conduction band directly to Pb^{2+} reduction, the electron path is rerouted, being taken up by adsorbed O_2 (a strong electron acceptor) and reacting instead with an organic cation or directly with Pb^{2+}. In either case, Pb^{2+} stays in its oxidized form as Pb(II) or Pb(IV).

(A) Proton abstraction from formamidinium to produce formamidine:

$$FAPbI_3 + O_2^{*-\cdot} \rightleftharpoons FA^0 + HO_2^{\cdot *} + PbI_2 + I^- \quad (1A\text{-}O)$$

$$FA^0 \rightarrow \text{volatile organics (g} \uparrow) \quad (2A\text{-}O)$$

$$HO_2^{\cdot *} \rightarrow \frac{1}{2}H_2 + O_2^* \quad (3A\text{-}O)$$

$$I^- + h^+ \rightarrow \frac{1}{2}I_2 \quad (4A\text{-}O)$$

with the net reaction of:

$$FAPbI_3 + hv \xrightarrow{O_2} FA^0 + PbI_2 + \frac{1}{2}I_2 \quad (A\text{-}O)$$

(B) Lead oxide formation:

$$FAPbI_3 + O_2^{*-\cdot} + e^- \rightarrow PbO_2 + 3I_i^- + FA_i^+ \quad (1B\text{-}O)$$

$$2I_i^- + 2h^+ \rightarrow I_2 \quad (2B\text{-}O)$$

$$I_i^- + FA_i^+ \rightarrow FAI \quad (3B\text{-}O)$$

with the net reaction of:

$$FAPbI_3 + 2hv + O_2 \rightarrow FAI + PbO_2 + I_2 \quad (B\text{-}O)$$

In each of the above cases, the reduced species is different than LID, but the oxidized species is still I_2. Future studies will seek to elucidate the reaction mechanisms for the photooxidation of FA-rich perovskite compositions.

3.8.9 ***Effects of High Temperature Exposure***

Due to the relatively slow rate of this reaction coupled with the specific sensitivity of our detection instruments, we chose to fit the kinetic model with degradation experiments performed at elevated temperatures (85°C and 145°C). To determine the effects of high temperature exposure on the samples compared to high temperature with illumination, a $FA_{0.8}Cs_{0.2}Pb(I_{0.83}Br_{0.17})_3$ film was degraded in our *in-situ* degradation chamber at 145°C (maximum temperature used for rate law fitting) under 1 sun illumination from a monochromatic 540 nm green LED. Every hour for three

hours, the sample was briefly removed from the flowing N_2 atmosphere to collect transmittance spectra and XRD patterns inside and outside of the degradation beam area. Figure S9 shows the results of these experiments. The changes in transmittance spectrum are very distinct between the two regions (fig. S11a,c). For the illuminated region, the transmittance decreases significantly in the low energy visible and near infrared with a slight increase at wavelengths below ~600 nm. In contrast, the transmittance spectrum outside the illuminated region changes minimally over 3 hours. In agreement with our *ex-situ* measurements shown in Figure 1, we again see the Pb^0 (111) reflection at ~31.3° as well as the $FAPbBr_3$ (001) reflection at ~14.8°. We do not observe the PbI_2 (001) peak at ~12.6° for the illuminated region but do observe a small peak associated with this reflection in the unilluminated region. The appearance of this peak is most likely attributable to thermal decomposition of formamidinium.[95] Thus, we cannot conclude that no degradation occurs because of high temperature exposure, but it is apparent that any degradation occurring is quite small in magnitude compared to LID at an identical temperature. Importantly, any degradation that may be occurring appears to minimally affect the optical properties. We have also shown that high temperatures are not required for LID Pb^0 formation in Figure 2.

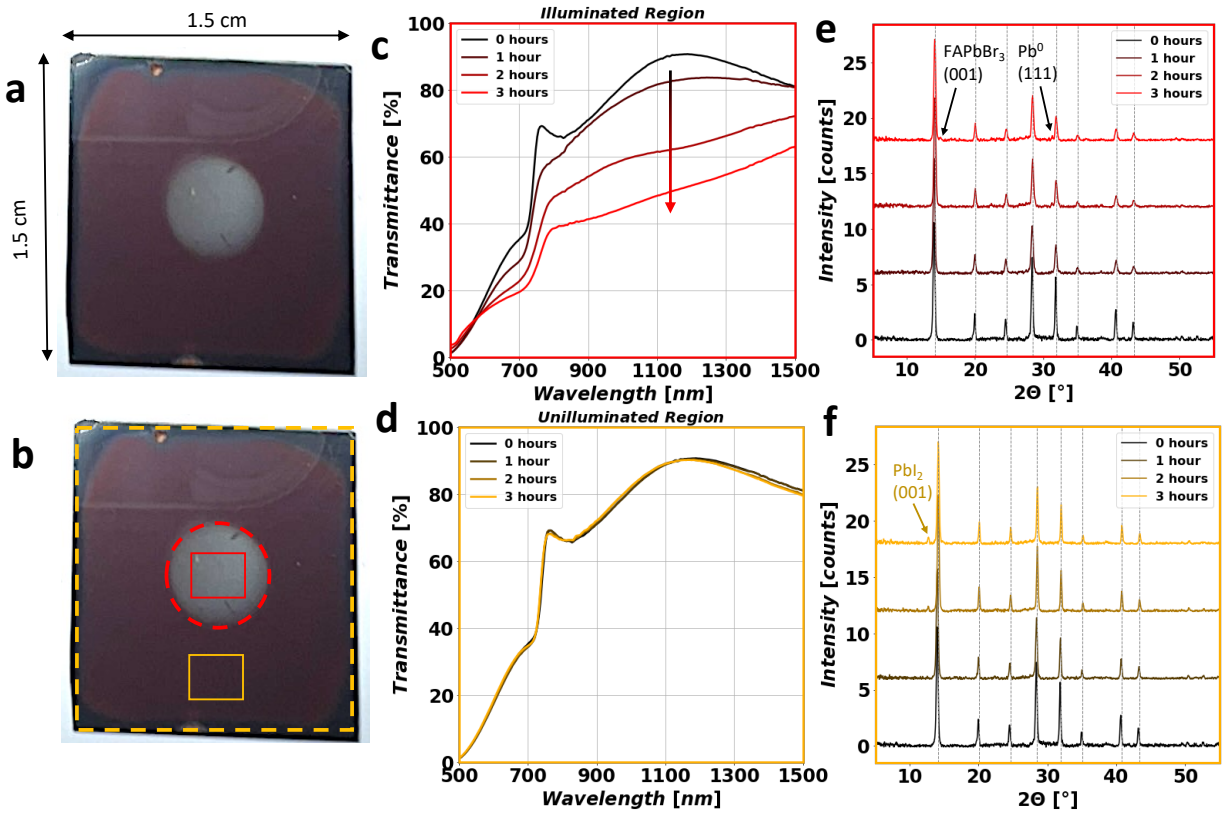

Figure 3.17. **Effect of high temperature exposure versus high temperature exposure with illumination.** *In-situ* degradation at 145°C, 1 sun green LED, flowing N_2**.** Image of the perovskite sample after 2 hours of degradation with (a) sample dimensions and (b) with reference to area illuminated by the microscope beam (red) and the unilluminated region outside the microscope beam (yellow). (c. d) Transmittance spectrum and diffraction pattern (e, f) over the course of degradation for the (c, e) illuminated region and (d, f) unilluminated region. The red and yellow rectangles in (b) are the approximate area through which the transmittance measurements were taken (as defined by a mask at the entrance of an integrating sphere); diffraction measurements are also taken inside these denoted areas (x-ray beam area defined by a 0.3 mm collimator).

3.8.10 ***Influence of Encapsulation on Degradation Rate***

To probe how the rate of Pb^0 formation is expected to change with encapsulation (and ensuing trapping of volatile decomposition products), we encapsulated $FA_{0.8}Cs_{0.2}Pb(I_{0.83}Br_{0.17})_3$ films with a thin layer of polymethyl methacrylate (PMMA) via a spin coating procedure. PMMA precursor solution was first prepared to a concentration of 5mg/ml in chlorobenzene and subsequently spin

coated onto bare perovskite samples, followed by an anneal at 100°C for 10 minutes. Encapsulation layer thickness was measured to be ~20 nm by stylus profilometry. An encapsulated and unencapsulated FACsPbIBr film were degraded side-by-side at 55°C under 1 sun illumination (broad-spectrum white LED) for 48 hours and characterized with UV-Vis-NIR absorption measurements. Here, we measure the absorptance (to avoid interference effects from the PMMA) by placing the sample in the center mount of an integrating sphere and plot the spectral absorbance as defined by the negative logarithm of one minus the absorptance. The results of this experiment are shown in Figure S11. Both encapsulated and unencapsulated films show negligible absorption in the sub bandgap region prior to degradation. After the period of degradation, the sub bandgap absorption increase is more pronounced in the unencapsulated film. This suggests that the trapping of volatile degradation products (e.g., I_2) slows the net formation of Pb^0.

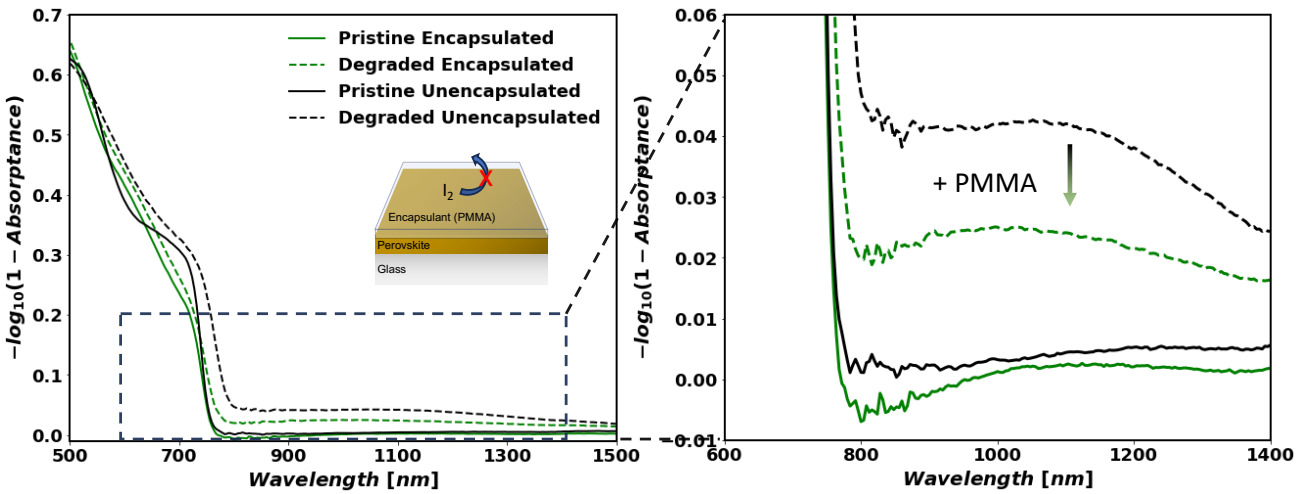

Figure 3.18. **Light-induced degradation of $FA_{0.8}Cs_{0.2}Pb(I_{0.83}Br_{0.17})_3$ with and without encapsulation.** Absorption versus wavelength for encapsulated (green) and unencapsulated (black) mixed-cation, mixed-halide films before (solid) and after (dashed) a 48-hour period of light-induced degradation. Conditions of the degradation were 55°C, 1 sun illumination from a broad-spectrum white LED.

4 Photooxidation Reaction Kinetics of Mixed Cation Mixed Halide Perovskite

This chapter describes experiments undertaken on $FA_{0.8}Cs_{0.2}Pb(I_{0.83}Br_{0.17})_3$ perovskite thin films to determine the reaction kinetics of photooxidation. Optical absorbance was tracked over the course of exposure to oxygen, water, and illumination. Using the initial rate of absorbance loss to estimate the rate of perovskite decomposition, we collect a comprehensive dataset spanning variations in each stressor. This dataset is used for modeling of the relevant photooxidation processes: dry photooxidation, water-accelerated photooxidation, and hydrate formation. This chapter was published in the Journal of Materials Chemistry A in October of 2025.[96] Reproduced with permission[96]; Copyright 2025 RSC Publishing.

4.1 Abstract

In this work, we use *in situ* absorbance measurements to study the kinetics of photooxidation of a representative mixed-cation mixed-halide perovskite composition, $FA_{0.8}Cs_{0.2}Pb(I_{0.83}Br_{0.17})_3$. We identify two dominant mechanisms of degradation in the presence of oxygen: a dry photooxidation pathway (with surface reaction rate of $(0.89 \pm 0.29) \times 10^{-9}$ mol·m^{-2}·s^{-1} at 25°C in dry air under 1 sun equivalent photon flux) and a water-accelerated photooxidation pathway (with a total surface reaction rate of $(1.8 \pm 0.9) \times 10^{-9}$ mol·m^{-2}·s^{-1} at 25°C in 50% relative humidity air under 1 sun equivalent photon flux). Notably, water vapor is found to increase the total decomposition rate at lower temperatures but decrease the rate at higher temperatures compared to dry conditions. We propose a temperature-dependent hydrate formation pathway to explain this behavior and outline a possible degradation mechanism for both the dry and water-accelerated photooxidation pathways. A mathematical expression for the initial decomposition rate as a function of temperature, ambient partial pressures of water vapor and oxygen, and above

bandgap photon flux is derived and fitted to observed rates based on the mechanistic analyses. These results provide key insights into the kinetics of decomposition for commercially relevant perovskite absorbers and may serve as a foundation for future device lifetime predictions when coupled with time-dependent mass transfer simulations.

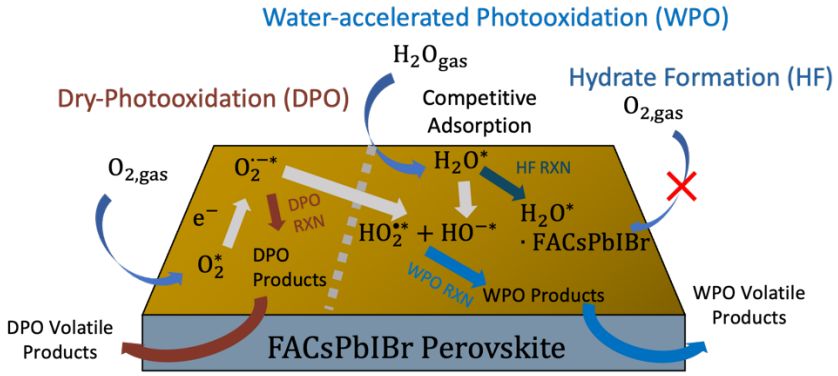

Figure 4.1. **Photooxidation Reaction Kinetics of Mixed Cation Mixed Halide Perovskite**

4.2 Introduction

Optoelectronic devices based on halide perovskite (HP) semiconductors are well-poised to decrease the cost of electricity generation from sunlight if their stability in the presence of oxygen and moisture can be managed by either encapsulation, gettering, or increased material stability.[25] HPs have an ABX_3 chemical formula and can be compositionally mixed at the A, B, and X sites with several organic and inorganic monovalent cations, divalent metal cations, and halides, respectively, to tailor the properties of the semiconductor. Of particular commercial interest are state-of-the-art perovskite solar cells (PSCs) which have high power conversion efficiency and low manufacturing costs using solution or vapor processing.[37,97] The tunable properties of halide perovskites enable their integration into single-junction, all-perovskite multijunction, and perovskite-on-silicon tandem solar cells. Currently, silicon photovoltaics (PV) dominate the global PV market, and perovskite-on-silicon tandem solar cells offer the possibility of incrementally

increasing the efficiency of the silicon-based PV without significant increased cost of manufacturing. Thus, HPs tuned for enhanced stability and an optimal bandgap (~1.65-1.70 eV[24]) when paired with a silicon bottom cell are of the most immediate commercial interest.

Alloyed lead-based HPs ($APbX_3$) have optimized optoelectronic performance when compositionally mixed at the A-site with formamidinium ($CH(NH_2)_2^+$, FA) and cesium (Cs^+) to optimize stability and performance[24] and at the X-site with bromine and iodine to tune the bandgap.[98] For X-site bromine fractions greater than ~20%, optoelectronic quality and halide phase segregation limit PSC device performance.[70,99,100] Thus, perovskite compositions optimized for efficient tandem architecture implementation have a ~1.65 eV bandgap (containing slightly less than 20% bromine at the X-site) which may then be made optically thin to achieve current matching in a monolithic tandem.[101] Despite the large interest in these so-called mixed-cation mixed-halide perovskites, detailed quantitative kinetic studies of the chemical reaction landscape for these materials are limited. Prior studies on FA-rich perovskites have measured the kinetics of degradation using in situ diffraction measurements,[102,103] in situ XPS,[68,104] and thermogravimetric analysis of gaseous products.[105] However, no prior works have quantitatively explored how the rate of surface reaction varies as a function of oxygen, moisture, illumination, and temperature.

In this work, we have studied the photooxidation kinetics of the perovskite $FA_{0.8}Cs_{0.2}Pb(I_{0.83}Br_{0.17})_3$, a representative composition for commercial application in tandem solar cells with a bandgap of ~1.66 eV. In previous reports on the decomposition of $MAPbI_3$[34] (MA=methylammonium, $CH_3NH_3^+$) and of $FA_{0.75}Cs_{0.25}Sn_{0.5}Pb_{0.5}I_3$[35], we used *in situ* measurements of above-bandgap optical transmittance ($\mathcal{T}$) to determine the decomposition reaction kinetics in response to environmental stressors. While the kinetic models presented in

these reports help reveal the underlying chemical mechanisms responsible for perovskite decomposition and clarify the critical roles played by oxygen, water, illumination, and temperature, they have also proven valuable as predictive features in machine learning models designed to forecast the stability of perovskite materials and devices.[35,82,87] They may also be coupled with simulations based on the drift-diffusion equations to estimate acceleration factors and predict the performance of photovoltaic modules.[106]

Recently, we have studied the reaction kinetics of light-induced metallic lead formation in $FA_{0.8}Cs_{0.2}Pb(I_{0.83}Br_{0.17})_3$ thin films using *in situ* sub-bandgap transmittance measurements.[36] In that work, we identified that light-induced decomposition in an inert environment produces reduced lead species whereas photooxidation decomposition (which dominates at >3% ambient oxygen) produces insulating wide bandgap decomposition products. Given this critical distinction, we conduct our kinetic study on $FA_{0.8}Cs_{0.2}Pb(I_{0.83}Br_{0.17})_3$ thin films under illumination with ambient oxygen levels above 3%, where photooxidation definitively governs decomposition. Under these conditions, above bandgap absorbance measurements exclusively probe photooxidative processes, unaffected by any reduced lead species formation, thereby enabling precise, unambiguous kinetic analysis. The thin films used throughout this study were fabricated by spin-coating with an anti-solvent wash and exhibit 1-sun quasi-fermi level splitting greater than 90% of the radiative limit in addition to ambipolar diffusion length exceeding 500 nm; their optoelectronic properties and solar cell device performance have been previously reported.[36]

Here, we measure the material decomposition rate under controlled environmental conditions in which temperature, relative humidity, oxygen partial pressure, and photon flux are all controlled (refer to SI section 4.6.1 and SI Figure 4.5 for further discussion of this experimental setup). As a degradation experiment proceeds, we collect a transmittance measurement *in situ*

(every 5 minutes). The change in absorbance with respect to time can be calculated from the following equation: $\frac{dA}{dt} = -log_{10}\left(\frac{\mathcal{T}_{t=t}}{\mathcal{T}_{t=0}}\right)$, assuming reflectance is changing minimally relative to transmittance, which is confirmed in SI section 4.6.2 (Figure 4.6). We focus on the 'early-time' degradation because the initial absorbance decay rate provides a direct measure of material stability and correlates with the onset of material optoelectronic quality and device performance decline.[82,87] From the change in absorbance, we determine the rate of perovskite loss[34–36] as: $r_{perovskite} = -\frac{\rho \cdot log_e 10}{M \cdot \alpha_o}\frac{dA}{dt}$, where ρ, M, and α_0 are the density, molecular weight, and absorption coefficient (at the probe wavelength, 630 nm in all studies presented) of the perovskite, respectively. Note that this is a 'rate of disappearance'. We conducted timeseries experiments (referred to as 'runs') across varied oxygen partial pressures, relative humidities, photon fluxes, and temperatures. The combined results, discussed below, inform our proposed decomposition pathways and underpin modeling of the overall decomposition rate as a function of each stressor.

4.3 Dry-Photooxidation (DPO) Kinetic Modeling

Figure 4.2 presents the timeseries absorbance decay and corresponding kinetic analyses for runs conducted across varied photon fluxes, oxygen concentrations (all >3%), and temperatures in humidity free environments. Figure 4.2a shows the change in absorbance over time for runs under 1 sun equivalent photon flux (1.5 x 10^{21} photons·m^{-2}·s^{-1} for a 1.66 eV bandgap material) from a 540 nm monochromatic LED in dry air over a range of temperatures. In all cases, the absorbance decreases over time, indicating the loss of light absorbing perovskite material due to its degradation to wider bandgap materials (E_g > 1.97 eV / 630 nm). At higher temperatures, the films exhibit a more rapid decline in absorbance. Figure 4.2b presents that data in an Arrhenius plot with an observed activation energy determined from the Arrhenius fit to be 0.56 $\pm$ 0.02 eV.

For dry conditions with ambient O_2 and illumination, the most plausible reactive species driving perovskite decomposition is the superoxide radical ($O_2^{*-\cdot}$),[34,84,107,108] formed when an adsorbed oxygen molecule takes up a conduction band electron. From a plausible reaction mechanism based on several elementary steps (see SI section 4.6.5 for the full derivation), we derive an expression that predicts the initial rate of perovskite loss in dry oxygen-containing environments under illumination. In this derivation, it is only necessary to assume that the elementary reaction step in which $O_2^{*-\cdot}$ reacts with the perovskite (step 4 DPO, below) is the rate determining step (RDS) and that all other elementary reactions are in quasi-equilibrium to arrive at a mathematical expression for the dry photooxidation rate. Note that, while oxygen and/or moisture (i.e., O_2^* and/or H_2O^***)** induced decomposition reactions have been found to decompose FA-rich lead halide perovskites,[109,110] the decomposition rate of the films under study in the dark in both dry and 50% RH air is negligible compared to the rate under one sun (Figure 4.7), consistent with prior reports.[111–113] In light of this finding, contributions from kinetically slow dark oxidation pathways are omitted in our modeling efforts throughout this manuscript. The proposed reaction pathway for DPO is the following:

$$h\nu \rightleftharpoons e^- + h^+ \qquad \text{1 DPO}$$
$$O_2 + [*] \rightleftharpoons O_2^* \qquad \text{2 DPO}$$
$$O_2^* + e^- \rightleftharpoons O_2^{\cdot -*} \qquad \text{3 DPO}$$
$$\mathbf{FA_{0.8}Cs_{0.2}Pb(I_{0.83}Br_{0.17})_3 + O_2^{\cdot -*} \rightarrow Degradation\ Products} \qquad \mathbf{4\ DPO}$$

X-ray diffraction patterns recorded during photooxidation exhibit no additional peaks over an extended period of degradation (SI Figure 4.8), indicating the absence of detectable crystalline degradation products. It is probable that degradation products are a mixture of amorphous compounds including delta phase pure or mixed cation/halide perovskites,[109] lead halides (PbX_2),[114] and residual organic decomposition products.[95] Vapor phase products are likely gaseous

diatomic halides (X_2)[115] and volatilized organic compounds.[95] Despite this, so long as the assumptions that step 4 DPO is the RDS and that the products do not absorb the incident probe 630 nm light hold, the resulting rate equation for DPO is the following:

$$r_{DPO} = k_{DPO} \frac{P_{O_2} n}{1 + K_2 P_{O_2} (1 + K_3 n)} \quad (1)$$

where $k_{DPO} = k_{0,DPO} \exp\left(\frac{-E_{A,DPO}^{eff}}{k_B T}\right)$, K_2 is the equilibrium constant associated with oxygen adsorption (step 2 DPO), and K_3 is the equilibrium constant associated with reduction of adsorbed oxygen (step 3 DPO).

The experimentally observed rate data at 85°C is plotted over a range of oxygen partial pressures (no humidity) under 1 sun photon flux in Figure 4.2c and over a range of photon fluxes in dry air in Figure 4.2d. While empirical sublinear exponential fits to the data are quite good (red traces in Figures 4.2c and 4.2d), the mechanistic models (blue and gold traces in Figures 4.2c and 4.2d, respectively) deliver an even better fit, providing important insights into the fidelity of the derived mathematical form. Note that we have previously determined that the activity of photoexcited species (electrons, n, in the case of photooxidation) scales as $I_{in}^{0.72}$ for this composition,[36] where I_{in} is the incident above bandgap photon flux. The mechanistic model in Figure 4.2d (gold trace) is fit based on this result.

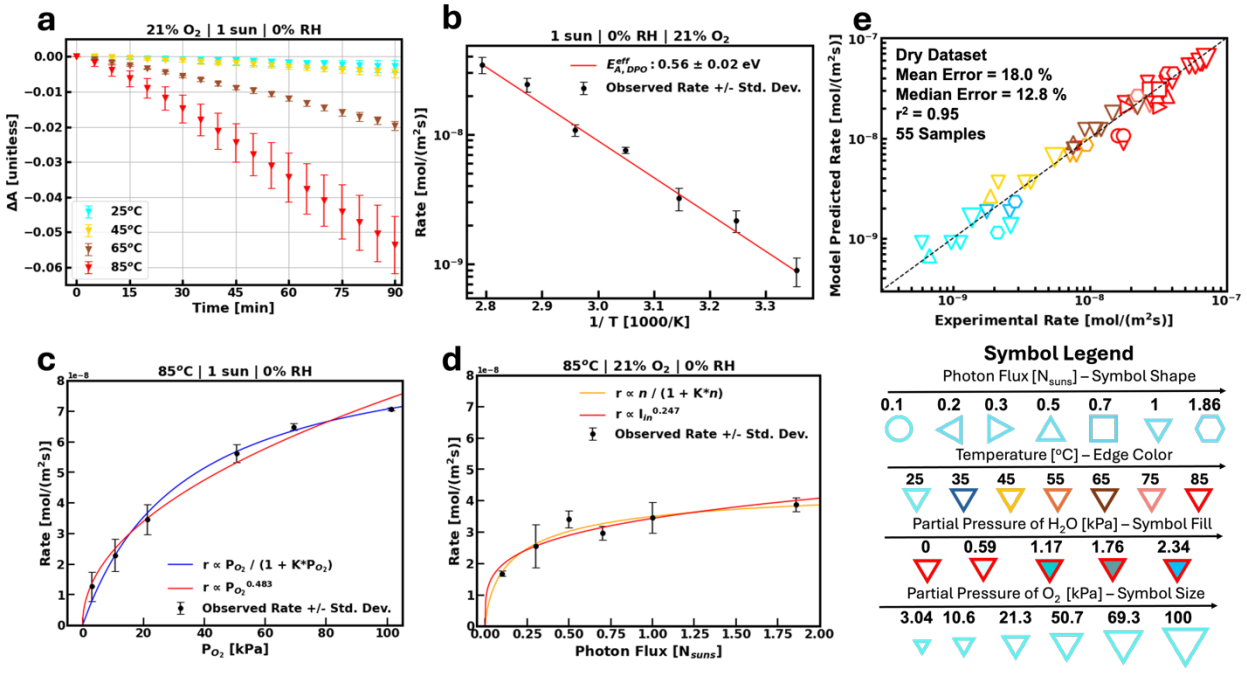

Figure 4.2**. Reaction Kinetics for Dry-Photooxidation (DPO).** (a) Change in absorbance over time for runs in dry air, 1 sun at 25°C, 45°C, 65°C, and 85°C. (b) Arrhenius plot for runs in dry air, 1 sun. Rate at 85°C versus (c) partial pressure of O_2 and (d) photon flux with empirical power law fits (red lines) and mechanistic model fits (blue and gold lines, respectively). (e) Parity plot for the dry photooxidation model. Data includes 55 total runs in humidity free environments over a range of O_2 partial pressure, photon fluxes, and temperatures demonstrating a strong fit of the model to the data (symbol legend included below).

Runs at 1 sun, 21% O_2 over a range of temperatures are used to determine the effective activation energy (Figure 4.2b). The entire dry dataset is used to determine the temperature independent prefactor, $k_{0,DPO}$, and the two equilibrium rate constants, K_2 and K_3, via the non-linear least-squares method. K_2 and K_3 may have temperature dependences. However, the fit to the data is quite good over a range of temperatures, oxygen partial pressures, and illumination intensities (Figure 4.2e), suggesting that associated temperature dependences are negligible over the temperature ranges in this study. Because the fitting parameters are non-linear, we applied a bootstrap procedure with 10,000 resamples (SI Figure 4.10) to estimate parameter uncertainty.[116] In this approach, we resampled the original data with replacement, refit the model to each synthetic

dataset, and derived standard deviations and 95% confidence intervals from the resulting parameter distributions. The final DPO parameter estimates and their uncertainty measures are presented in Table 4-1. The dry photooxidation model fits the dry dataset (55 samples) with a median error, mean error, and r^2 value of 12.8%, 18.0%, and 0.95, respectively, indicating an excellent fit of the data (Figure 4.2e). Expanded details for the fitting procedure for the dry photooxidation model are included in SI section 4.6.6.

4.4 Water-Accelerated Photooxidation (WPO) Kinetic Modeling

Having established a model for decomposition of $FA_{0.8}Cs_{0.2}Pb(I_{0.83}Br_{0.17})_3$ in dry oxygen containing environments under illumination, we next consider the influence of water on the overall degradation rate. Our previous reports identified that the introduction of water vapor to an oxygen containing atmosphere increases the net photooxidation rate of $MAPbI_3$[34] and the net oxidation rate of $FA_{0.75}Cs_{0.25}Sn_{0.5}Pb_{0.5}I_3$.[35] This behavior is more pronounced at lower temperatures than higher temperatures (posited to be a result of lower water surface coverage at higher temperatures compared to lower temperatures). Figure 4.3 shows the results of several 'on-off' experiments in which the absorbance change of the $FA_{0.8}Cs_{0.2}Pb(I_{0.83}Br_{0.17})_3$ films over the course of degradation is observed. These experiments are conducted in the same environmental chamber described in SI section 4.6.1. Each run begins in dry air at the specified temperature. After some time, humidity is introduced into the chamber (50% RH). Finally, the gas flow is switched back to dry air. We isolate the effect that the presence of water vapor has on the overall rate by comparing the absorbance change over time in each of the three windows. The volume of the environmental chamber used is ~300 ml, and at a flow rate of 3 L/min of inlet gas, it reaches 99% of the way to its new humidity set point in <30 seconds. This rapid exchange ensures that each humidity switch is effectively instantaneous for these measurements.

Interestingly, we observe a unique phenomenon in which the effect of adding water is a net increase in perovskite decomposition rate at lower temperatures (25ºC, 45ºC, Figures 4.3 a, b, respectively) and a net decrease in rate at higher temperatures (65ºC, 85ºC, Figure 4.3 c, d, respectively) compared to dry conditions. The associated water acceleration rate factor (50% RH rate divided by the initial dry rate) for these runs are 2.47, 2.68, 0.77, and 0.53 for the 25ºC, 45ºC, 65ºC, and 85ºC run, respectively. This counterintuitive result is confirmed with *ex situ* spectral absorption measurements (SI Figure 4.9).

Several surface reactions are possible that may produce other reactive oxygen species (ROSs) in addition to superoxide when water vapor is also present in the ambient. These include but are not limited to reactions between superoxide and adsorbed water to form hydroxyl radicals and the further reactions to form hydrogen peroxide (both of which are strong oxidizers capable of decomposing the perovskite[117,118]). The generation of these additional, plausible ROSs may activate alternative degradation pathways that, in total, could accelerate the decomposition rate of $FA_{0.8}Cs_{0.2}Pb(I_{0.83}Br_{0.17})_3$ relative to that under dry conditions. Water may also competitively adsorb with oxygen and/or form perovskite hydrates, reducing the surface coverage of oxygen and superoxide and by extension lowering the superoxide induced decomposition rate (dry photooxidation). If competitive adsorption of water effectively displaces oxygen and superoxide from the surface, the net decomposition rate of $FA_{0.8}Cs_{0.2}Pb(I_{0.83}Br_{0.17})_3$ under humid conditions could be reduced compared to that under dry conditions. We propose that the interplay between competitive adsorption and additional ROS generation underlies the observed temperature dependent decomposition behavior. This posited explanation is further explained in the subsequent paragraphs. We note that McAndrews et al. reported that moisture uptake can influence stability

through stress-relaxation mechanisms,[119] which we do not explore here but acknowledge as a possible contributing factor.

At lower temperatures, the exothermic water adsorption enthalpy outweighs the entropic penalty, increasing surface H_2O^* coverage relative to elevated temperatures. Adsorbed water then reacts with $O_2^{\cdot -*}$ to produce secondary ROSs such as hydroxyl radicals.[120] Hydroxyl radicals, or other secondary ROSs, open an alternative decomposition route with a lower transition-state energy barrier, yielding a reduced observed activation energy for the overall reaction.[34] Note that, in order for water to react with superoxide radicals, we assume that it must be present as unreacted adsorbed water (H_2O^*).

In contrast, at higher temperatures, there is a decrease in the net rate, implying the onset of a competing water-mediated process that suppresses the net photooxidation rate. This high-temperature slowdown motivates our proposal of a hydrated-perovskite pathway. We postulate that, in the presence of water vapor, a surface hydration reaction between pristine perovskite and gas-phase H_2O rapidly reaches quasi-equilibrium with ambient humidity (observed predominately at elevated temperatures), generating a hydrated perovskite phase. This process is fundamentally different from simple water adsorption, where an adsorbed molecule can detach and return the site to an active state. In the case of hydrate formation, vapor phase water first binds reversibly to an available site and, from this precursor state, undergoes a surface rearrangement with the perovskite lattice. This rearrangement produces a hydrate phase that annihilates the associated active site and prevents the bound water molecule from participating in further ROS-generating reactions. Only when the hydrate itself decomposes is the site restored.

It is important to note the role of site sampling dynamics in the proposed pathways. In all temperature regimes, adsorption sites are assumed to be sampled rapidly. Because both adsorption and desorption are fast, equilibrium coverage, not kinetic limitation, governs surface occupancy. At elevated temperatures, surface-bound free water (H_2O^*) coverage is low because excess thermal energy drives rapid desorption, keeping the equilibrium coverage minimal. However, the same thermal energy also enables hydrate formation at available active sites. Thus, due to rapid site sampling and the strong driving force for hydrate formation, these sites are quickly occupied, and the hydrate formation reaction proceeds.

In our model (below), we represent the hydrated species as (1) in quasi-equilibrium with gas-phase water, (2) kinetically inactive toward degradation over the experimental timescale, and (3) reversible in nature.[121–125] Functionally, an additional factor is introduced that accounts for water's effect on the total number of active adsorption sites on the perovskite surface. First-principles calculations of perovskite–water interactions show that hydrate formation likelihood depends on surface termination sites.[126] Combined experimental and theoretical studies further demonstrate that water-induced degradation varies across crystal facets.[127] To capture this surface heterogeneity, a factor that quantifies the fraction of total sites that are susceptible to hydrate formation ($f_{hydrate}$) is included.

The elementary reaction steps of the plausible water-accelerated photooxidation pathway can be written as the following:

$$h\nu \rightleftharpoons e^- + h^+ \qquad \text{1 WPO}$$
$$O_2 + [*] \rightleftharpoons O_2^* \qquad \text{2 WPO}$$
$$O_2^* + e^- \rightleftharpoons O_2^{\cdot -*} \qquad \text{3 WPO}$$
$$H_2O + [*] \rightleftharpoons H_2O^* \qquad \text{4 WPO}$$
$$\mathbf{H_2O^* + O_2^{\cdot -*} \rightleftharpoons OH^- + HO_2^{\cdot *}} \qquad \mathbf{5\ WPO}$$
$$FA_{0.8}Cs_{0.2}Pb(I_{0.83}Br_{0.17})_3 + OH^- \rightarrow \text{Degradation Products} \qquad \text{6 WPO}$$

Note that ROSs aside from OH^- may form under these conditions and contribute to decomposition; here, we choose to model the hydroxyl mediated pathway while recognizing that alternative ROS-driven routes may also operate. It is assumed that surface adsorbed water (H_2O^*) remains in the low-coverage (linear) regime of the Langmuir isotherm, allowing omission from the denominator of equation 2 below. Using the rate-determining step approximation (step 5 WPO) with all prior steps in quasi-equilibrium, the resulting WPO rate equation is:

$$r_{WPO} = k_{WPO} \frac{P_{O_2} n P_{H_2O}}{(1 + K_2 P_{O_2}(1 + K_3 n))^2} \tag{2}$$

where $k_{WPO} = k_{0,WPO} \exp\left(\frac{-E_{A,WPO}^{eff}}{k_B T}\right)$, and K_2 and K_3 are again equilibrium constants associated with oxygen adsorption and adsorbed oxygen reduction by conduction band electrons, respectively. The complete derivation of the WPO rate equation is included in SI section 4.6.7.

The pathway for the hydrated perovskite formation can be written as the following:

$$H_2O + [*]_{avail} \rightleftharpoons H_2O^* \quad \text{1 HF}$$
$$H_2O^* + FA_{0.8}Cs_{0.2}Pb(I_{0.83}Br_{0.17})_3 \rightleftharpoons H_2O^* \cdot FA_{0.8}Cs_{0.2}Pb(I_{0.83}Br_{0.17})_3 \quad \text{2HF}$$

An expression that captures the reduction in total surface adsorption sites ($[*]_{total}$) due to the hydrate formation (HF) pathway is presented below (equation 3). Because $[*]_{total}$ is contained within the prefactor of the rate equations for both the DPO and WPO pathways (SI sections 4.6.6 and 4.6.7), it is necessary to modify both the DPO and WPO rate equations to account for relative changes in this value. A site balance on total adsorption sites, incorporating temperature-dependent equilibrium constants for hydrate formation, yields equation 3 below. A complete derivation is provided in SI section 4.6.8. The following equation quantifies the fraction of total available active adsorption sites relative to the total ($f_{active} = \frac{[*]_{available}}{[*]_{total}}$):

$$f_{active} = 1 - f_{hydrate}\frac{K_{hydrate}P_{H_2O}}{1 + K_2P_{O_2}(1 + K_3n) + K_{hydrate}P_{H_2O}} \quad (3)$$

where $K_{hydrate}$ is a temperature dependent equilibrium constant associated with hydrate formation and is equal to $K_{0,hydrate}\exp\left(\frac{-\Delta H^{eff}_{hydrate}}{k_BT}\right)$. $f_{hydrate}$ is the fraction of total sites that are available to hydrate formation ($\frac{[*]_{act,water}}{[*]_{total}}$). The fitting of the remaining parameters that define the WPO and HF pathways is discussed below.

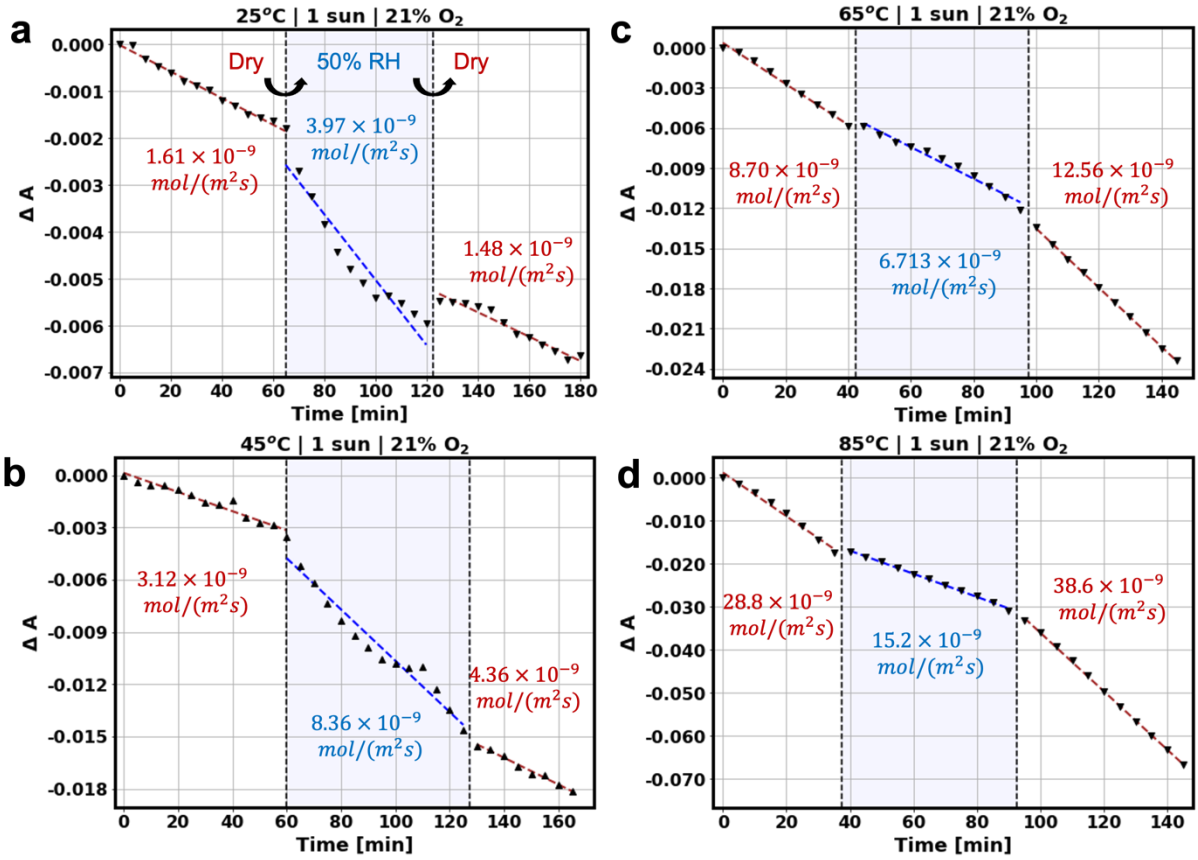

Figure 4.3. **Water Vapor 'On-off' Absorbance Tracking.** Degradation at 1 sun equivalent illumination in air at (a) 25°C, (b) 45°C, (c) 65°C, and (d) 85°C. Experiments start in dry air, followed by 50% RH air, and then are switched back to dry air. The calculated rate for each condition is calculated and shown in the plots. Note the difference in range of the change of absorbance for each temperature.

From the derivations for DPO, WPO, and the hydrate formation reaction, a total rate equation for the photooxidation of $FA_{0.8}Cs_{0.2}Pb(I_{0.83}Br_{0.17})_3$ in oxygen containing environments under illumination is established. We begin by noting that the total rate is assumed to be a sum of the contributions from the dry-photooxidation and water-accelerated photooxidation pathway:

$$r_{total} = r_{DPO} + r_{WPO}$$

Including the effect that hydrate formation has on total adsorption sites, the total photooxidation reaction rate can be written as the following:

$$r_{total} = \left[k_{DPO}\frac{P_{O_2}n}{1 + K_2P_{O_2}(1 + K_3n)} + k_{WPO}\frac{P_{O_2}nP_{H_2O}}{(1 + K_2P_{O_2}(1 + K_3n))^2}\right] \cdot \left[1 - f_{hydrate}\frac{K_{hydrate}P_{H_2O}}{1+K_2P_{O_2}(1 + K_3n) + K_{hydrate}P_{H_2O}}\right] \quad (4)$$

Figure 4.4a shows the change in absorbance over time for runs in 50% RH at 25, 45, 65, and 85°C. Reaction rates increase with temperature but less steeply than in dry air. Figure 4.4b is an Arrhenius plot in which runs at 100% RH (dark blue) and 50% RH (light blue) are compared to the dry-photooxidation model. At low temperatures (25-45°C), we observe a decrease in the apparent activation energy with an increase in relative humidity. The magnitude of the observed rate is also higher than the dry-photooxidation rate. These two results are commensurate with our initial hypothesis of an additional water-accelerated photooxidation pathway that occurs predominately at lower temperatures. Consistent with prior results on other perovskite compositions, this pathway exhibits a negative effective activation energy because of the substantial enthalpy of water adsorption.[34,35] However, at high temperatures (45-85°C), the apparent activation energy is nearly identical for runs at 50% RH and 100% RH. This observation supports the hydrate formation hypothesis but also indicates that available hydrate formation sites

are becoming saturated, with the surface coverage term approaching unity under these conditions. Figure 4.4c is a plot of the rate of disappearance of perovskite versus the partial pressure of water vapor for runs at 85°C under 1 sun in air. Here, the rate is accounted for almost entirely by reactions precipitated by the formation of superoxide radical ($[H_2O^*]$ is expected to be very low while $[H_2O^* \cdot FA_{0.8}Cs_{0.2}Pb(I_{0.83}Br_{0.17})_3]$ is expected to be appreciable at this temperature). We model the rate (the red line) as the dry-photooxidation rate at 85°C in dry air under 1 sun multiplied by the hydrate formation factor (equation 3). This fit provides an estimate for the fraction of total adsorption sites available for hydrate formation ($f_{hydrate} = 0.55$) in addition to a reference equilibrium constant for hydrate formation ($K_{hydrate}(T = 85^oC) = 47\ kPa^{-1}$).

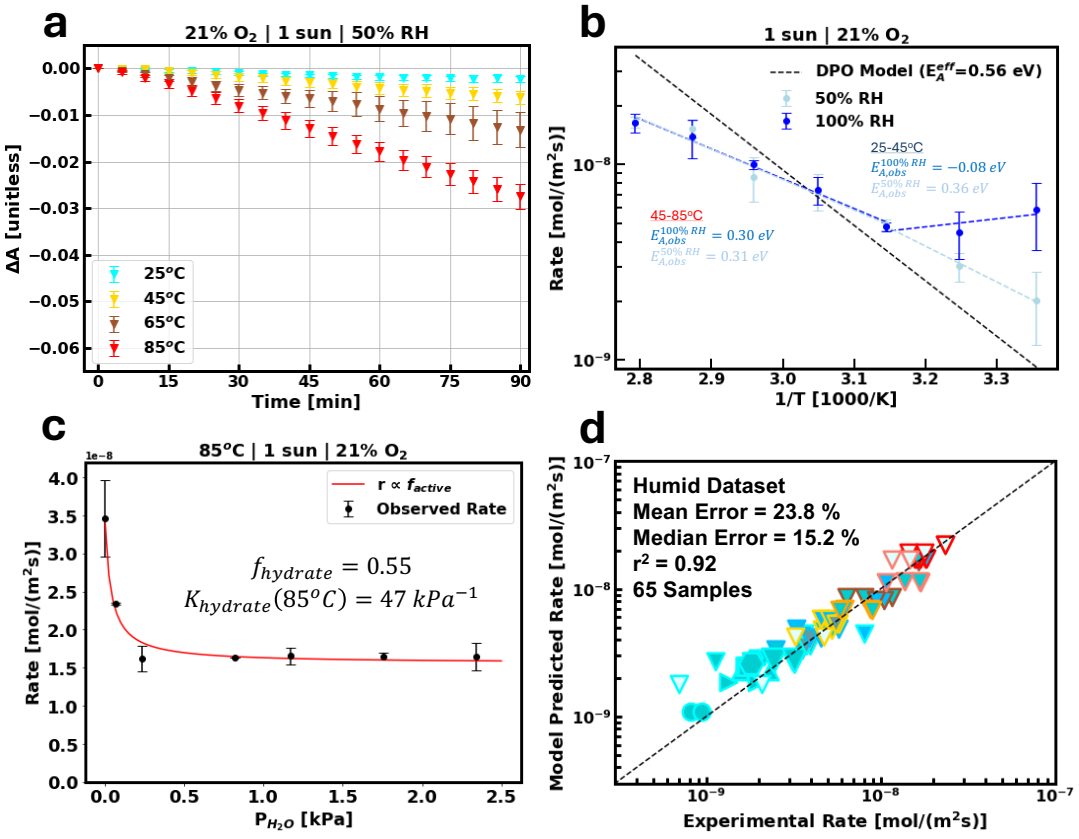

Figure 4.4. **Reaction Kinetics for Water-Accelerated Photooxidation and Hydrate Formation.** (a) Change in absorbance over time for runs in 50% RH air, 1 sun at 25°C, 45°C, 65°C, and 85°C.

(b) Arrhenius plot for runs in 50% and 100% RH compared to DPO model predicted rates. Apparent activation energies for low temperature (25-45ºC) and high temperature (45-85ºC) runs are shown. (c) Observed rate versus partial pressure of water vapor at 85ºC, 21% O_2, 1 sun illumination with model fit. (d) Parity plot for the humid dataset (65 total samples across a range of conditions with non-zero humidity, refer to Fig 1 for symbol legend).

To fit the remaining parameters ($E_{A,WPO}^{eff}$, $\Delta H_{hydrate}^{eff}$, $k_{0,WPO}$) that define the total rate (equation 4), we divided the 65-sample humid dataset into multiple subsets defined by distinct temperature ranges and performed a grid search optimization.[128] This exhaustive search is necessary because activation energies appear in the exponent of the Arrhenius term, making gradient-based methods extremely sensitive to initial guesses and prone to failure unless seeded very close to the true values. The grid search involves selecting pairs of $E_{A,WPO}^{eff}$ and $\Delta H_{hydrate}^{eff}$ values over a broad range and fitting $k_{0,WPO}$ to optimize the fit. The results of these grid searches are presented in SI section 4.6.9 and SI Figure 4.11. The most optimal parameters based on a minimization of the sum of squared residuals are when of the parameters $E_{A,WPO}^{eff}$ and $\Delta H_{hydrate}^{eff}$ are equal to -0.12 eV and 1.48 eV, respectively.

In agreement with our prior work, we find that a negative effective activation energy associated with WPO provides a strong fit to the data. We also find a relatively high activation energy associated with hydrate formation which indicates that this process has a large energy barrier to formation in this perovskite composition. As discussed in SI section 4.6.8, $\Delta H_{hydrate}^{eff}$ is the sum of the enthalpy of adsorption for water vapor and the enthalpy of the hydrate formation reaction. For the humid dataset, we achieve an excellent fit of the data with a median error, mean error, and r^2 value of 15.2%, 23.8%, and 0.92, respectively (Figure 4.4d). We have also included a bootstrap procedure (SI section 4.6.9, SI Figure 4.12) identical to that done for the DPO parameters to estimate the uncertainty of the fitted WPO and HF parameters. The final WPO and HF parameter

estimates and their uncertainties are included in Table 4-1. Expanded details for the fitting procedure for the water-accelerated photooxidation model and hydrate formation model are included in SI section 4.6.9.

Table 4-1. **Best-Fit Parameters for the Full Kinetic Photooxidation Model for $FA_{0.8}Cs_{0.2}Pb(I_{0.83}Br_{0.17})_3$ Thin Films**

Parameter	Value	Units
$k_{o,DPO}$	$(1.5 \pm 0.2) \times 10^{-16}$	$\text{mol} \cdot \text{m}^{-2} \cdot \text{s}^{-1} \cdot \text{kPa}^{-1} \cdot (\text{photons} \cdot \text{m}^{-2} \cdot \text{s}^{-1})^{-0.72}$
$E_{A,\,eff}^{DPO}$	0.56 ± 0.02	eV
K_2	$(9.5 \pm 1.2) \times 10^{-4}$	kPa^{-1}
K_3	$(2.3 \pm 0.4) \times 10^{-14}$	$(\text{photons} \cdot \text{m}^{-2} \cdot \text{s}^{-1})^{-0.72}$
$k_{o,WPO}$	$(1.3 \pm 0.2) \times 10^{-27}$	$\text{mol} \cdot \text{m}^{-2} \cdot \text{s}^{-1} \cdot \text{kPa}^{-2} \cdot (\text{photons} \cdot \text{m}^{-2} \cdot \text{s}^{-1})^{-0.72}$
$E_{A,\,eff}^{WPO}$	-0.12 ± 0.12	eV
$f_{hydrate}$	0.55	unitless
$K_{o,hydrate}$	3.2×10^{22}	kPa^{-1}
$\Delta H_{hydrate}^{eff}$	1.5 ± 0.4	eV

4.5 Conclusion

In conclusion, we identify two distinct oxygen and light-induced degradation pathways for $FA_{0.8}Cs_{0.2}Pb(I_{0.83}Br_{0.17})_3$ absorbers: (1) dry photooxidation ($E_{A,DPO}^{eff}$ = 0.56 eV, with only superoxide radical as the oxidizing agent) and (2) water-accelerated photooxidation ($E_{A,WPO}^{eff}$= −0.12 eV, includes secondary ROSs as reactants). In addition, we demonstrate that water vapor retards decomposition at elevated temperatures in an oxygen containing environment, which is posited to be a result of hydrate formation that decreases the number of available surface adsorption sites for oxygen. A two-step reaction pathway for hydrate formation is used to derive an expression that accurately quantifies water's effect on total photooxidation rate. A complete rate expression for the chemical decomposition of this representative mixed-cation mixed-halide perovskite is reported and predicts the initial rate of degradation with low error (~14% median error for the total dataset of 120 runs across a range of oxygen and water partial pressures, photon fluxes, and temperatures, Fig S10). This model is determined from degradation runs with greater than 3% ambient oxygen. However, in principle it provides an estimate at lower oxygen concentrations as well. It is, however, important to note that the unscavenged electrons at low O_2 partial pressures may react with Pb^{2+} to reduce it.[36,60,129] Our model should be accurate in quantifying the rate of perovskite loss due to reaction with superoxide and other ROSs but will miss the Pb^{2+} reduction reaction at low O_2 partial pressure. To validate that the identified mechanisms are not unique to $FA_{0.8}Cs_{0.2}Pb(I_{0.83}Br_{0.17})_3$, we performed additional tests on $FA_{0.8}Cs_{0.2}Pb(I_{0.9}Br_{0.1})_3$ and $FA_{0.8}Cs_{0.2}PbI_3$ thin films (SI Figure 4.15), which showed similar trends under combined oxygen, humidity, and illumination stresses. This model may also be useful in developing predictions of module lifetime when coupled with models of moisture and oxygen ingress through an

encapsulant, as well as the effects of slower escape and build-up of gaseous decomposition products.

4.6 Supporting Information

4.6.1 Experimental Methods and Film Characterization

Sample Preparation: $FA_{0.8}Cs_{0.2}Pb(I_{0.83}Br_{0.17})_3$ thin films were fabricated by a spin-coating procedure as described previously.[36] In summary, stoichiometric CsI (FISHER SCIENTIFIC, 99.998%), FAI (Greatcell Solar Materials, >99.99%), PbI_2 (TCI AMERICA, 99.99%, trace metals basis) and $PbBr_2$ (TCI AMERICA, >98.0%) were dissolved in in 1/1 vol/vol N-methyl-2-pyrrolidone (NMP)/dimethylformamide (DMF) and allowed to dissolve overnight to create precursor inks. 50 µL of filtered precursor ink was spin coated on clean glass slides (4-part sonication in Alconox and DI water, then DI water, then acetone, then 2-propanol followed by air plasma treatment, all for 10 minutes) at 4000 rpm for 45 sec followed by a 0.6 ml of toluene antisolvent drip with 15 sec remaining in the cycle. Samples were annealed at 120°C for 15 minutes and averaged ~280 nm in thickness.

***In-situ* Decomposition Rate Experiments**: Bare samples are placed in a Linkam Scientific LTSE420-P environmental test chamber, outfitted with an electric heater, gas ports, and windows above and below the sample to allow for light excitation and transmission. The oxygen content in the atmosphere was maintained by mixing pure nitrogen (99.998%, 4.8 grade), air (0.0 grade "Extra Dry"), and/or pure oxygen (99.5%, technical diving grade) with a set of Omega FMA5400/5500 mass flow controllers and setting the total flow rate to 3L/min. For runs in humidified gas, the flow was bubbled through a H_2O/glycerol bath (H_2O/glycerol ratio set to achieve a specific relative humidity which was determined with a Fisher Scientific TraceableTM hygrometer, PN #11-661- 18). For 'dry' runs in humidity free environments, the gas stream was passed through a desiccant column to eliminate trace moisture present in the gas cylinders. We use a calibrated 540 nm LED (Lumencor SpectraX Light Engine, FWHM = 29nm) as the light source in a metallurgical upright microscope (Olympus BX53M, equipped with an Olympus 5x objective lens), and adjust the input power based on the sample band gap to obtain the desired photon flux. Periodically (every 5 minutes), we switch off the degradation beam and collect a measurement of transmittance with a 630 nm LED light source (FWHM = 14nm). The transmittance is measured by short-circuit current measurements (detected using a Keithley 2400 source/measure unit) from an OSI Optoelectronics UV-100DQ photodiode placed underneath the sample. All data collection is automated with a Python Master control.

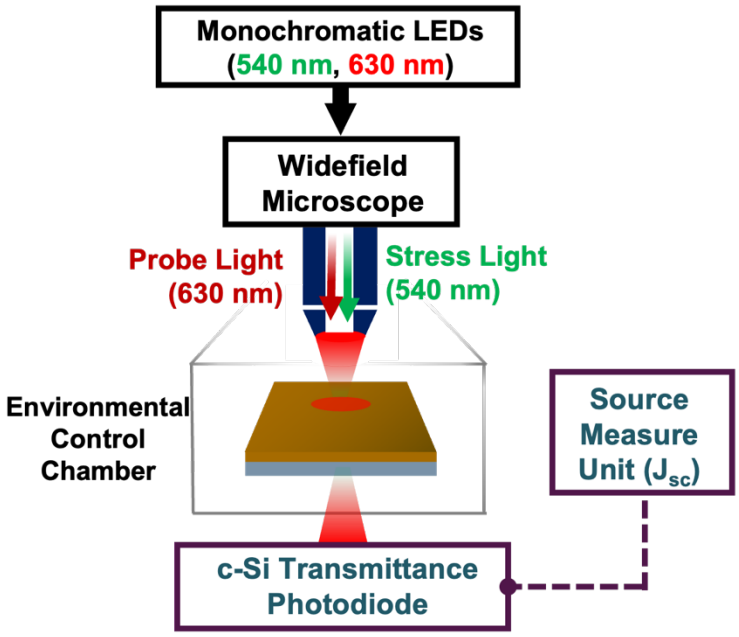

Figure 4.5. **Schematic of Degradation Setup**.

1.3 ***Ex-situ Film Characterization***:

X-ray Diffraction (XRD): Thin film X-ray diffraction measurements were collected with a Bruker D8 Discover instrument equipped with a Pilatus 100K large area 2D detector and a Cu anode (wavelength 1.542 Å, Kα radiation). The X-ray beam size was defined with a 0.3 mm collimator. UV-vis Absorbance: Optical absorbance spectra were collected from a PerkinElmer Lambda 1050 UV/vis/NIR spectrometer with an integrating sphere in laboratory atmosphere. Absorbance was calculated from separate measurements of sample percent transmittance and sample percent absorptance.

Table 4-2. **$FA_{0.8}Cs_{0.2}Pb(I_{0.83}Br_{0.17})_3$ Film Properties**

Perovskite Material Property	Value	Units
Density	4201	kg/m^3
Abs. Coeff. 630 nm	4.53×10^4	cm^{-1}
Molar Mass	0.627	kg/mol

4.6.2 Determination of Early-time Absorbance Changes from In-situ Transmittance Measurements

The in-situ transmittance measurements presented in the main text were conducted with a 630 nm LED narrowed with a 630 nm bandpass filter (FWHM = 14 nm). To determine if this wavelength is appropriate for accurate absorbance measurements from transmittance alone, we conducted ex-situ measurements of reflectance and transmittance on $FA_{0.8}Cs_{0.2}Pb(I_{0.83}Br_{0.17})_3$ thin films to calculate total absorbance change over the course of a period of photooxidation. The results of these measurements are shown below in Figure 4.6. As shown in Figure 4.6d, the absorbance change calculated over a 180-minute period of degradation from transmittance alone (approximate, blue) is very similar to that calculated from both transmittance and reflectance (absolute, red). This indicates that the reflectance change is small at this wavelength during early times of degradation. Thus, we deem it appropriate to assess absorbance changes with transmittance changes alone as done in the main text and as done previously.[34–36]

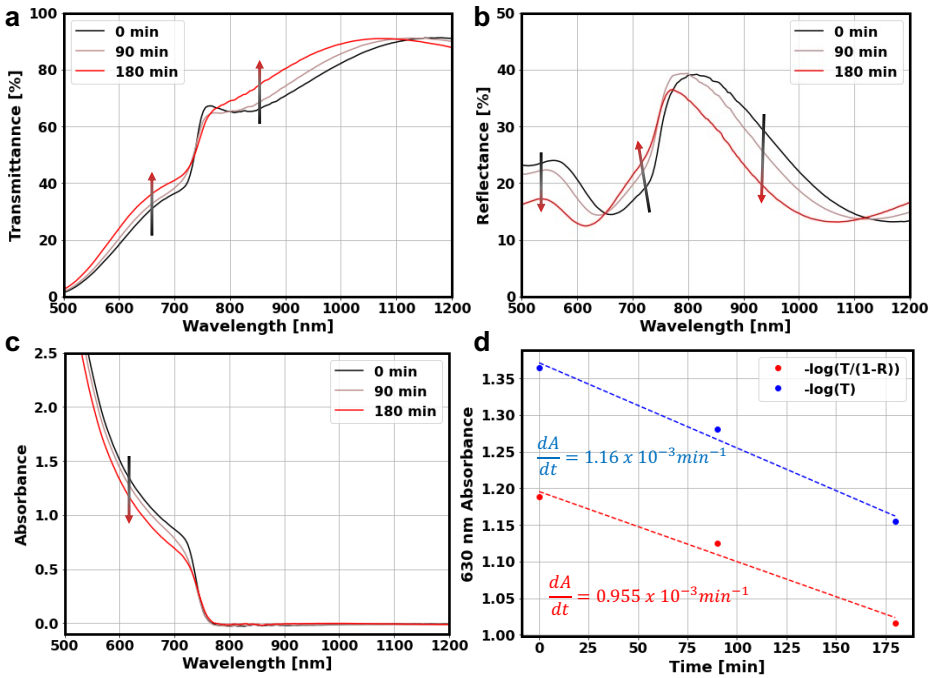

Figure 4.6. **Selection of Accurate Probe Wavelength.** (a) Transmittance, (b) reflectance, and (c) absorbance as a function of wavelength for a $FA_{0.8}Cs_{0.2}Pb(I_{0.83}Br_{0.17})_3$ thin film stressed in ambient lab air (~60%RH, 25°C) under a 1 sun equivalent illumination from a solar simulator. The sample

is removed periodically for UV-vis measurements. (d) Absorbance at 630 nm over the course of degradation calculated from transmittance and reflectance (red) and transmittance alone (blue). The results indicate that 630 nm transmittance measurements capture absorbance changes with little error (~20%) due to reflectance changes. Data were collected using a Perkin-Elmer Lambda 1050 UV/Vis/NIR spectrometer equipped with an integrating sphere. Transmittance and reflectance were independently measured by placing the sample on the front exterior mount and rear exterior mount of the integrating sphere.

4.6.3 Comparing Photooxidation and Oxidation

To determine if pure oxidation processes (i.e., those facilitated by oxygen and/or oxygen plus water without illumination) contribute to the decomposition rate, we conducted runs in which the samples were kept in the dark at 85^{o}C in dry air and 50%RH air. Because the probe transmittance beam inherently exposes the sample to above bandgap photons that can cause photooxidation decomposition (~0.33 suns exposure for ~20 sec per cycle), sample transmittance was only measured once every two hours. The results of these experiments are shown in Figure 4.7 below alongside representative runs at 1 sun (sampling transmittance at the standard time interval of 5 minutes with the 540 nm continuously on). We observe that decomposition is almost completely retarded, indicating that oxidation plays a negligible role in the total decomposition rate. Oxidation can almost certainly be ignored when assessing the stability of these materials for the application of light absorbers in solar cells.

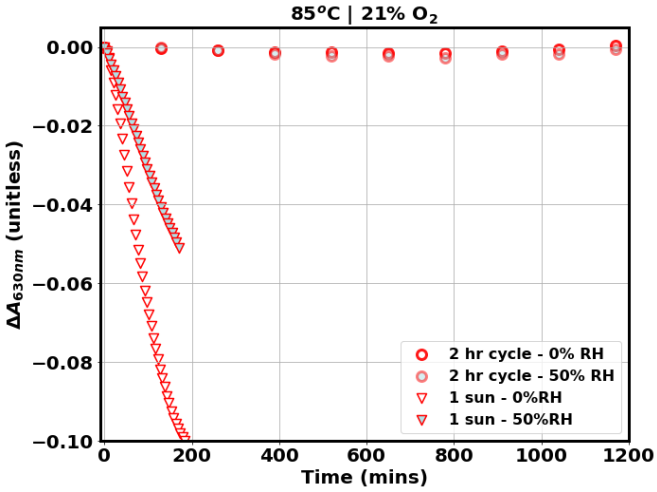

Figure 4.7. **Comparing photooxidation and oxidation.** In situ absorbance measurements at of $FA_{0.8}Cs_{0.2}Pb(I_{0.83}Br_{0.17})_3$ thin films degraded at 1 sun with 5-minute cycles and 0 sun with 2-hour cycles in 50% RH air and dry air, respectively, at 85°C.

4.6.4 Ex-situ Diffraction and Absorption Measurements During Photooxidation

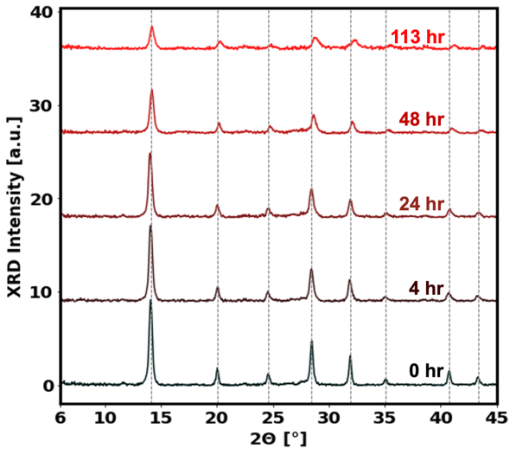

Figure 4.8**. Ex-situ X-ray Diffraction.** Diffraction patterns of $FA_{0.8}Cs_{0.2}Pb(I_{0.83}Br_{0.17})_3$ thin films over the course of degradation in lab air (~40% RH air) under ~1 sun illumination from a white light LED. No discernable peaks appear outside of the main perovskite peaks (denoted with vertical dashed lines) despite significant reduction in perovskite peak intensities. All perovskite peaks shift to higher angles, indicated a lattice contraction that is commensurate with loss of organic formamidinium or I_2 gas.

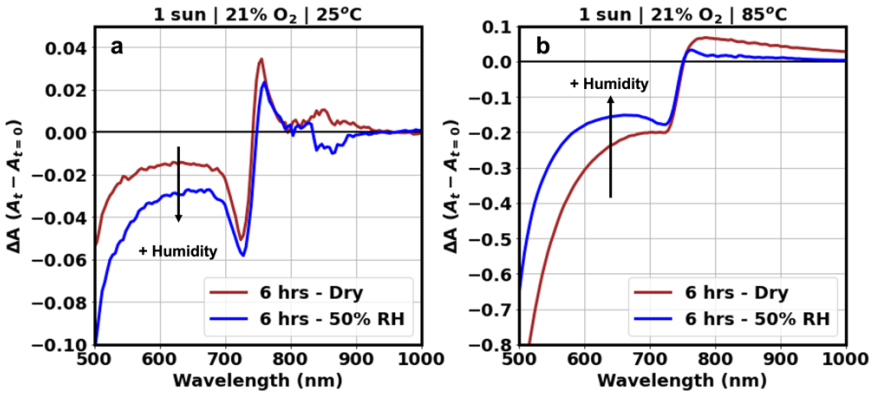

Figure 4.9**. Ex-situ UV-vis Absorbance During Photooxidation.** Absorbance measurements of $FA_{0.8}Cs_{0.2}Pb(I_{0.83}Br_{0.17})_3$ thin films degraded in air at (a) 25ºC and at (b) 85ºC over a period of 6 hours with (blue traces, 50% RH) and without moisture (brown traces). All samples were illuminated with ~1 sun illumination from a white light LED and measurements were taken of the pristine films before and after 6 hours of exposure. The results agree with those in the main text that the rate of degradation increases at lower temperatures and decreases at higher temperatures for samples under illumination with the addition of humidity to dry air.

4.6.5 Derivation of Rate Expression for Dry Photooxidation

For dry photooxidation, it is most likely that the perovskite decomposition proceeds through a reaction with superoxide radical. The process begins by absorption of a photon (step 1) to create an electron in the conduction band and a hole in the valence band. Oxygen then adsorbs (step 2) to the surface at a surface adsorption site (suggested to be at iodide vacancies[84,130]).The adsorbed oxygen then takes up a photoexcited electron from the conduction band. The superoxide radical then reacts with the perovskite (step 4) in what is assumed to be the rate determining step (bolded).

$$h\nu \rightleftharpoons e^- + h^+ \quad \text{1 DPO}$$
$$O_2 + [*] \rightleftharpoons O_2^* \quad \text{2 DPO}$$
$$O_2^* + e^- \rightleftharpoons O_2^{\cdot -*} \quad \text{3 DPO}$$
$$\mathbf{FA_{0.8}Cs_{0.2}Pb(I_{0.83}Br_{0.17})_3 + O_2^{\cdot -*} \rightarrow Degradation\ Products} \quad \textbf{4 DPO}$$

We can first note that the rate of perovskite loss is equal to the rate determining step (assuming that all prior steps are in quasi-equilibrium):

$$r_{pero} = -r_4$$

Applying that step 4 is rate limiting such that it is much slower than steps 1-3, we simplify the above to:

$$r_3 = r_{-3}$$
$$r_2 + r_{-3} = r_3 + r_{-2}$$
$$r_2 = r_{-2}$$

Solving for r_{FAPbI}:

$$r_{pero} = -k_4[O_2^{\cdot -*}]a_{FAPbI}$$

Solving for $[O_2^{\cdot -*}]$:

$$r_3 = r_{-3}$$
$$k_3[O_2^*]n = k_{-3}[O_2^{\cdot -*}]$$
$$[O_2^{\cdot -*}] = K_{eq,3}n[O_2^*]$$
$$r_2 = r_{-2}$$
$$k_2 P_{O_2}[*] = k_{-2}[O_2^*]$$
$$[O_2^*] = K_{eq,2}P_{O_2}[*]$$
$$[O_2^{\cdot -*}] = K_{eq,3}K_{eq,2}P_{O_2}n[*]$$

Doing a site balance for $[*]$:

$$[*]_T = [*] + [O_2^*] + [O_2^{\cdot -*}]$$
$$[*]_T = [*] + \frac{r_{-2}}{k_{-2}} + \frac{r_{-3}}{k_{-3}}$$
$$[*]_T = [*] + [O_2^*] + [O_2^{\cdot -*}]$$
$$[*]_T = [*] + K_{eq,2}P_{O_2}[*] + K_{eq,3}K_{eq,2}P_{O_2}n[*]$$
$$[*]_T = [*](1 + K_{eq,2}P_{O_2}(1 + K_{eq,3}n))$$
$$\frac{[*]_T}{(1 + K_{eq,2}P_{O_2}(1 + K_{eq,3}n))} = [*]$$
$$r_{pero} = -k_4[O_2^{\cdot -*}]a_{FAPbI} = -k_4K_{eq,3}K_{eq,2}a_{FAPbI}[*]_T \frac{P_{O_2}n}{(1+K_{eq,2}P_{O_2}(1+K_{eq,3}n))}$$
$$r_{DPO} = \frac{k_{DPO}P_{O_2}n}{1 + K_2P_{O_2}(1 + K_3n)}$$

Under conditions where water vapor is also present, we need to account for the reduction in total active sit concentration due to hydrate formation. This is done in SI section 8.

4.6.6 Model Fitting and Bootstrapping for Dry Photooxidation

To estimate the uncertainty of the parameter fits, we perform a bootstrapping procedure. The procedure involves generating 10,000 datasets, each of which is created by sampling with replacement from the dry dataset until the dataset size is matched (55 samples). From each of the datasets, the parameters that define the DPO equation are fit using curve_fit from the scipy package in python. The results of these 10,000 iterations are shown below as histograms and are used to determine the uncertainty associated with the fits.

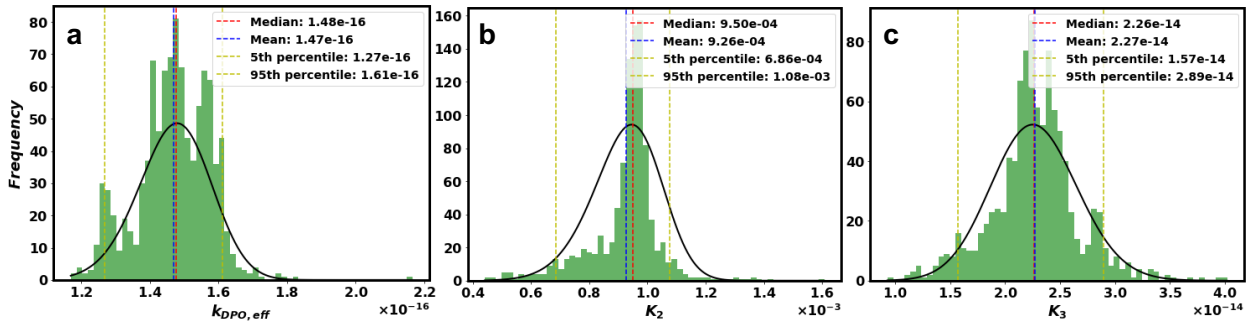

Figure 4.10. **Bootstrapping Procedure for Dry Photooxidation Parameters.** Histogram results of bootstrapping procedure over 10,000 iterations for (a) $k_{0,DPO}$,(b) $K_{2,}$, and (c) $K_{3,}$. Mean, median, 5th percentile, and 95th percentile of the bootstrap fits is included as vertical lines. Black traces over the histograms are skewed gaussians fit to the data (arbitrarily scaled).

Table 4-3. **Explanation of Fitting Procedure for Dry-Photooxidation Parameters**

Parameter	Subset of the data used for fitting
$E_{A,DPO}^{eff}$	Runs in dry air under 1 sun equivalent illumination from 25°C to 85°C
$k_{0,DPO}$	Runs in dry oxygen containing environments (3 kPa to 101 kPa) with varying illumination (0.1 to 1.86 suns)
K_2	Runs in dry oxygen containing environments (3 kPa to 101 kPa) with varying illumination (0.1 to 1.86 suns)
K_3	Runs in dry oxygen containing environments (3 kPa to 101 kPa) with varying illumination (0.1 to 1.86 suns)

4.6.7 Derivation of Rate Expression for Water-accelerated Photooxidation

In the presence of water and oxygen, we observe an increased rate of decomposition compared to dry oxygen alone which decrease in its magnitude as temperature increases. This is likely due to the adsorption phenomena of water and is encapsulated in the negative effective activation for the water-accelerated photooxidation pathway that accounts for the changes in adsorption equilibrium

constant at different temperatures. We hypothesize that the water-accelerated photooxidation pathway takes the following form:

$$h\nu \rightleftharpoons e^- + h^+ \quad \text{1 WPO}$$
$$O_2 + [*] \rightleftharpoons O_2^* \quad \text{2 WPO}$$
$$O_2^* + e^- \rightleftharpoons O_2^{\cdot -*} \quad \text{3 WPO}$$
$$H_2O + [*] \rightleftharpoons H_2O^* \quad \text{4 WPO}$$
$$\mathbf{H_2O^* + O_2^{\cdot -*} \rightleftharpoons OH^- + HO_2^{\cdot *}} \quad \textbf{5 WPO}$$
$$FA_{0.8}Cs_{0.2}Pb(I_{0.83}Br_{0.17})_3 + OH^- \rightarrow \text{Degradation Products} \quad \text{6 WPO}$$

Now going ahead with the derivation:

$$r_{FAPbI} = -r_7$$
$$r_{O_2^*} = 0 = r_2 - r_{-2} - r_3 + r_{-3}$$
$$r_{O_2^{\cdot -*}} = 0 = r_3 - r_{-3} - r_5 + r_{-5}$$
$$r_{HO_2^{\cdot *}} = 0 = r_5 - r_{-5} - r_6$$
$$r_{H_2O^*} = 0 = r_4 - r_{-4} - r_5 + r_{-5}$$
$$r_{HO^{-*}} = 0 = r_5 - r_{-5} - r_7$$

Solving for r_{FAPbI}:

$$r_{FAPbI} = -k_7[HO^{-*}]a_{FAPbI}$$
$$r_5 = r_6 + r_{r-5}$$

Here we note that $r_{-5} << r_6 \approx r_5$ for our rate determining step assumption to remain logically consistent:

$$r_5 \approx r_6$$

And we continue noting that against step 5 is RDS and therefore quite slow:

$$r_3 = r_{-3}$$
$$r_2 = r_{-2}$$
$$r_4 = r_{-4}$$
$$r_5 = r_6$$

Noting that reactive oxygen species will react quickly with the perovskite:

$$r_5 = r_7$$

Noting that the rate of loss of perovskite is equal to the rate limiting step:

$$r_{FAPbI} = -k_5[H_2O^*][O_2^{\cdot -*}]$$

Solving for $[H_2O^*]$ while assuming that we are in equilibrium (i.e., step 4 forward and reverse are fast kinetics):

$$r_4 = r_{-4}$$
$$k_4 P_{H_2O}[*] = k_{-4}[H_2O^*]$$
$$[H_2O^*] = K_{eq,4} P_{H_2O}[*]$$

And now solving for $[O_2^{\cdot -*}]$:

$$r_3 = r_{-3}$$
$$k_3[O_2^*]n = k_{-3}[O_2^{\cdot -*}]$$

$$[O_2^{\cdot -*}] = K_{eq,3} n [O_2^*]$$
$$r_2 = r_{-2}$$
$$k_2 P_{O_2} [*] = k_{-2} [O_2^*]$$
$$[O_2^*] = K_{eq,2} P_{O_2} [*]$$
$$[O_2^{\cdot -*}] = K_{eq,2} K_{eq,3} P_{O_2} n [*]$$

Which gives for r_{FAPbI}:

$$r_{FAPbI} = -k_5 K_{eq,4} P_{H_2O} [*] K_{eq,2} K_{eq,3} P_{O_2} n [*]$$
$$= -k_5 K_{eq,2} K_{eq,3} K_{eq,4} P_{O_2} P_{H_2O} n [*] 2$$

Now we need to solve a site balance for $[*]$:

$$[*]_T = [*] + [O_2^*] + [O_2^{\cdot -*}] + [HO_2^{\bullet *}] + [H_2O^*]$$

Site balance continued and ignoring the small contribution of $[HO_2^{\bullet *}]$:

$$[*]_T = [*]\left(1 + K_{eq,2} P_{O_2} + K_{eq,2} K_{eq,3} P_{O_2} n + K_{eq,4} P_{H_2O}\right)$$
$$[*] = \frac{[*]_T}{\left(1 + K_{eq,2} P_{O_2} + K_{eq,2} K_{eq,3} P_{O_2} n + K_{eq,4} P_{H_2O}\right)}$$

Plugging this back into our equation for r_{FAPbI}:

$$r_{FAPbI} = -k_5 K_{eq,2} K_{eq,3} K_{eq,4} P_{O_2} P_{H_2O} n [*] 2$$
$$r_{FAPbI} = -k_5 K_{eq,2} K_{eq,3} K_{eq,4} P_{O_2} P_{H_2O} n \frac{[*]_T^2}{\left(1 + K_{eq,2} P_{O_2} + K_{eq,2} K_{eq,3} P_{O_2} n + K_{eq,4} P_{H_2O}\right) 2}$$

Here, we assume that $K_{eq,4} P_{H_2O} << (1 + K_{eq,2} P_{O_2} + K_{eq,2} K_{eq,3} P_{O_2} n)$ and thus water is in the quasi-linear regime of the Langmuir isotherm:

$$r_{FAPbI} = -k_5 K_{eq,2} K_{eq,3} K_{eq,4} P_{O_2} P_{H_2O} n \frac{[*]_T^2}{\left(1 + K_{eq,2} P_{O_2} (1 + K_{eq,3} P_{O_2} n)\right) 2}$$
$$r_{WPO} = \frac{k_{WPO} P_{O_2} P_{H_2O} n}{\left(1 + K_{eq,2} P_{O_2} (1 + K_{eq,3} P_{O_2} n)\right) 2}$$

Excluding the effects of hydrate formation on adsorption site 'poisoning' at present, we can write the final form of the WPO reaction as the following:

$$r_{WPO} = \frac{k_{WPO} P_{O_2} P_{H_2O} n}{\left(1 + K_{eq,2} P_{O_2} (1 + K_{eq,3} P_{O_2} n)\right) 2}$$

SI section 8 below describes how this term will be modified to account for hydrate formation.

4.6.8 Derivation of Active Site Concentration Change Due to Hydrate Formation

In the case of humid environments, we observe that the net rate of perovskite loss increases at lower temperatures and decreases at higher temperatures compared to dry conditions. As such, we

hypothesize that water acts to increase the decomposition rate by providing a pathway with lower activation energy in which other ROSs decompose the perovskite. Section 7 of this supplement discusses this pathway and provides a derivation. Water may also react with the perovskite to form hydrate phases.[131] These have been observed to be reversible.[118,132,133] If the formation of hydrate phases negligibly affects the decomposition rate while consuming active adsorption sites, the coverage of a specific reactant or reactant precursor on the perovskite surface (e.g. oxygen, superoxide radical) would be lower compared to moisture free atmospheres. Thus, we hypothesize following: (1) water adsorbs less favorably as temperature increases[34,35], (2) hydrate formation increases with temperature, (3) only a specific fraction of adsorption sites can undergo hydrate formation, and (4) the adsorption and desorption reaction rate constants are large such that rapid site sampling is assumed. The implications of these hypotheses are the following: (1) surface adsorbed water (H_2O^*) predominates at lower temperatures while (2) hydrate bound water ($H_2O^* \cdot FA_{0.8}Cs_{0.2}Pb(I_{0.83}Br_{0.17})_3$) predominates at high temperatures (despite the fact that surface coverage is lower, see below for further explanation). An additional underlying assumption is that only surface adsorbed water can contribute to water-accelerated photooxidation reactions. Hydrate bound water is assumed to have consumed a surface adsorption site and not be able to react while bound in a hydrate (e.g. with superoxide radical). We begin with a derivation for hydrate formation equilibrium kinetics to account for the decrease in observed rates at high temperatures. The proposed reaction scheme is the following:

$$H_2O + [*]_{avail} \rightleftharpoons H_2O^* \qquad \text{1 HF}$$

$$H_2O^* + FA_{0.8}Cs_{0.2}Pb(I_{0.83}Br_{0.17})_3 \rightleftharpoons H_2O^* \cdot FA_{0.8}Cs_{0.2}Pb(I_{0.83}Br_{0.17})_3 \qquad \text{2HF}$$

To quantify the reduction in available active sites, we construct a parameter that asses the fraction of active sites still available (f_{active}):

$$f_{active} = 1 - \frac{[*]_{poisoned}}{[*]_{total}} = 1 - \frac{[\mathrm{H_2O^*} \cdot \mathrm{FA_{0.8}Cs_{0.2}Pb(I_{0.83}Br_{0.17})_3}]}{[*]_{total}}$$

Now, solving for $[\mathrm{H_2O^*} \cdot \mathrm{CHNH_2NH_3PbI_3}]$:

$$[\mathrm{H_2O^*} \cdot \mathrm{FA_{0.8}Cs_{0.2}Pb(I_{0.83}Br_{0.17})_3}] = K_{react} a_{FAPbI} [\mathrm{H_2O^*}]$$

$$= K_{react} a_{FAPbI} P_{H_2O} K_{ads} [*]_{avail}$$

where K_{react} is a temperature dependent equilibrium constant for hydrate formation (step 2HF) and K_{ads} is a temperature dependent equilibrium constant for water adsorption onto the perovskite surface (step 1HF). Note that $[*]_{avail}$ is the number of free adsorption sites available for water adsorption and hydrate formation. It is also available for oxygen adsorption, and thus, oxygen and superoxide radical are included in the site balance for these sites.

Doing a site balance on water only free adsorption sites, $[*]_{avail}$:

$$[*]_{avail,total} = [*]_{avail} + [\mathrm{H_2O^*}] + [\mathrm{H_2O^* \cdot FA_{0.8}Cs_{0.2}Pb(I_{0.83}Br_{0.17})_3}] + [\mathrm{O_2^*}] + [\mathrm{O_2^{\cdot -*}}]$$

$$= [*]_{avail}[1 + P_{H_2O} K_{ads} + K_{react} a_{FAPbI} P_{H_2O} K_{ads} + K_2 P_{O_2} + K_3 K_2 P_{O_2} n]$$

$$[*]_{avail} = \frac{[*]_{avail,total}}{1 + P_{H_2O} K_{ads} + K_{react} a_{FAPbI} P_{H_2O} K_{ads} + K_{eq,2} P_{O_2} + K_{eq,3} K_{eq,2} P_{O_2} n}$$

Where we assume that the concentration of adsorbed water is small relative to the other adsorbed species under all experimental conditions, ($P_{H_2O} K_{ads} \ll 1 + K_{react} a_{FAPbI} P_{H_2O} K_{ads} + K_2 P_{O_2} + K_3 K_2 P_{O_2} n$.

Thus, we arrive at the following:

$$= \frac{[*]_{avail,total}}{1 + K_{react} a_{FAPbI} P_{H_2O} K_{ads} + K_2 P_{O_2} (1 + K_3 n)}$$

Therefore, we can now calculate $[H_2O^* \cdot FA_{0.8}Cs_{0.2}Pb(I_{0.83}Br_{0.17})_3]$ by plugging in for $[*]_{avail}$:

$$[H_2O^* \cdot FA_{0.8}Cs_{0.2}Pb(I_{0.83}Br_{0.17})_3] = \frac{K_{react}a_{FAPbI}P_{H_2O}K_{ads}[*]_{avail,total}}{1 + K_{react}a_{FAPbI}P_{H_2O}K_{ads} + K_2P_{O_2}(1 + K_3n)}$$

We can note that the number of total available adsorption sites is a function of $[*]_{total}$:

$$[*]_{avail,total} = f_{water}\,[*]_{total}$$

Thus, plugging in for $[*]_{avail,total}$:

$$[H_2O^* \cdot FA_{0.8}Cs_{0.2}Pb(I_{0.83}Br_{0.17})_3] = \frac{f_{water}\,K_{react}a_{FAPbI}P_{H_2O}K_{ads}[*]_{total}}{1 + K_{react}a_{FAPbI}P_{H_2O}K_{ads} + K_2P_{O_2}(1 + K_3n)}$$

Now plugging back into the expression for f_{active}:

$$f_{active} = 1 - \frac{\frac{f_{water}\,K_{react}a_{FAPbI}P_{H_2O}K_{ads}[*]_{total}}{1 + K_{react}a_{FAPbI}P_{H_2O}K_{ads} + K_2P_{O_2}(1 + K_3n)}}{[*]_{total}}$$

Therefore, we arrive the final form for f_{active} where we can also define a net temperature dependent equilibrium constant for hydrate formation, $K_{hydrate} = a_{FAPbI}K_{react}K_{ads}$:

$$f_{active} = 1 - f_{water}\frac{K_{hydrate}P_{H_2O}}{1 + K_{hydrate}P_{H_2O} + K_2P_{O_2}(1 + K_3n)}$$

Note that, based on the results of our rate measurements, we expect $K_{hydrate}$ to be a function of temperature (likely obeying an Arrhenius relationship). Because $K_{hydrate} = K_{react}a_{FAPbI}P_{H_2O}K_{ads}$, the temperature

dependences of $K_{hydrate}$ will involve both that associated with water adsorption (K_{ads}) and the hydrate formation reaction (K_{react}). Based on a Van't Hoff analysis, we expect the function form of K_{react} to be the following:

$$K_{water}(T) = K_{0,hydrate} \exp \frac{-\Delta H_{hydrate}^{eff}}{k_B T}$$

where the effective enthalpy of the hydrate formatted reaction is the sum of the enthalpy of the hydrate formation reaction (2HF) and the adsorption enthalpy of water on the perovskite surface (1HF): $\Delta H_{hydrate}^{eff} = \Delta H_{react} + \Delta H_{ads}$. Here, we expect ΔH_{ads} to be negative and ΔH_{react} to be positive. The temperature independent prefactor, $K_{0,hydrate}$, will include the entropic contributions of the two equilibrium constants as well as the activity of the perovskite.

The functional form of this reaction shows that, as P_{H_2O} increases, the active fraction of adsorption sites on the perovskite surface will asymptote to 1-f_{water} which is equal to the number of sites not susceptible to water adsorption and subsequent hydrate reaction. As discussed in the main text, to determine the various parameters associated with the above equation, we fit the rate at 85°C, 1 sun, 21% O_2 over a range of water vapor partial pressures (Figure 4.4c). Here, we perform the fit under the assumption that the dry-photooxidation superoxide radical decomposition reactions dominate the rate. Thus, the rate of 'dry' photooxidation (that is photooxidation due to superoxide radical related decomposition) in humid environments becomes the following:

$$r_{DPO,water} = f_{active} \frac{k_{DPO}(T) P_{O_2} n}{1 + K_{eq,2} P_{O_2} (1 + K_{eq,3} n)}$$
$$= \frac{k_{DPO}(T) P_{O_2} n}{1 + K_{eq,2} P_{O_2} (1 + K_{eq,3} n)} \left(1 - f_{hydrate} \frac{K_{hydrate}(T) P_{H_2O}}{1 + K_{hydrate}(T) P_{H_2O}}\right)$$

Similarly, we must adjust the water-accelerated photooxidation reaction to account for the hydrate formation.

$$r_{WPO,water} = f_{active}\frac{k_{WPO}P_{O_2}P_{H_2O}n}{\left(1+K_{eq,2}P_{O_2}\left(1+K_{eq,3}P_{O_2}n\right)\right)2}$$

$$= \frac{k_{WPO}P_{O_2}P_{H_2O}n}{\left(1+K_2P_{O_2}\left(1+K_3P_{O_2}n\right)\right)2}\left(1-f_{water}\frac{K_{hydrate}(T)P_{H_2O}}{1+\ K_{hydrate}(T)P_{H_2O}\ +\ K_2P_{O_2}(1+K_3n)}\right)$$

Therefore, the total photooxidation reaction, which can be written as the sum of the dry and water-accelerated photooxidation pathways, is the following:

$$r_{total} = \left(1-f_{water}\frac{K_{hydrate}(T)P_{H_2O}}{1+\ K_{hydrate}(T)P_{H_2O}+\ K_2P_{O_2}(1+K_3n)}\right) \times\left[\frac{k_{WPO}P_{O_2}P_{H_2O}n}{\left(1+K_2P_{O_2}\left(1+K_3P_{O_2}n\right)\right)2}+\frac{k_{DPO}P_{O_2}n}{1+K_2P_{O_2}(1+K_3n)}\right]$$

4.6.9 Model Fitting and Bootstrapping for Water-Accelerated Photooxidation and Hydrate Formation

To initially assess the parameter landscape for the remaining fit parameters, we performed rigorous grid search optimizations on various subsections of the humid dataset. For each fit, k_{WPO} is allowed to vary while $E_{A,WPO}^{eff}$ and $\Delta H_{hydrate}^{eff}$ are fixed. The result of these searches are shown below in Figure 4.11a-d. Also included are Arrhenius plots that allow for qualitative comparison between the optimized model with fitted parameters and the data (Figure 4.11e-f). We observe that 3 of the 4 subsets provide good fits the entire humid dataset. The subset of the dataset that includes only runs between 55-85°C provides an obviously poor fit (Figure 4.11h). We observe that the optimized parameters from this dataset are not optimized for fitting of the low temperature data in which water accelerated photooxidation plays an important role in the overall rate.

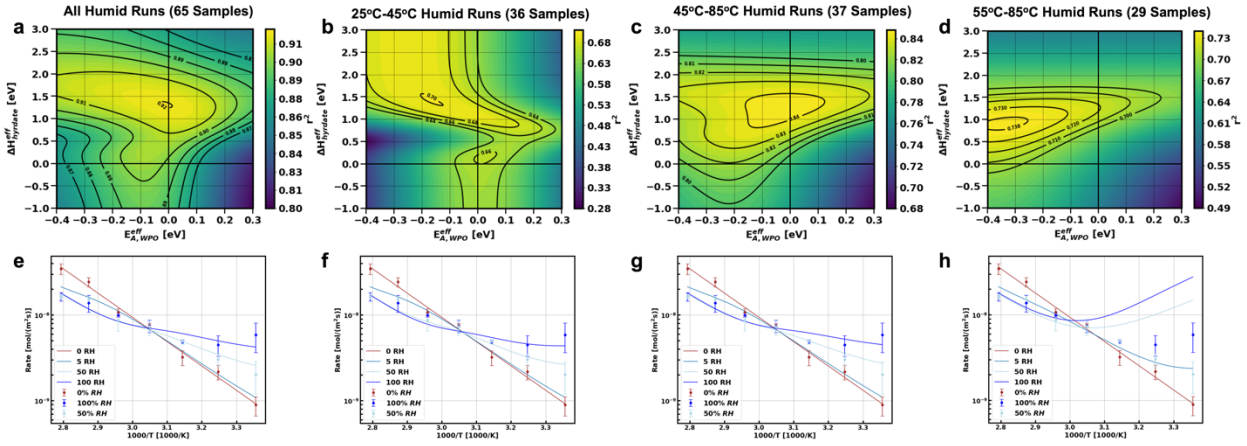

Figure 4.11. **Grid parameter search optimization for subsections of the humid dataset.** (a-d) Contour plots for the grid search optimization with coefficient of determination plotted for (a) the full humid dataset, (b) humid runs between 25-45°C, (c) humid runs between 45-85°C, and (d) humid runs between 55-85°C. (e-f) Arrhenius plots of the measured rates (points with error bars) and the model fit lines for the optimized parameters corresponding the each of the subsets. Table S2 provides a list of each of these values.

Note that the grid search optimization is necessary due to the non-linearity of $E^{eff}_{A,WPO}$ and $\Delta H^{eff}_{hydrate}$ which make simultaneous fitting challenging. Based on these results, we choose to perform a bootstrap analysis of each of the parameters for specific parts of the dataset. Importantly, the 25-45°C appears to be the most sensitive to the $E^{eff}_{A,WPO}$ since WPO is important to the overall rate at these temperatures and substantially less so at higher temperatures.

Table 4-4. **Optimized Parameter Values for the WPO Grid Search Optimization**

	All Humid	**25-45°C**	**45-85°C**	**55-85°C**
$\Delta H^{eff}_{hydrate}$	1.316	1.416	1.276	0.905
$E^{eff}_{A,WPO}$	-0.011	-0.165	-0.016	-0.339
k_{WPO}	8.36×10^{-26}	2.14×10^{-28}	7.43×10^{-26}	2.07×10^{-30}

r^2_{subset}	0.920	0.700	0.8440	0.740
$r^2_{all\ humid}$	0.920	0.917	0.920	-0.700

To determine the optimal parameter value and estimate the uncertainty of the parameter fits for water accelerated photooxidation and hydrate formation, we perform a bootstrapping procedure on specific temperature range subsets of the humid dataset. The general bootstrapping procedure involves generating 10,000 datasets, each of which is created by sampling with replacement from a specific subset of the humid dataset until the subset size is matched. From each of the subsets, the desired fitting parameters that define the complete decomposition reaction equation are fit using curve_fit from the scipy package in python. The results of these procedures are shown below as histograms and are used to determine the uncertainty associated with the fits. The fitting parameters are the activation energies associated with water accelerated photooxidation, the effective enthalpy of hydrate formation, and the temperature independent prefactor for the WPO reaction. The results of these bootstraps are shown below and the final optimized parameters with uncertainties are included in Table 1 in the main text. An explanation of the fitting procedure is included in table S3 below. In short, low temperature data (25-45ºC) is used to fit $E^{eff}_{A,WPO}$ while the complete humid data is used to fit $\Delta H^{eff}_{hydrate}$. Based on the range of $\Delta H^{eff}_{hydrate}$ values observed for the grid search optimization, we expect hydrate formation to play a negligible role at lower temperature. This fact is demonstrated in Figure 4.13 where we use the lowest $\Delta H^{eff}_{hydrate}$ value observed (corresponding to highest influence at lower temperatures) during the grid search procedure to model the hydrate formation poisoning factor. The hydrate formation poisoning factor is near unity across all water partial pressures below 45ºC.

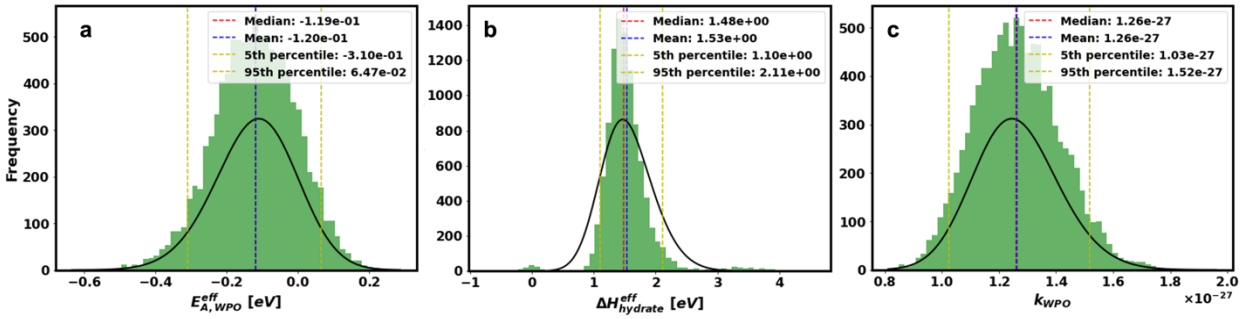

Figure 4.12. **Bootstrapping Procedure for Water-Accelerated Photooxidation and Hydrate Formation Parameters.** Histogram results of bootstrapping procedure over 10,000 iterations for (a) $E^{eff}_{A,WPO}$, (b) $\Delta H^{eff}_{hydrate}$, and (c) $k_{0,WPO}$. Mean, median, 5th percentile, and 95th percentile of the bootstrap fits is included. Black traces over the histograms are skewed gaussians fit to the data (arbitrarily scaled).

Table 4-5. **Explanation of Fitting Procedure for Water-Accelerated Photooxidation and Hydrate Formation Parameters**

Parameter	Subset of the data used for fitting
$\boldsymbol{E^{eff}_{A,WPO}}$	Runs in oxygen containing environments (3 kPa to 101 kPa) with varying illumination (0.1 to 1.86 suns) and humidity (0.1 to 2.3 kPa) with set $\Delta H^{eff}_{hydrate}$ and the following temperature range: 25-45°C
$\boldsymbol{k_{0,WPO}}$	Runs in oxygen containing environments (3 kPa to 101 kPa) with varying illumination (0.1 to 1.86 suns) and humidity (0.1 to 2.3 kPa) with set $E^{eff}_{A,WPO}$ and $\Delta H^{eff}_{hydrate}$ over all temperatures
$\boldsymbol{\Delta H^{eff}_{hydrate}}$	Runs in oxygen containing environments (3 kPa to 101 kPa) with varying illumination (0.1 to 1.86 suns) and humidity (0.1 to 2.3 kPa) with set $E^{eff}_{A,WPO}$ over all temperatures
$\boldsymbol{f_{water}}$	Runs in humid (0 to 2.3 kPa water vapor partial pressure) air at 85°C
$\boldsymbol{k_{water,0}}$	Runs in humid (0 to 2.3 kPa water vapor partial pressure) air at 85°C

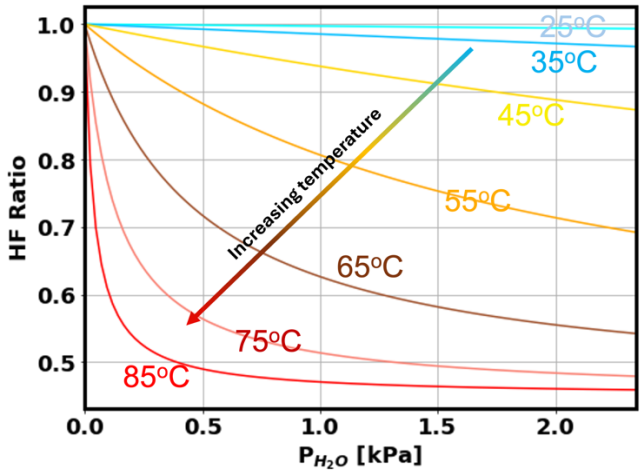

Figure 4.13. **Hydrate formation factor versus partial pressure of water over a range of temperatures for $\Delta H^{eff}_{hydrate}$ equal to 1.3 eV.** Here, the effective enthalpy of hydrate formation is chosen based on the preliminary grid searches that gave optimized fits around 1.3 eV for the three good fits. Note that the optimized value (based on r^2 for the humid dataset) is 1.48 eV (Figure 4.12b).

4.6.10 Model Results for Full Dataset

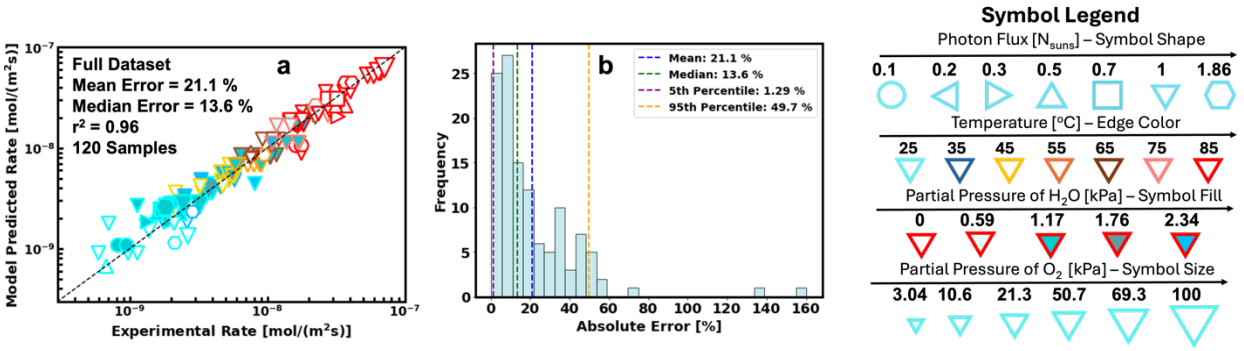

Figure 4.14. **Statistics for fitting the complete dataset.** (a) Parity plot for the full dataset that includes both dry and humid runs (120 samples total). (b) Histogram of absolute percentage errors for the full dataset. Mean, median, 5th percentile, and 95th percentile of the errors is included. Symbol legend is for the parity plot (a).

4.6.11 Ex-situ Photooxidation of $FA_{0.8}Cs_{0.2}Pb(I_{0.9}Br_{0.1})_3$ and $FA_{0.8}Cs_{0.2}PbI_3$

To see how films of varying composition behave under combined stresses of oxygen, water, and illumination, we fabricated $FA_{0.8}Cs_{0.2}Pb(I_{0.9}Br_{0.1})_3$ and $FA_{0.8}Cs_{0.2}PbI_3$ perovskite thin films (via

same methods as for the $FA_{0.8}Cs_{0.2}Pb(I_{0.83}Br_{0.17})_3$ films) and monitored their degradation with *ex situ* UV-vis absorbance. The results of 4 total degradation experiments per composition are shown in Figure 4.15 below. Note that these experiments were carried out under identical conditions to those discussed in SI section 4.6.4 and shown in Figure 4.9. We observe that these films display the same behavior as the $FA_{0.8}Cs_{0.2}Pb(I_{0.83}Br_{0.17})_3$ films discussed in the main text. At elevated temperatures (85ºC), the net effect of adding water to dry air is a decrease in the photooxidation rate while, at lower temperatures (25ºC), the net effect is an increase in the photooxidation rate.

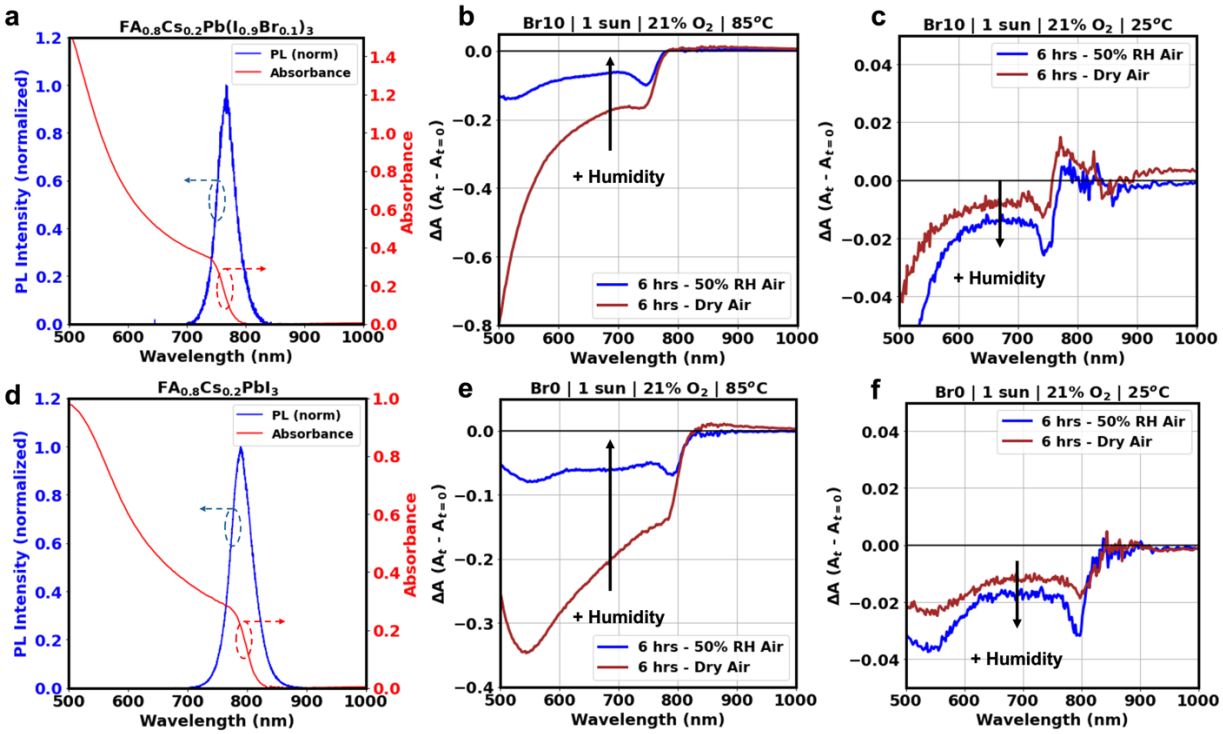

Figure 4.15. **Ex-situ UV-vis Absorbance During Photooxidation of Varying Compositions.** (a, d) UV-vis absorbance and normalized film PL intensity (PL collected from films illuminated with 1.5 x 10^{21} photons/m^2/s from a 532 nm CW laser, refer to prior work for full PL collection details[36]) for fresh (a) $FA_{0.8}Cs_{0.2}Pb(I_{0.9}Br_{0.1})_3$ and (d) $FA_{0.8}Cs_{0.2}PbI_3$ perovskite thin films. Absorbance measurements of (b, c) $FA_{0.8}Cs_{0.2}Pb(I_{0.9}Br_{0.1})_3$ and (e, f) $FA_{0.8}Cs_{0.2}PbI_3$ thin films degraded in air at (b, e) 85ºC and at (c, f) 25ºC over a period of 6 hours with (blue traces, 50% RH) and without moisture (brown traces).

5 Bromine Alloying Dictates the Stability Tradeoff Between Light and I_2 Vapor Induced Degradation Pathways in Mixed Halide Lead Perovskites

The work presented in this chapter is currently unpublished. This work is partially an extension of the work presented in chapter 3 but also includes new experimental procedures in which perovskite thin films are exposed to I_2 vapor, a known byproduct of various halide perovskite decomposition reactions.

5.1 Abstract

Hybrid metal halide perovskite semiconductors are promising for next-generation, low-cost optoelectronics, but their instability under operating and ambient conditions remains a central challenge. Here, we examine the stability of $FA_{0.8}Cs_{0.2}Pb(I_{1-x}Br_x)_3$ thin films (x = 0, 0.1, 0.17). Using sub-bandgap absorption spectroscopy under illumination in inert environments, we track the formation kinetics of reduced lead species and find that increasing bromine content enhances near-infrared absorption across a range of temperatures, indicating increased susceptibility to reduced lead defect formation and reduced photostability. Complementary time-series measurements of carrier diffusion length under photo-stress show a monotonic decrease in characteristic decay times with increasing bromine fraction, establishing a correlation between composition, diffusion length decay, and the formation rate of reduced lead species. Given that iodine vapor is generated during light-induced decomposition and can accumulate in encapsulated devices, we next investigated the impact of I_2 exposure to determine whether bromine incorporation alters resistance to this secondary degradation pathway, which may act in parallel during photostress in encapsulated perovskite solar cells. Optical analyses (photoluminescence and absorption) reveal progressive redshifts in PL emission and absorption onset during I_2 exposure, motivating the use of X-ray diffraction to more directly track structural degradation. We find that

bromine incorporation improves resistance to I_2-induced degradation, slowing perovskite transformation to non-perovskite delta phases. We propose that these contrasting stability trends arise from defect energy level alignment, where bromide-rich compositions favor halide oxidation due to their wider bandgaps, and from the stabilizing chemistry of mixed halides, in which I_2Br^- formation helps suppress phase transformations. These results highlight a key trade-off: bromine reduces intrinsic photostability but enhances stability against photogenerated iodine vapor.

5.2 Introduction

Lead halide perovskite semiconductors ($APbX_3$) are promising absorber and emitter materials for next-generation solar cells and light-emitting diodes.[134] Their tunable optoelectronic properties, defect tolerance, high radiative efficiencies,[135] and compatibility with both solution and vapor processing[136] make them attractive for rapid commercial scale-up. However, their widespread deployment ultimately hinges on understanding and controlling the chemical decomposition pathways and phase transformations that limit the operational stability of optoelectronic devices they comprise.

Perovskite solar cells in particular have attracted significant attention over the past decade for their rapid efficiency gains, reaching ~27% for single-junction devices and ~35% for perovskite–silicon tandems. Bandgap optimization and empirical performance studies have converged on compositions alloyed with predominately formamidinium and cesium at the A-site, paired with nearly pure iodide at the X-site for single-junction devices, and mixed iodide-bromide alloys at the X-site for use as the top-cell absorber in tandems.[24] Given the established infrastructure of silicon photovoltaics, much of the commercial effort has focused on developing perovskite–silicon tandem cells. Regardless, across all device architecture, long-term stability of the perovskite absorber remains the critical factor governing commercial viability.

Compositional tuning is a central strategy for tailoring the properties and stability of metal halide perovskites. The earliest photovoltaic demonstrations employed methylammonium lead triiodide ($MAPbI_3$) and tribromide ($MAPbBr_3$) as absorbers in dye-sensitized solar cells.[137] Within only a few years, however, formamidinium-rich perovskite compositions emerged as leading candidates for higher-efficiency and more stable PSCs.[98,138–140] These improvements are attributed to the enhanced thermal stability and stronger hydrogen bonding interactions of the formamidinium cation compared to the archetypal methylammonium.

While bromine alloying at the X-site unlocks higher bandgap compositions suitable for multijunction PSCs, empirical studies show that bromine fractions above ~0.2 suffer from light-induced halide phase segregation and generally exhibit lower optoelectronic quality than less aggressively alloyed compositions.[70,99,100,141] Some studies suggest that higher bromine contents can be stabilized through A-site tuning, for example with large cesium fractions[142] or with bulky cations that induce favorable strain and suppress halide phase segregation.[143,144] Despite these promising strategies, long term device operation has yet to be demonstrated. Moreover, bandgaps exceeding ~1.7 eV are unnecessary for current matching in two or four terminal tandem devices, further constraining the practical design space for halide perovskites to <20% bromide at the X-site.[145]

The role of bromide in perovskite material stability remains debated, with several studies reporting seemingly conflicting results. On one hand, bromine incorporation has been shown to improve photovoltaic performance.[50] Prior studies have identified that adding bromine to pure iodide perovskites reduces non-radiative recombination, posited to be via reduction in hole trapping[146] or optimizing the orientation of the formamidinium A-site cation.[147,148] Furlan et al. further reported that increasing bromide halide fraction (up to ~15%) in methylammonium based

perovskite devices yielded better performing devices with improved morphology and crystallinity.[149] More broadly, many earlier studies highlight that bromine can enhance device performance by slowing crystallization kinetics, which yields larger grains with fewer trap states.[150] However, such enhancements in initial optoelectronic quality and photovoltaic performance largely represent instantaneous snapshots, providing limiting insight into long-term operational stability and overlooking how bromine incorporation may also influence defect energetics and halide oxidation chemistry.

Beyond improved crystallization and trap reduction, the long-term chemical, electronic, and structural consequences of bromine incorporation remain less clear. Iqbal et. al[86] reported that, even in films of similar apparent morphology, higher bromine concentrations led to reduced photostability, correlated with diminishing octahedral tilting and a greater amount of non-perovskite polytype inclusions, features previously identified as degradation seeds in perovskite thin films[59,60] and devices.[63] Studies by Hidalgo et al.[151] and LaFollette et al.[152] demonstrated that bromine incorporation suppresses low temperature phase transformations and alters the phase transitions and thermal stability at elevated temperatures, respectively.

Alignment of the perovskite valence band with iodide defect levels is thought to critically influence the favorability of iodine oxidation and subsequent halide loss.[69] Accordingly, increasing bromine concentrations can, somewhat counterintuitively, exacerbate mass loss and photoinstability due to preferential halide oxidation.[153] Together, these findings suggest that bromine incorporation may render perovskite films more susceptible to light-induced degradation under inert conditions, the ultimate performance-limiting case of metal halide perovskites under strong encapsulation, underscoring a central uncertainty: while bromine can improve morphology

and initial performance, its impact on intrinsic photostability and iodine-driven degradation remains unresolved.

In this study, we investigate the stability of $FA_{0.8}Cs_{0.2}Pb(I_{1-x}Br_x)_3$ (x = 0, 0.1, 0.17) series of perovskite thin films ($FA_{0.8}Cs_{0.2}Pb(I_{1-x}Br_x)_3$, x = 0, 0.1, 0.17) under light and heat stress as well as controlled iodine vapor exposure, in order to clarify the impact of bromine incorporation on long-term stability. Under photo stress, higher bromine fractions accelerate the formation of reduced lead defects, a trend corroborated by in situ two-point photoconductivity measurements in which higher bromine films see faster declines in measured ambipolar diffusion length. Because I_2 is a key decomposition product of light-induced halide oxidation, we further examined the response of these films to I_2 vapor. While all compositions degrade under exposure, we find the opposite trend: bromine-rich films exhibit greater resistance to I_2-induced degradation.

5.3 Photostability of $FA_{0.8}Cs_{0.2}Pb(I_{1-x}Br_x)_3$ Films

The perovskite thin films studied here were fabricated by spin-coating on glass substrates, with full details provided in the Supporting Information. Baseline characterization by UV-Vis absorption, steady-state photoluminescence (PL), x-ray diffraction (XRD), and scanning electron microscopy (SEM) confirmed the formation of a single perovskite crystalline phase with comparable apparent grain sizes across compositions (SI Figure 5.5). As expected, the optical bandgap increased with higher bromine content (SI Figure 5.5b), accompanied by diffraction peak shifts to higher angles (SI Figure 5.5a) consistent with bromine incorporation into the lattice.

To confirm that halide phase segregation does not occur in the films of interest, we performed steady-state PL measurements under continuous excitation with a 532 nm CW laser in an N_2 filled microscope stage. The normalized emission spectra were nearly identical across compositions over a 60-minute period of continuous illumination (SI Figure 5.6), indicating that

the materials do not exhibit halide segregation under illumination. Having established that the films are phase-pure, morphologically comparable, and free from halide segregation that may otherwise complicate stability results, we next examined their photostability across the compositional range.

To assess photostability, the films were exposed to illumination from a broad-spectrum LED (400–700 nm emission) inside a nitrogen-filled glovebox while maintained on a hotplate. Spectral absorbance was periodically measured during exposure using a UV-vis spectrometer. The LED flux was calibrated to correspond to one-sun absorbed photon flux, using the short-circuit current density of a reference device fabricated from the x = 0.17 composition. Because the x = 0.1 and x = 0 films have lower bandgaps, their absorbed flux is expected to be slightly higher (estimated <5%); however, this small variation does not affect the compositional comparisons reported here.

Figure 5.1a-c displays absorbance spectra of the $FA_{0.8}Cs_{0.2}Pb(I_{1-x}Br_x)_3$ thin films over the course of photo stress from a white LED at 35°C. Note that absorbance is calculated from separate measurements of sample percent transmittance and reflectance and thus accurately quantifies the film 'internal absorbance' which is linearly proportional to light absorbing material in the beam path. Across all compositions, a steady increase in near-infrared sub-bandgap absorption is observed over the course of photostress. We have previously attributed this sub-bandgap feature to the formation of reduced lead species (likely metallic Pb^0) generated during light-induced decomposition.[36] Thus, assuming that the sub bandgap absorption is due to the presence of reduced lead defects, the rate at which the sub bandgap absorption increases can be used to quantify the rate. This approach enables quantitative comparison of the susceptibility to defect generation across the three compositions.

Figure 5.1d shows the time evolution of absorbance at 1000 nm, chosen as an optimal probe for Pb^0 detection because it lies well below the bandgap of all compositions yet remains within an energy range where Pb^0 exhibits appreciable absorption. Linear fits to the absorbance increase reveal a clear compositional trend: x = 0.17 generates reduced lead defects most rapidly, followed by x = 0.1, with x = 0 showing the slowest rate of defect formation. Given the detrimental impact of Pb^0 on carrier transport and overall optoelectronic performance,[36,55,68,154,155] these results provide direct evidence that bromine incorporation accelerates light-induced degradation in inert environments.

In addition to measurements at 35°C, absorbance was also tracked for samples held at 55°C and 85°C (SI Figure 5.7 and 5.8). Linear fits, as shown in Figure 5.1d for the samples stressed at 35°C, were performed for each composition at all 3 temperatures to extract comparative defect formation rates. These rates are summarized in Arrhenius plots separated by composition (Figure 5.1e) and also listed in SI Table 5-1.. The temperature dependence is well described by Arrhenius behavior, with activation energies ranging from 0.3 to 0.6 eV. Importantly, across the entire temperature range examined, spanning the generally accepted daytime operating conditions of fielded perovskite modules,[156] the x = 0.17 films consistently exhibit the fastest rate of reduced-lead defect formation, followed by x = 0.1 and x = 0.

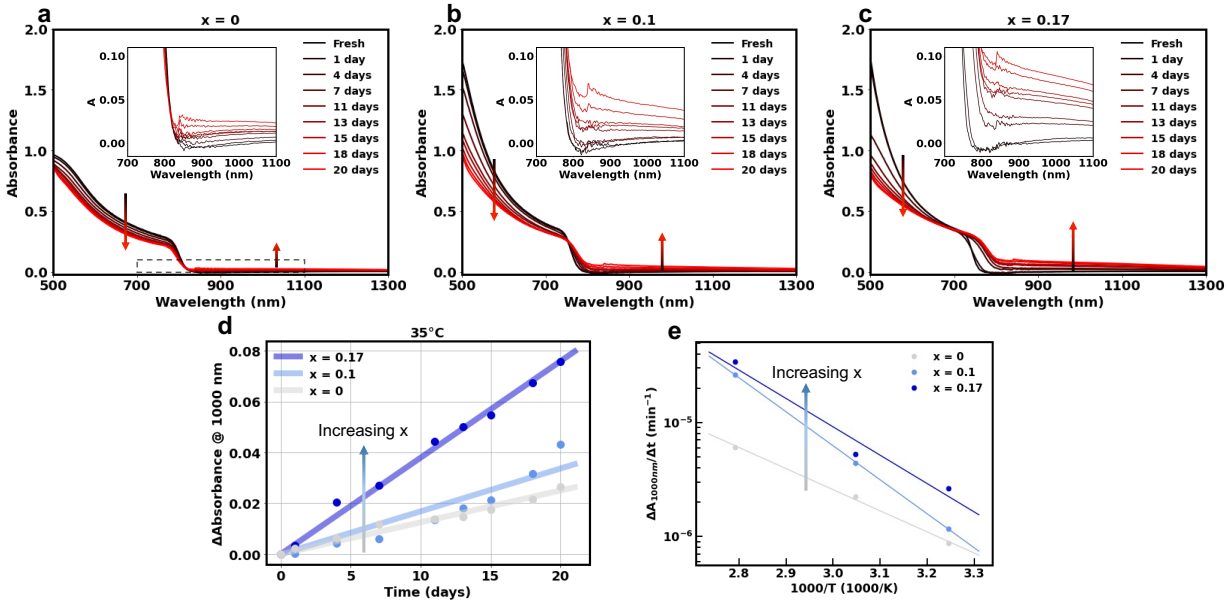

Figure 5.1. **Absorption changes during photo stress of $FA_{0.8}Cs_{0.2}Pb(I_xBr_{1-x})_3$ Thin Films.** UV-vis absorbance spectra of (a) $FA_{0.8}Cs_{0.2}PbI_3$, (b) $FA_{0.8}Cs_{0.2}Pb(I_{0.9}Br_{0.1})_3$, and (c) $FA_{0.8}Cs_{0.2}Pb(I_{0.83}Br_{0.17})_3$ during photo stress (1 sun, broad spectrum white LED) at 35°C in a N2 glovebox over the course of 20 days. (d) Change in 1000 nm absorbance over the course of 20 days for each of the film compositions with linear fits. (e) Arrhenius plot for measured rate of sub bandgap absorption at 1000 nm.

To directly probe the degradation of charge transport properties, we performed *in situ* measurements of ambipolar diffusion length (L_D) using a two-point photoconductivity method, described in detail in our prior reports.[36,82,83,144] In short, gold contacts were deposited on the sample with a channel width of 0.01 cm. The films were placed in a microscope stage fitted with electrical wiring and gas ports used for continuous nitrogen purging. Films were subject to continuous illumination from a calibrated 540 nm monochromatic LED source fed through an upright microscope with photoconductivity measurements taken every 5 minutes.

This approach is particularly valuable because L_D captures the combined effects of carrier lifetime and carrier mobility. The diffusion length was calculated using the relationship previously derived by Stoddard et al.: $L_D = \sqrt{\frac{\sigma_{ph} kT}{2q^2 G}}$, where σ_{ph} is the measured photoconductivity, kT is

Boltzmann's constant multiplied by temperature, q is the charge on the electron, and G is the photogeneration rate.[33] Time-series measurements were collected during continuous illumination at multiple temperatures for each composition (Figure 5.2a–c). To quantify degradation kinetics, we extracted the characteristic rate of L_D decline by taking the reciprocal of the time required for L_D to decrease to 80% of its maximum value (T80-L_D). This procedure enables direct comparison of photostability across bromide fractions, analogous to the analysis of sub-bandgap absorbance.

Figure 5.2a-c shows normalized timeseries measurements (referred to as runs) for $FA_{0.8}Cs_{0.2}Pb(I_xBr_{1-x})_3$ films during degradation under one-sun equivalent photon flux (calibrated to the x = 0.17 composition) at several temperatures. In several runs, an initial increase in L_D is observed at early times, after which the diffusion length declines nearly monotonically. Consistent with the sub-bandgap absorption results in Figure 5.1, the x = 0.17 films exhibit the fastest L_D decay at all temperatures, followed by x = 0.1 and then x = 0, indicating reduced photostability with increasing bromine content.

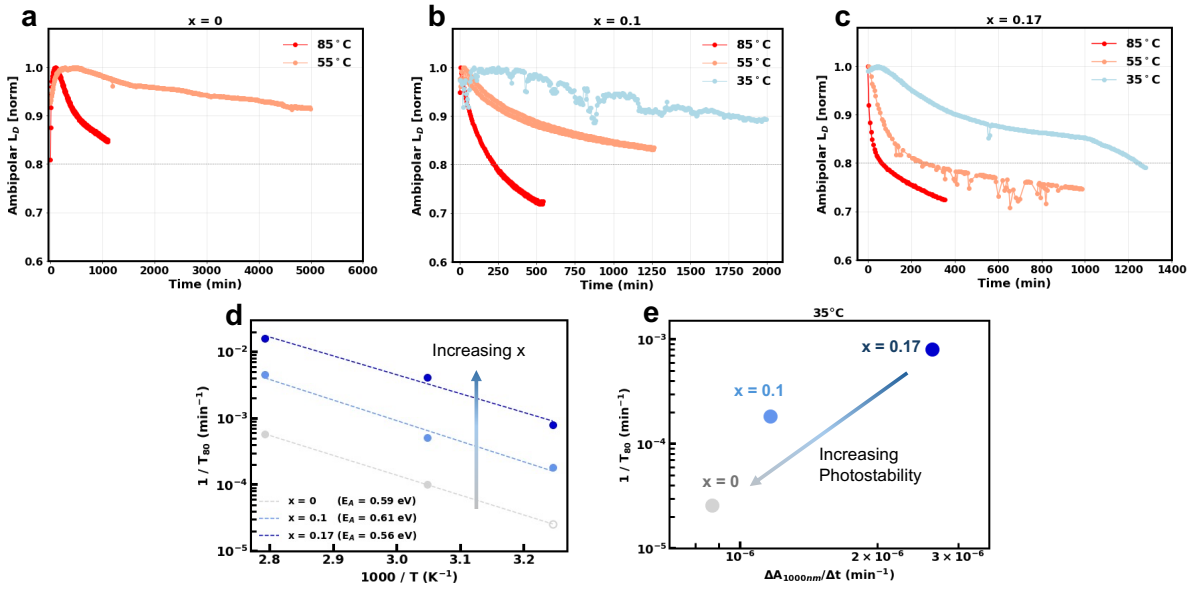

Figure 5.2. **Optoelectronic quality decline of $FA_{0.8}Cs_{0.2}Pb(I_xBr_{1-x})_3$ Thin Films during photo stress.** Normalized ambipolar diffusion length of (a) $FA_{0.8}Cs_{0.2}PbI_3$, (b) $FA_{0.8}Cs_{0.2}Pb(I_{0.9}Br_{0.1})_3$, and (c) $FA_{0.8}Cs_{0.2}Pb(I_{0.83}Br_{0.17})_3$ over time at various temperatures while stressed under 1.5 x 10^{21} photons/(m^2s) (540 nm green LED filtered light, ~55 mW/cm^2). (d) Arrhenius plot for the characteristic rate of ambipolar diffusion length decline (1 / T80). Note that the 35°C run was not collected due to its expected length (~27 days) but instead was approximated (indicated by an open circle) based on Arrhenius relationship. (e) Characteristic rate of diffusion length decline versus rate of 1000 nm absorbance increases for the three compositions at 35°C, establishing a causal link between reduced lead defect formation, material composition, and optoelectronic quality decline. Runs that did not reach T80-LD were extrapolated based on a linear fit to the ~linear part of the curves.

Figure 5.2d summarizes the extracted L_D decline rates for all runs in an Arrhenius plot. Fits to the data yield a consistent activation energy of ~0.6 eV across compositions. This value lies within the range typically associated with ionic motion in metal halide perovskites and matches the activation energy we previously reported for reduced-lead defect formation in x = 0.17 films.[36] Notably, Jiang et. al also reported a similar ~0.6 eV barrier for efficiency decline (1/T80-PCE) in high-performance (>24% PCE) p-i-n single junction cells,[157] suggesting the possibility of similar rate limiting processes underlying both device performance decline and the transport degradation

observed here. Across all conditions, the trend remains clear: higher bromine fractions accelerate L_D decay.

Figure 5.2e compares the characteristic rate of L_D decline with the rate of 1000 nm sub-bandgap absorbance growth at 35°C across the three compositions. A strong, nearly linear correlation is observed, directly linking transport degradation with the formation of reduced-lead defects. Taken together, the results in Figures 5.1 and 5.2 establish an unambiguous correlation between bromine composition, defect generation, and optoelectronic property loss, underscoring the critical role of material composition in governing photostability. While these results demonstrate that bromine incorporation accelerates intrinsic photodegradation through enhanced reduced-lead defect formation, the impact of bromine on stability to I_2 vapor, a decomposition product of light-induced reactions that can accumulate and accelerate degradation even in well-encapsulated devices, remains unresolved.

5.4 Impact of I_2 Vapor Exposure on $FA_{0.8}Cs_{0.2}Pb(I_xBr_{1-x})_3$ Films

Because iodide-containing perovskites readily expel iodine under photoexcitation,[58,73,115,154,158,159] much research has focused on understanding their chemical stability in the presence of I_2 vapor. A broad consensus in the literature is that iodide ions are oxidized by photoexcited holes to form I_2, which can subsequently escape the film. This same process is also implicated in halide phase segregation phenomena.[72,153,159] Consequently, understanding how I_2 vapor interacts with halide perovskites is critical for developing a comprehensive picture of all the photochemical pathways that can occur over decades-long device operation. Several studies have further identified I_2 buildup as a direct cause of device failure. For example, Fu et al. performed an extensive root-cause analysis of FA-based PSCs under combined light and heat stress, concluding that I_2 generation during operation dramatically accelerates device

breakdown.[92] Similarly, Khadka et al. showed that I_2 formation in PSCs is strongly correlated with cell-level degradation.

At the film level, Wang et al. demonstrated that $MAPbI_3$ rapidly degrades to PbI_2 in the presence of I_2 vapor and further showed that FA-based perovskites, including $FA_{0.8}Cs_{0.2}PbI_3$, are also susceptible to I_2 induced decomposition.[93] Importantly, they found that increasing bromine concentrations in $MAPb(I_xBr_{1-x})_3$ improved resistance to chemical conversion to PbI_2 upon I_2 exposure. However, systematic studies of mixed-cation mixed-halide compositions spanning a range of bromine fractions remain lacking, preventing direct comparison of stability trends of this class of perovskites. Moreover, comprehensive investigations linking intrinsic photostability with I_2 vapor stability, mimicking the parallel degradation pathways expected in well-encapsulated solar cells, are not yet available. Here, we test the I_2 vapor stability of the films of interest by exposing them to controlled I_2 environments and monitoring the resulting optical and structural changes.

Figure 5.3 presents UV-vis absorption and steady-state PL measurements collected on separate films exposed to controlled ambient I_2 vapor for 0, 20, 40, 60, 90, and 120 minutes. Separate films were used at each time point to avoid artifacts from repeated ambient exposure, and all experiments were performed in a nitrogen-filled glovebox to isolate the effects of I_2 vapor alone (see SI for details). Figure 5.3a–c show the evolution of PL spectra during exposure (samples and solid I_2 held at 25°C), revealing a pronounced redshift with increasing time that is consistent with the formation of iodine-rich phases. For the mixed-halide compositions (x = 0.1, 0.17), this process resembles light-induced halide phase segregation.[159] Interestingly, even the pure-iodide perovskite exhibits substantial redshifts in both PL center of mass and peak wavelength (Figure 5.3d). This behavior may arise from (1) filling of iodide vacancies or (2) cation segregation and subsequent carrier funneling into lower-bandgap FA-rich domains. Notably, the PL center of mass shifts well

below the ~1.65 eV edge typically associated with halide phase segregation, suggesting significant iodine incorporation into the lattice beyond that which can be achieved with light stress alone.

Figure 5.3e-g show the absorbance spectra taken on the same films, along with optical bandgaps extracted by Tauc fitting. A pronounced redshift in the absorption onset is observed for all compositions, with the calculated bandgaps decreasing continuously over the course of exposure. This shift is consistent with the formation of lower-bandgap phases, either iodine-rich domains or segregated cation phases that dominate the absorption onset. Importantly, despite the redshift, the absorbance at higher photon energies (shorter wavelengths) decreases for all films. A simple bandgap reduction would instead be expected to increase absorption uniformly across the visible spectrum (~1.8–3.1 eV). The decrease in high-energy absorption therefore indicates concurrent chemical decomposition of the perovskite lattice. Together, optical results reveal two parallel processes under I_2 vapor exposure: (1) iodine intercalation into the lattice, producing redshifts in PL and bandgap, and (2) surface-driven chemical decomposition of the perovskite.

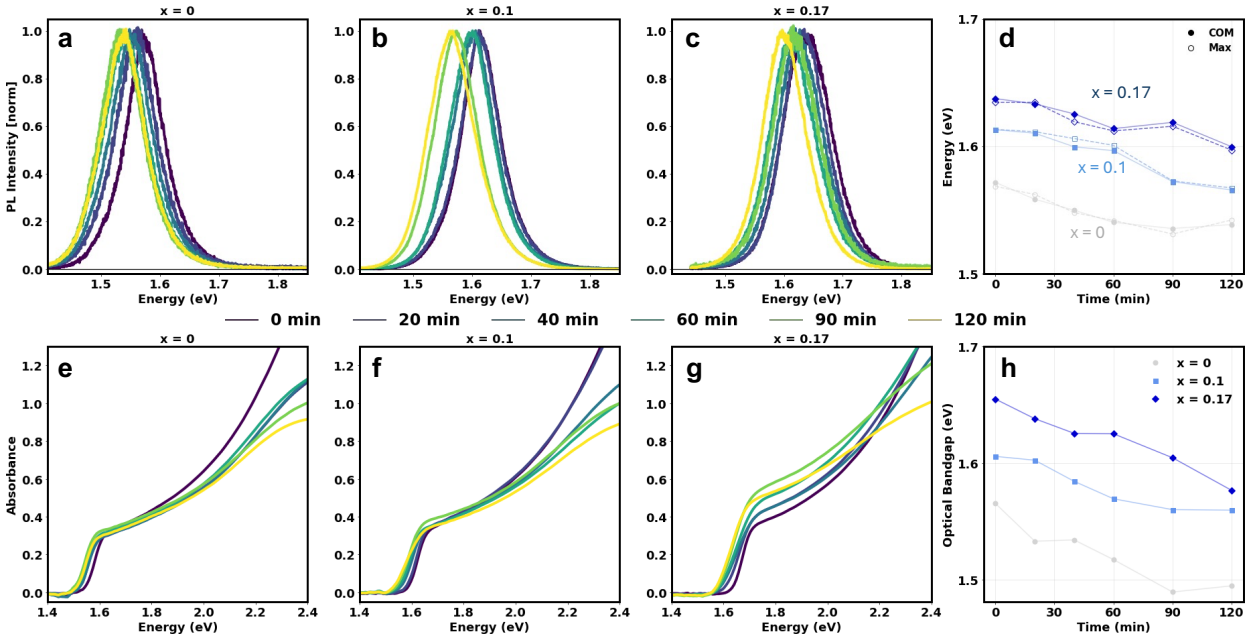

Figure 5.3. **Optical Analysis of $FA_{0.8}Cs_{0.2}Pb(I_xBr_{1-x})_3$ Thin Films Upon Exposure to I_2 vapor.** (a-c) Photoluminescence spectra of (a) $FA_{0.8}Cs_{0.2}PbI_3$, (b) $FA_{0.8}Cs_{0.2}Pb(I_{0.9}Br_{0.1})_3$, and (c) $FA_{0.8}Cs_{0.2}Pb(I_{83}Br_{0.17})_3$ over the period of 120 minutes of exposure to xx Pa of I_2 vapor. (d) Calculated PL center of max and corresponding photon energy for each composition over the period of exposure. (e-g) Photoluminescence spectra of (e) $FA_{0.8}Cs_{0.2}PbI_3$, (f) $FA_{0.8}Cs_{0.2}Pb(I_{0.9}Br_{0.1})_3$, and (g) $FA_{0.8}Cs_{0.2}Pb(I_{83}Br_{0.17})_3$ over the period of 120 minutes of I_2 vapor exposure. (h) Optical bandgap calculated from a Tauc fit for composition over time.

From a stability comparison perspective, the red shift of the optical properties prevents direct kinetic analysis, since a changing bandgap introduces uncertainty in the absorption coefficients. Consistent absorption coefficients have underpinned prior kinetic studies based on absorbance measurements.[34,35] To circumvent this limitation, we turned to x-ray diffraction (XRD), which directly probes crystalline structure and enables quantitative kinetic analysis when tracked over the course of degradation. Accordingly, we performed identical I_2-exposure experiments, with the only modification being that films were maintained at 45°C. This elevated temperature accelerates degradation by increasing the I_2 vapor concentration, thereby improving resolution of stability differences between compositions.

The XRD results are shown in Figure 5.4, with zoomed-in diffractograms highlighting phase evolution. Kinetic modeling was focused on the least-overlapped, phase-diagnostic reflections: the (110) perovskite (~13.9°), (002) δ-$CsPbI_3$ (~9.8°), and (110) δ-$FAPbI_3$ (~11.9°), highlighted in light blue, orange, and green in Figure 5.4a-c. We also note the presence of the (001) PbI_2 reflection at 12.6° (purple highlight in Figure 5.4a-c), Additional reflections from these phases are visible and follow similar qualitative evolution (SI Figure 5.9 shows a broader two-theta range) but were not modeled individually to avoid overlap and low-SNR bias. Figure 5.4d–f presents the integrated time-series intensities for the (110) perovskite peak, the (002) δ-$CsPbI_3$ peak, and the (110) δ-$FAPbI_3$, respectively. Substantial loss of the (110) reflection is observed in the x = 0 films, whereas the x = 0.1 films show only modest loss and the x = 0.17 films show negligible loss over the 120-minute exposure. This stability trend is corroborated by the secondary phases: the δ-$CsPbI_3$ peak grows rapidly in x = 0, more slowly in x = 0.1, and is suppressed in x = 0.17, while the δ-$FAPbI_3$ peak exhibits dramatic growth only in x = 0 with very minimal growth in the bromide containing films. Taken together, these results demonstrate that higher bromine content substantially improves phase stability under I_2 vapor exposure, suppressing both perovskite decomposition and the emergence of non-perovskite δ-phases.

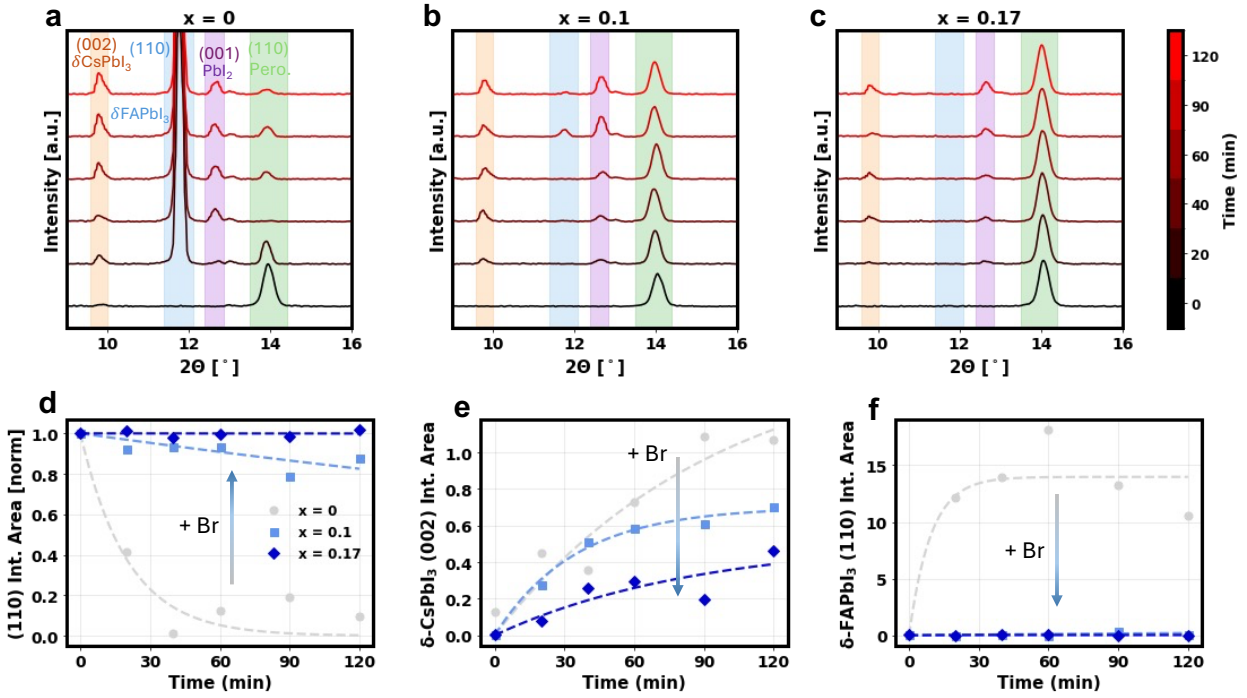

Figure 5.4. **XRD Analysis of $FA_{0.8}Cs_{0.2}Pb(I_xBr_{1-x})_3$ Thin Films Upon Exposure to I_2 vapor.** (a-c) XRD patterns of (a) $FA_{0.8}Cs_{0.2}PbI_3$, (b) $FA_{0.8}Cs_{0.2}Pb(I_{0.9}Br_{0.1})_3$, and (c) $FA_{0.8}Cs_{0.2}Pb(I_{83}Br_{0.17})_3$ over the period of 120 minutes of exposure to xx Pa of I_2 vapor. Integrated peak areas over the 120-minute exposure period for the (d) main perovskite (110) peak, (e) δ-CsPbI3 (002) peak, and (f) and the δ-$FAPbI_3$ (110) peak.

5.5 Discussion and Outlook

We characterized the stability of $FA_{0.8}Cs_{0.2}Pb(I_xBr_{1-x})_3$ (x=0, 0.1, 0.17) thin films under photo-stress and controlled I_2 vapor exposure, stressors that are expected to act in parallel in well-encapsulated perovskite solar cells. Under photo-stress, increasing bromide content accelerates the formation of reduced-lead defects. Consistently, *in situ* measurements of ambipolar diffusion length reveal faster decay in bromide-rich films, establishing a clear correlation between composition, susceptibility to defect formation, and the loss of optoelectronic performance.

In contrast, when exposed to I_2 vapor, bromine rich films exhibit markedly greater structural stability. Optical measurements revealed progressive redshifts in photoluminescence and

absorption onsets, commensurate with iodine intercalation into the lattice. Complimentary XRD analysis captured the kinetics of phase evolution, showing that the 17% and 10% bromine films retained the parent perovskite phase more effectively than the pure-iodide composition. Bromine-containing films also exhibited slower growth of non-perovskite δ phases. These results demonstrate that while bromide incorporation is detrimental under intrinsic photostress, it enhances resistance to extrinsic iodine vapor, underscoring a fundamental trade-off in stability pathways.

These contrasting stability trends can be rationalized by two complementary factors. First, bromine-rich compositions exhibit deeper valence band levels, which increase the thermodynamic driving force for iodide oxidation. This accelerates reduced-lead defect formation under photostress, a process thought to depend critically on iodide oxidation that consumes photoexcited holes and leaves behind excess electrons. Xu et al. confirmed this mechanism experimentally using quartz crystal microbalance measurements, which showed increasing halide loss at higher bromine fractions in inorganic perovskites.[153] It is also notable that Sn-based perovskites, which have narrower bandgaps due to Sn substitution for Pb, show exceptional light stability and do not undergo halide segregation even at high bromine fractions.[89] Second, in the presence of iodine vapor, bromine incorporation may promote the formation of I_2Br^- polyhalide complexes. These species are thought to mediate halide exchange and drive segregation into iodide-rich and bromide-rich domains.[159,160] At the same time, their formation may also act as a chemical buffer by sequestering reactive I_2/I_3^-, thereby suppressing the nucleation of non-perovskite δ-phases. Together, these mechanisms provide a framework for understanding why bromide simultaneously undermines intrinsic photostability while enhancing resistance to extrinsic I_2 vapor.

Compositional tuning remains a central strategy for optimizing both performance and stability in perovskite materials and devices. Establishing which processes ultimately limit performance is therefore critical to guiding composition choice. High efficiency and stability have been demonstrated across a wide range of perovskite compositions, but our photostability results help clarify why recent reports of pure-iodide perovskites have achieved such exceptional stability and performance.[161,162] Nevertheless, even limited I_2 evolution over time may still drive degradation, posing a challenge to realizing the decade-long operational lifetimes required for photovoltaic modules.

In conclusion, we have demonstrated that halide alloying plays a critical role in dictating the light-induced degradation kinetics of mixed-cation, mixed-halide lead halide perovskites. Bromine incorporation accelerates the formation of reduced-lead defects under photo-stress, leading to faster transport degradation, yet simultaneously suppresses perovskite decomposition under I_2 vapor exposure by stabilizing the parent phase against δ-phase growth. These dual behaviors highlight the need to evaluate compositional stability across both intrinsic and extrinsic degradation pathways, as these processes may act in parallel under device-relevant conditions. More broadly, our findings underscore that compositional engineering must be considered not only in terms of initial efficiency but also with respect to the coupled chemical and electronic processes that determine long-term operational stability. Future efforts to integrate defect energetics, halide chemistry, and encapsulation strategies will be critical for realizing perovskite modules with reliable, decades-long lifetimes.

5.6 Supporting Information

5.6.1 Experimental Methods and Film Characterization

Sample Preparation: $FA_{0.8}Cs_{0.2}Pb(I_{1-x}Br_x)_3$ precursor inks were prepared by dissolving stoichiometric CsI (FISHER SCIENTIFIC, 99.998%), FAI (Greatcell Solar Materials, >99.99%), PbI_2 (TCI AMERICA, 99.99%, trace metals basis) and $PbBr_2$ (TCI AMERICA, >98.0%) at 1 M concentration in 1/1 vol/vol N-methyl-2-pyrrolidone (NMP)/dimethylformamide (DMF), then allowed to dissolve overnight at 25°C. Glass substrates (15mm square) were cleaned with a four-step procedure by sonicating for 10 minutes each in (1) Alconox and DI water, then (2) DI water, then (3) acetone, and finally (4) 2-propanol. Shortly before spin coating, the substrates were cleaned for 10 minutes in an air plasma. $FA_{0.8}Cs_{0.2}Pb(I_{1-x}Br_x)_3$ thin films were fabricated via spin coating in a N_2-filled glovebox. Before spin coating, the precursor inks were filtered through a 0.2 μm PTFE filter. 50 μL of the filtered precursor ink was spin coated at 4000 rpm for 45 sec. With 15 seconds remaining in the spin cycle, an antisolvent wash of 0.6 ml of toluene was dripped onto the sample to induce crystallization. Upon completion of the 45 second spin cycle, the films were annealed on a ceramic hotplate at 120°C for 15 minutes. Films for each composition averaged ~300 nm in thickness as measured with a Bruker OM-DektakXT stylus profilometer. For degradation experiments in which diffusion length measurements are also taken, 80nm Au contact pads (separation of 0.01 cm) were deposited via thermal evaporation at a rate of 2 Å/s.

Perovskite Film Characterization: Scanning electron microscopy (SEM) micrographs were obtained using a ThermoFisher Scientific Apreo-S. Thin film X-ray diffraction (XRD) measurements were collected with a Bruker D8 Discover instrument equipped with a Pilatus 100K large area 2D detector and a Cu anode (wavelength 1.542 Å, Kα radiation). The X-ray beam size was defined with a 0.3 mm collimator. Optical absorbance spectra were collected from a PerkinElmer Lambda 1050 UV/vis/NIR spectrometer with an integrating sphere in laboratory atmosphere. Absorbance was calculated from separate measurements of sample percent transmittance and sample percent reflectance. Absorptance was calculated as $\mathcal{A} = 1 - \mathcal{T} - \mathcal{R}$. PL spectra were obtained with a modified Horiba LabRAM HR-800 with 532 nm laser excitation and a 10x objective lens. The adjustable confocal hole was set to 800 μm, and a 150 gr/mm Czerny−Turner monochromator blazed at 500 nm was used. To account for spectral artifacts in the detection system, a calibration procedure was done using a blackbody source (IR- 301, Infrared Systems Development) at 850, 950, and 1050 °C with a 10 μm pinhole (the calibration factor was averaged between the three temperatures to minimize error). To calculate 1 sun excitation flux, an Oriel optical power meter and Thorlabs beam profiler were used to set the photon flux equal to above bandgap photon flux of the AM1.5 GT solar spectrum (reference for the 1.66 eV x = 0.17 films).

***In situ* Optoelectronic Degradation Experiments**: For these degradation experiments, we place the sample, prepared as described above (with Au contact pads), in a Linkam Scientific LTSE420-P environmental test chamber, outfitted with an electric heater, gas ports, electrical probes, and windows above and below the sample. The atmosphere was controlled by connecting a cylinder of N_2 (99.998%, 4.8 grade, Praxair) through an Omega FMA5400/5500 mass flow controller to

the gas port on the Linkam chamber, maintaining a constant total gas flow set at 3.0 L/min. We use a calibrated 540 nm LED (Lumencor SpectraX Light Engine) as the light source in a metallurgical upright microscope (Olympus BX53M, equipped with a 5x Mitutoyo Plan Apo NIR HR objective lens), and adjust the input power based on the sample band gap to obtain the desired 1 sun equivalent flux of above-band gap photons under the AM1.5G spectrum. Photoconductivity was measured by connecting Au contacts to a Keithley 2420 source meter and sourcing + or – 3V while measuring current. The polarity of the applied voltage is switched every measurement to prevent artifacts from ion migration and buildup over the duration of the experiment due to consistent applied voltage. All data collected is automated with a Python master control program that takes measurements every 5 minutes. This general procedure has been described previously.[82]

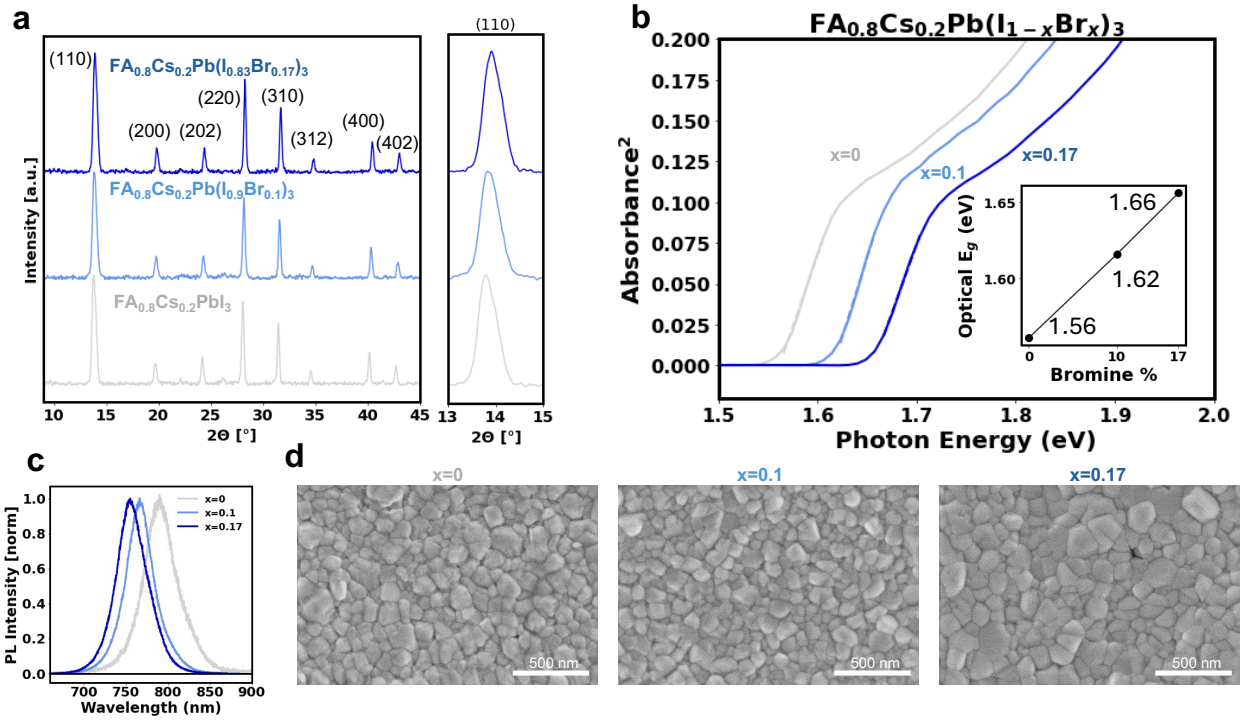

Figure 5.5. **Characterization of Fresh $FA_{0.8}Cs_{0.2}Pb(I_{1-x}Br_x)_3$ Thin Films.** (a) Diffractograms, (b) absorbance spectra with Tauc bandgap energy fits, (c) normalized photoluminescence spectra, and (d) scanning electron micrographs of the perovskite thin films.

5.6.2 Photoluminescence Stability Measurements

To assess stability in the spectral photoluminescence necessary to exclude halide phase segregation as a competing factor in the degradation of film optoelectronic quality, the PL spectrum of the thin films was measured over the course of continuous illumination from a 532 continuous wave laser (calibrated to 1-sun equivalent photon flux for the x = 0.17 composition). The PL was measured

every minute for the first 10 minutes of exposure, followed by every 10 minutes until 60 total minutes. Films were maintained in a dry N_2 ambient at 35°C.

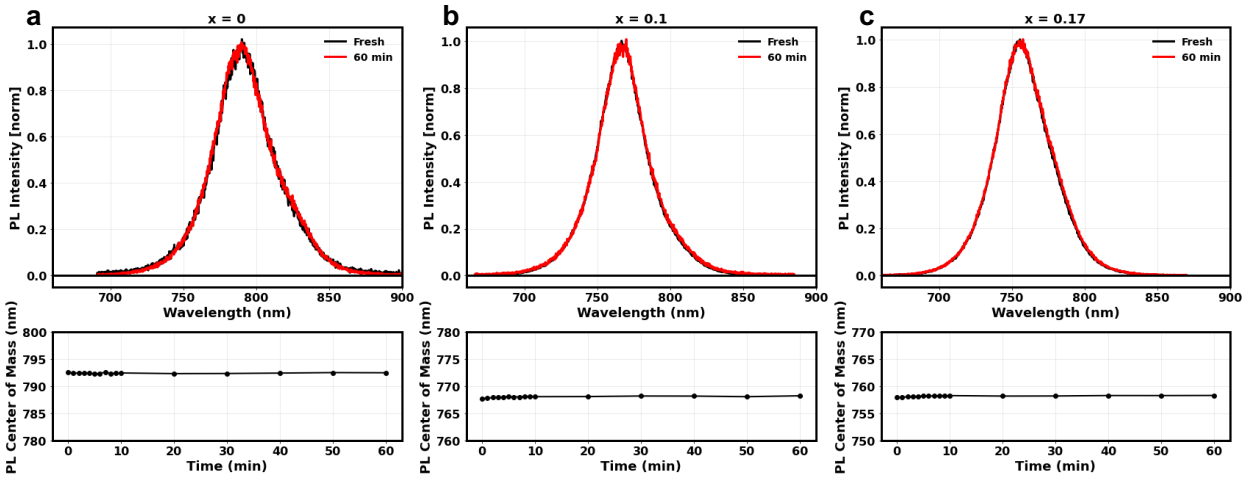

Figure 5.6. **Photoluminescence spectral stability measurements.** Normalized photoluminescence spectra of (a) $FA_{0.8}Cs_{0.2}PbI_3$, (b) $FA_{0.8}Cs_{0.2}Pb(I_{0.9}Br_{0.1})_3$, and (c) $FA_{0.8}Cs_{0.2}Pb(I_{0.83}Br_{0.17})_3$ perovskite thin films, respectively, before and after 1 hour of photo stress from 532 nm CW laser illumination (1.5×10^{21} photos/(m^2s) [~55 mW/cm^2]) at 35°C under flowing N_2. PL center of mass is tracked over time and plotted below each spectrum (measured at multiple time points), demonstrating the spectral stability for each of the samples under standard illumination conditions.

5.6.3 Change in Absorbance of all films at all temperatures

Here, we report the acquired absorbance spectrum for each of the films at the elevated temperatures of 55°C and 85°C. The raw data is included in Fig S3. The calculated absorbance at 1000 nm versus time is shown in FigS4. The linear fits to the absorbance at 1000 nm versus time is included in Table S1.

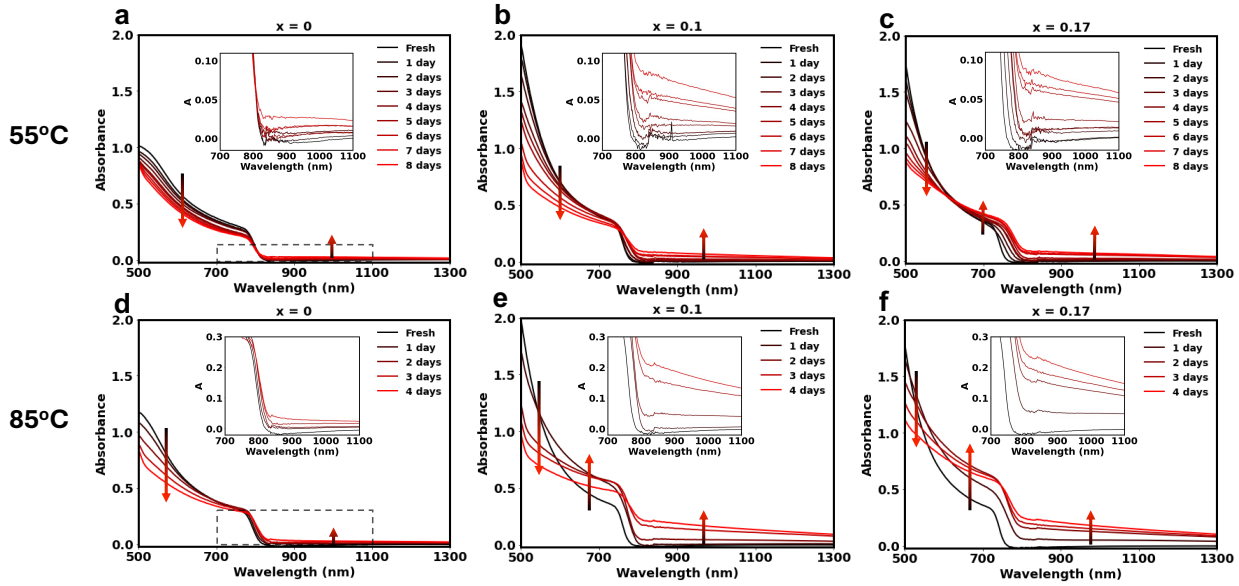

Figure 5.7. **Absorbance spectra for Light-Induced Degradation of $FA_{0.8}Cs_{0.2}Pb(I_{1-x}Br_x)_3$ Thin Films.** Absorbance spectra of (a,d) $FA_{0.8}Cs_{0.2}PbI_3$, (b,e) $FA_{0.8}Cs_{0.2}Pb(I_{0.9}Br_{0.1})_3$, and (c,f) $FA_{0.8}Cs_{0.2}Pb(I_{0.83}Br_{0.17})_3$ perovskite thin films, respectively, over the course of photo stress from a broad spectrum white LED illumination at 55°C (a-c) and 85°C (d-f) in a N_2 glovebox. Separate measurements of sample percent transmittance and percent reflectance were taken to calculate the film absorbance at each time point. The 1000 nm absorbance at each time point is used to calculate the rate of sub bandgap absorbance increase as a proxy for reduced lead species.

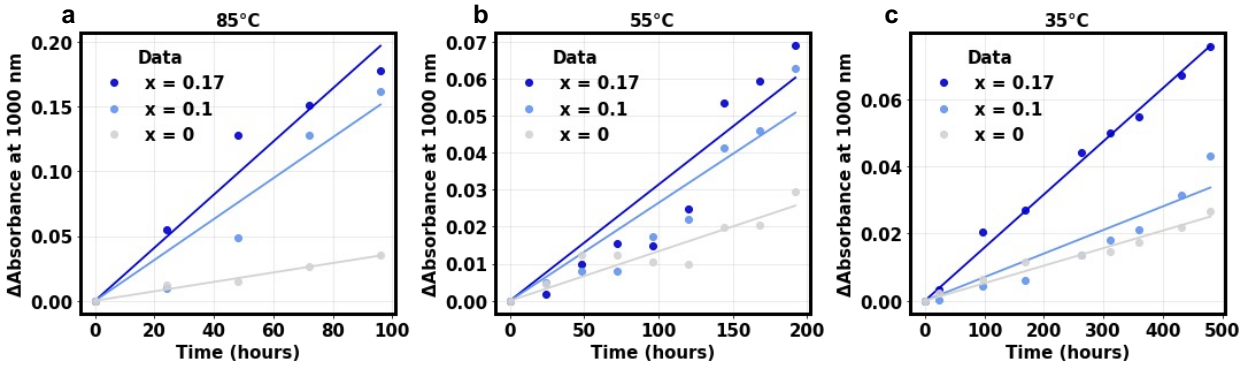

Figure 5.8. **Timeseries 1000 nm absorbance for $FA_{0.8}Cs_{0.2}Pb(I_{1-x}Br_x)_3$ Thin Films During Photostress.** Change in 1000 nm absorbance at (a) 85°C, (b) 55°C, and (c) 35°C for $FA_{0.8}Cs_{0.2}Pb(I_{1-x}Br_x)_3$ thin films. The data presented is here is the same as that presented in Fig S3 above and Fig S4c is identical to Fig2d in the main text.

Table 5-1. **Change in absorbance per unit time for $FA_{0.8}Cs_{0.2}Pb(I_{1-x}Br_x)_3$ thin films at 35°C, 55°C, and 85°C.**

	Temp. \ Comp.	x = 0	x = 0.1	x = 0.17
dA/dt @ 1000 nm (1/min) x 10^{-6}	35°C	0.87	1.17	2.64
	55°C	2.23	4.41	5.23
	85°C	6.07	26.3	34.2

5.6.4 X-ray Diffraction Peak Identification

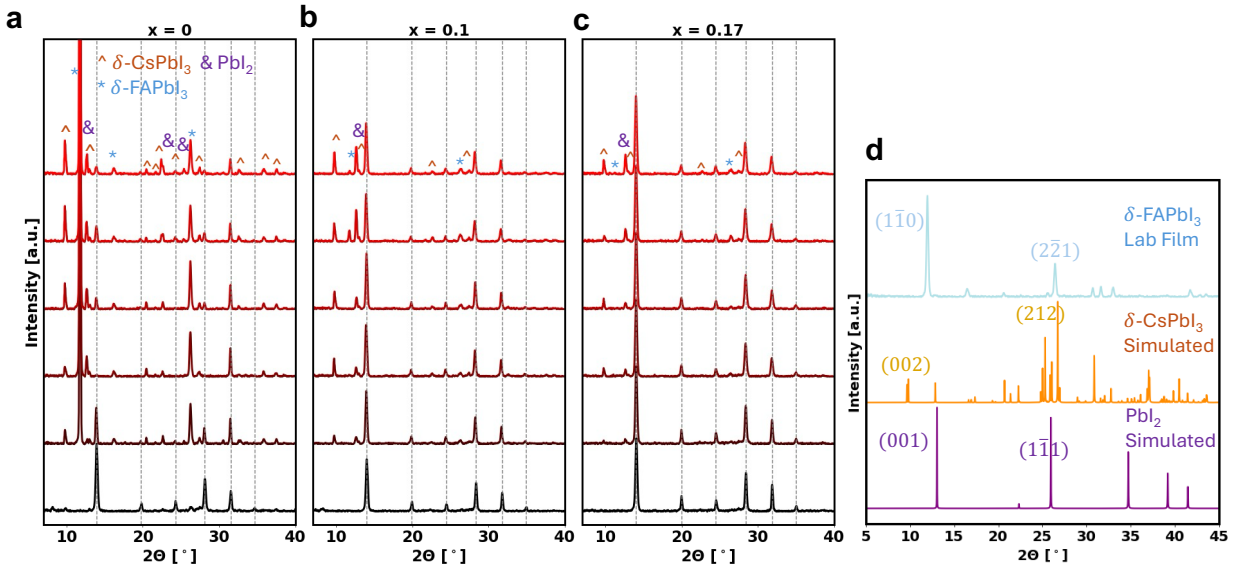

Figure 5.9. **XRD Peak Identification of $FA_{0.8}Cs_{0.2}Pb(I_{1-x}Br_x)_3$ Thin Films Over the Course of I_2 Vapor Exposure.** Diffractograms of (a) $FA_{0.8}Cs_{0.2}PbI_3$, (b) $FA_{0.8}Cs_{0.2}Pb(I_{0.9}Br_{0.1})_3$, and (c) $FA_{0.8}Cs_{0.2}Pb(I_{0.83}Br_{0.17})_3$ perovskite thin films over the course of 120 minutes of I_2 exposure. (d) Diffractograms of reference crystalline species for product identification, included lab made δ-$FAPbI_3$ and simulated δ-$CsPbI_3$ (CIF file retrieved from The Materials Project, mp-540839[163]) and PbI_2 (CIF file retrieved from the Crystallography OPEN Database, COD #1010062[164]). Simulated diffraction patterns were simulated on Vesta software using CIF files from publicly available databases.

6 Conclusions and Outlook

Metal halide perovskites represent an extraordinary class of semiconductors that have challenged long-standing assumptions about what defines a high-quality optoelectronic material. Whereas previous generations of solar absorbers required expensive, precision manufacturing to achieve near-perfect crystallinity, perovskites achieve exceptional performance through simple, low-cost processing from solution or vapor. This remarkable combination of ease of fabrication and high efficiency has made halide perovskites a leading candidate for the next generation of scalable, low-cost photovoltaic modules, positioning them to play a pivotal role in the global clean energy transition. However, despite their promise, these materials are not without significant challenges.[165]

These challenges arise almost entirely from stability issues associated with the perovskite absorber itself. Owing to their ionic nature, halide perovskites are chemically reactive with many species present in the ambient environment, most notably oxygen and water, and can even undergo self-driven degradation under illumination through reactions involving photoexcited charge carriers and the formation of decomposition byproducts such as molecular iodine. As a result, stability remains the critical hurdle presently limiting the commercialization of these materials and the next generation of optoelectronic devices they enable.[166] While the majority of this work has focused on elucidating the kinetics and mechanisms of perovskite decomposition, it is worth reflecting on recent advances and emerging strategies aimed at overcoming these stability challenges.

6.1 Recent Advances in Perovskite Solar Cell Performance and Stability

Contemporary research in perovskite solar cells (PSCs) largely focuses on two architectures: (1) single-junction devices and (2) perovskite-on-silicon tandems. Although all-

perovskite tandem structures once attracted significant attention, their development has been hindered by the limited efficiency and poor stability of low-bandgap (~1.2 eV) tin-based perovskites. These materials are prone to oxidation of Sn^{2+} to Sn^{4+}, which induces p-type doping and accelerates degradation in the presence of oxygen.[167] Recent progress in PSC performance and stability has therefore been driven primarily by advances in interface passivation, interlayer engineering, and improvements in absorber film quality and defect passivation.

Device interlayer passivation aims to enhance both performance and stability by incorporating additional layers that suppress the undesirable migration of ions, atoms, and molecules between adjacent device layers while also improving mechanical integrity. These passivation layers can be introduced at either the top or buried interfaces between the perovskite absorber and the charge transport layers. Li et al. demonstrated that incorporating a two-dimensional (2D) graphene layer at the top interface improved device stability and mechanical robustness.[168] Similarly, Zai et al. showed that introducing 2D molybdenum disulfide (MoS_2) at the buried interface effectively inhibited ion migration within the perovskite layer.[169] Other studies have explored the use of 2D perovskite interlayers to improve both performance and stability.[170,171] However, these 2D perovskite structures are likely subject to degradation pathways similar to those of their 3D counterparts. Consequently, more robust materials like MoS_2 and graphene may represent more durable strategies for interfacial passivation, mechanical reinforcement, and ion blocking.

Recent progress in absorber quality has also yielded notable improvements in both performance and operational stability for α-$FAPbI_3$ through the development of novel growth strategies. Sidhik et al. demonstrated that two-dimensional perovskite layers can effectively seed

the formation of structurally robust α-$FAPbI_3$, enhancing phase stability and device longevity.[161] Similarly, Zhang et al. employed an iodine intercalation approach to achieve highly stable α-$FAPbI_3$ films with improved crystallinity and resistance to phase degradation.[162] In both cases, the resulting devices exhibited minimal efficiency loss after more than 1,000 hours of continuous operation at 85°C under one-sun illumination.

In the context of the work presented here, two-dimensional (2D) device interlayers represent an excellent strategy for mitigating the intrinsic challenges associated with three-dimensional (3D) perovskite materials. Such interlayers can enhance the mechanical integrity of the inherently soft perovskite lattice while simultaneously suppressing ionic migration, making them highly valuable for improving both device efficiency and stability. Likewise, the controlled growth of high-quality, pure-iodide perovskites offers a promising pathway to reduce the compositional inhomogeneities that often compromise the performance and long-term stability of alloyed perovskite systems. The relatively narrow bandgap of α-$FAPbI_3$ also reduces the driving force for halide oxidation, further supporting its stability. Thus, strategies that suppress the undesirable but thermodynamically favored transition to the δ-phase could offer substantial upside for achieving simultaneously efficient and durable perovskite solar cells.

6.2 Toward Efficient and Stable Perovskite Solar Modules

A key challenge facing the current trajectory of perovskite research is the limited availability of module-level stability data. Most studies that investigate device stability report results from small-area test cells—typically less than 1 cm^2—comparing new fabrication or passivation strategies against control devices. While such studies are invaluable for uncovering fundamental mechanisms and advancing materials design, their relevance to commercial-scale

modules remains indirect. At this stage of perovskite PV maturity, field-validated module data are essential for bridging the gap between laboratory success and industrial deployment.[27] The Photovoltaic Accelerator for Commercializing Technologies (PACT), a joint initiative between Sandia National Laboratories and the National Renewable Energy Laboratory, has made important progress toward this goal by deploying perovskite modules for real-world testing, initiating the critical cycle of field learning needed to advance commercialization. These efforts mark an exciting and necessary step toward realizing the full potential of perovskite photovoltaics.

Several early-stage companies are actively pursuing the commercialization of perovskite photovoltaics, though most remain in preliminary stages as stability challenges continue to be addressed. Oxford Photovoltaics stands out as a leading example, having introduced commercial perovskite–silicon tandem modules and reported module efficiencies approaching 27% for an area of 1.6 m^2.[172] These milestones are highly encouraging and demonstrate tangible progress toward market readiness. Nonetheless, continued fundamental research into perovskite chemistry, coupled with applied studies on cell and module engineering, will be essential for establishing the lifetime guarantees and bankability required for large-scale adoption. Equally critical is for the field to learn from the deployment practices of existing photovoltaic technologies and accelerate the installation of perovskite modules in outdoor environments to gather real-world performance data.

6.3 Concluding Thoughts

The work presented in this thesis sought to elucidate the fundamental properties of alloyed perovskite semiconductors and their implications for next-generation photovoltaic technologies. Although perovskite PV has advanced remarkably, thanks to the efforts of thousands of researchers worldwide, many questions remain, particularly regarding long-term stability and module-scale performance. In the author's view, perovskite photovoltaics face a challenging but achievable path

toward commercialization, with the foremost hurdle being the realization of operational lifetimes spanning multiple decades. Achieving this goal will require continued investigation into chemically and mechanically robust interlayers, as well as intrinsically stable perovskite absorber compositions, to enable the development of truly durable, high-efficiency solar modules capable of contributing meaningfully to the global energy transition.

7 Vita

Spencer G. Cira earned dual Bachelor of Science in Engineering (B.S.E.) degrees in Chemical Engineering and Engineering Physics from the University of Michigan, Ann Arbor in 2021. While at Michigan, he conducted research with Professor Andrej Lenert on nanostructured polymer films for radiative cooling applications. Following graduation, Spencer began his Ph.D. studies in Chemical Engineering at the University of Washington in Fall of 2021, where he worked under the guidance of Professor Hugh W. Hillhouse to investigate the fundamental processes governing the degradation of metal halide perovskite semiconductors. Spencer currently lives in Seattle, WA and enjoys trail running, ski mountaineering, and spending meaningful time with friends and family.

8 Bibilography

(1) Joel Mokyr. *The Enlightened Economy: An Economic History of Britain 1700-1850*; Yale University Press, 2012.

(2) Intergovernmental Panel on Climate Change (IPCC). *Climate Change 2022 – Impacts, Adaptation and Vulnerability*; Cambridge University Press, 2023. https://doi.org/10.1017/9781009325844.

(3) Eurofound and International Labour Organization (2019), Working Conditions in a Global Perspective, Publications Office of the European Union, Luxembourg, and International Labour Organization, Geneva.

(4) Peter Brimblecombe. *The Big Smoke: A History of Air Pollution in London since Medieval Times*; Routledge Revivals, 1987.

(5) Vaclav Smil. *Energy and Civilization: A History*, 2nd ed.; The MIT Press, 2017.

(6) IEA (2023), World Energy Outlook 2023, IEA, Paris Https://Www.Iea.Org/Reports/World-Energy-Outlook-2023, Licence: CC BY 4.0 (Report); CC BY NC SA 4.0 (Annex A).

(7) Ramanathan, V.; Coakley, J. A. Climate Modeling through Radiative-convective Models. *Reviews of Geophysics* **1978**, *16* (4), 465–489. https://doi.org/10.1029/RG016i004p00465.

(8) Raymond T. Pierrehumbert. *Principles of Planetary Climate*; Cambridge University Press, 2010.

(9) *NOAA Global Monitoring Laboratory. Trends in Atmospheric Carbon Dioxide: Mauna Loa CO2 Record. Accessed October 2025. Https://Gml.Noaa.Gov/Ccgg/Trends/*.

(10) Rockström, J.; Steffen, W.; Noone, K.; Persson, Å.; Chapin, F. S.; Lambin, E. F.; Lenton, T. M.; Scheffer, M.; Folke, C.; Schellnhuber, H. J.; Nykvist, B.; de Wit, C. A.; Hughes, T.; van der Leeuw, S.; Rodhe, H.; Sörlin, S.; Snyder, P. K.; Costanza, R.; Svedin, U.; Falkenmark, M.; Karlberg, L.; Corell, R. W.; Fabry, V. J.; Hansen, J.; Walker, B.; Liverman, D.; Richardson, K.; Crutzen, P.; Foley, J. A. A Safe Operating Space for Humanity. *Nature* **2009**, *461* (7263), 472–475. https://doi.org/10.1038/461472a.

(11) Vignesh Ramasamy; Jarett Zuboy; Michael Woodhouse; Eric O'Shaughnessy; David Feldman; Jal Desai; Andy Walker; Robert Margolis; Paul Basore. *U.S. Solar Photovoltaic System and Energy Storage Cost Benchmarks, With Minimum Sustainable Price Analysis: Q1 2023*; 2023.

(12) Mitra, P. *Integrating Climate Change into Macroeconomic Analysis: A Review of Impact Channels, Data, Models, and Scenarios*; 2025.

(13) Jaquelin Cochran; Paul Denholm; Bethany Speer; Mackay Miller. *Grid Integration and the Carrying Capacity of the U.S. Grid to Incorporate Variable Renewable Energy*; 2015.

(14) *Solar Futures Study*; 2021.

(15) *Global Energy Perspective 2024*; 2024.

(16) Lee, T. D.; Ebong, A. U. A Review of Thin Film Solar Cell Technologies and Challenges. *Renewable and Sustainable Energy Reviews*. Elsevier Ltd 2017, pp 1286–1297. https://doi.org/10.1016/j.rser.2016.12.028.

(17) *Annual Report 2024*; Tempe, AZ, 2024.

(18) Snaith, H. J. Perovskites: The Emergence of a New Era for Low-Cost, High-Efficiency Solar Cells. *Journal of Physical Chemistry Letters*. November 7, 2013, pp 3623–3630. https://doi.org/10.1021/jz4020162.

(19) Simon Philipps. *Photovoltaics Report*; 2025.
(20) Ballif, C.; Haug, F. J.; Boccard, M.; Verlinden, P. J.; Hahn, G. Status and Perspectives of Crystalline Silicon Photovoltaics in Research and Industry. *Nature Reviews Materials*. Nature Research August 1, 2022, pp 597–616. https://doi.org/10.1038/s41578-022-00423-2.
(21) Hammer, M. S.; Schlott, H.; Lüer, L.; Brabec, C. J.; Sytnyk, M.; Will, J.; Meyer, B.; Heiss, W. Bridging Theory and Experiment in Defect-Tolerant Semiconductors for Photovoltaics. *Nat Rev Mater* **2025**, *10* (4), 311–325. https://doi.org/10.1038/s41578-024-00769-9.
(22) Renewable Energy Laboratory, N. *NREL Best Research-Cell PV Efficiency Chart*; 1976.
(23) Unger, E. L.; Kegelmann, L.; Suchan, K.; Sörell, D.; Korte, L.; Albrecht, S. Roadmap and Roadblocks for the Band Gap Tunability of Metal Halide Perovskites. *J Mater Chem A Mater* **2017**, *5* (23), 11401–11409. https://doi.org/10.1039/c7ta00404d.
(24) Leijtens, T.; Bush, K. A.; Prasanna, R.; McGehee, M. D. Opportunities and Challenges for Tandem Solar Cells Using Metal Halide Perovskite Semiconductors. *Nature Energy*. Nature Publishing Group October 1, 2018, pp 828–838. https://doi.org/10.1038/s41560-018-0190-4.
(25) Siegler, T. D.; Dawson, A.; Lobaccaro, P.; Ung, D.; Beck, M. E.; Nilsen, G.; Tinker, L. L. The Path to Perovskite Commercialization: A Perspective from the United States Solar Energy Technologies Office. *ACS Energy Lett* **2022**, *7* (5), 1728–1734. https://doi.org/10.1021/acsenergylett.2c00698.
(26) Yang, J.; Kelly, T. L. Decomposition and Cell Failure Mechanisms in Lead Halide Perovskite Solar Cells. *Inorganic Chemistry*. American Chemical Society January 3, 2017, pp 92–101. https://doi.org/10.1021/acs.inorgchem.6b01307.
(27) Silverman, T. J.; Deceglie, M. G.; Repins, I.; Owen-Bellini, M.; Berry, J. J.; Stein, J. S.; Schelhas, L. T. Durability Research Is Pivotal for Perovskite Photovoltaics. *Nat Energy* **2025**. https://doi.org/10.1038/s41560-025-01786-w.
(28) Uličná, S.; Schall, J. W.; Hayden, S. C.; Irvin, N. P.; Silverman, T. J.; Fei, C.; Shi, X.; Arnold, R. L.; McDanold, B.; Parker, J.; Huang, J.; Berry, J. J.; Stein, J. S.; Kern, D. B.; Owen-Bellini, M.; Schelhas, L. T. Field-Relevant Degradation Mechanisms in Metal Halide Perovskite Modules. *Adv Energy Mater* **2025**, *15* (23). https://doi.org/10.1002/aenm.202404518.
(29) Ross, J. R. G.; Smokler, M. I. *Flat-Plate Solar Array Project: Final Report: Volume 6, Engineering Sciences and Reliability*; 1986.
(30) Jordan, D. C.; Haegel, N.; Barnes, T. M. Photovoltaics Module Reliability for the Terawatt Age. *Progress in Energy*. Institute of Physics April 1, 2022. https://doi.org/10.1088/2516-1083/ac6111.
(31) Ross, R. T. Some Thermodynamics of Photochemical Systems. *J Chem Phys* **1967**, *46* (12), 4590–4593. https://doi.org/10.1063/1.1840606.
(32) Katahara, J. K.; Hillhouse, H. W. Quasi-Fermi Level Splitting and Sub-Bandgap Absorptivity from Semiconductor Photoluminescence. *J Appl Phys* **2014**, *116* (17). https://doi.org/10.1063/1.4898346.
(33) Stoddard, R. J.; Eickemeyer, F. T.; Katahara, J. K.; Hillhouse, H. W. Correlation between Photoluminescence and Carrier Transport and a Simple in Situ Passivation Method for High-Bandgap Hybrid Perovskites. *Journal of Physical Chemistry Letters* **2017**, *8* (14), 3289–3298. https://doi.org/10.1021/acs.jpclett.7b01185.

(34) Siegler, T. D.; Dunlap-Shohl, W. A.; Meng, Y.; Yang, Y.; Kau, W. F.; Sunkari, P. P.; Tsai, C. E.; Armstrong, Z. J.; Chen, Y. C.; Beck, D. A. C.; Meilă, M.; Hillhouse, H. W. Water-Accelerated Photooxidation of CH3NH3PbI3Perovskite. *J Am Chem Soc* **2022**, *144* (12), 5552–5561. https://doi.org/10.1021/jacs.2c00391.

(35) Meng, Y.; Sunkari, P. P.; Meilă, M.; Hillhouse, H. W. Chemical Reaction Kinetics of the Decomposition of Low-Bandgap Tin-Lead Halide Perovskite Films and the Effect on the Ambipolar Diffusion Length. *ACS Energy Lett* **2023**, *8* (4), 1688–1696. https://doi.org/10.1021/acsenergylett.2c02733.

(36) Cira, S. G.; Dunlap-Shohl, W. A.; Meng, Y.; Sunkari, P. P.; Folch, J. H.; Hillhouse, H. W. Light-Induced Degradation of Mixed-Cation, Mixed-Halide Perovskite: Observed Rates and Influence of Oxygen. *J Mater Chem A Mater* **2025**, *13* (7), 5033–5044. https://doi.org/10.1039/D4TA07807A.

(37) Vaynzof, Y. The Future of Perovskite Photovoltaics—Thermal Evaporation or Solution Processing? *Adv Energy Mater* **2020**, *10* (48). https://doi.org/10.1002/aenm.202003073.

(38) Stranks, S. D.; Eperon, G. E.; Grancini, G.; Menelaou, C.; Alcocer, M. J. P.; Leijtens, T.; Herz, L. M.; Petrozza, A.; Snaith, H. J. Electron-Hole Diffusion Lengths Exceeding 1 Micrometer in an Organometal Trihalide Perovskite Absorber. *Science (1979)* **2013**, *342*.

(39) Kojima, A.; Teshima, K.; Shirai, Y.; Miyasaka, T. Organometal Halide Perovskites as Visible-Light Sensitizers for Photovoltaic Cells. *J Am Chem Soc* **2009**, *131* (17), 6050–6051. https://doi.org/10.1021/ja809598r.

(40) Tao, S.; Schmidt, I.; Brocks, G.; Jiang, J.; Tranca, I.; Meerholz, K.; Olthof, S. Absolute Energy Level Positions in Tin- and Lead-Based Halide Perovskites. *Nat Commun* **2019**, *10* (1). https://doi.org/10.1038/s41467-019-10468-7.

(41) Cell-Efficiency-Data-Table.

(42) Ni, Z.; Bao, C.; Liu, Y.; Jiang, Q.; Wu, W.-Q.; Chen, S.; Dai, X.; Chen, B.; Hartweg, B.; Yu, Z.; Holman, Z.; Huang, J. *Resolving Spatial and Energetic Distributions of Trap States in Metal Halide Perovskite Solar Cells*. https://www.science.org.

(43) Futscher, M. H.; Gangishetty, M. K.; Congreve, D. N.; Ehrler, B. Quantifying Mobile Ions and Electronic Defects in Perovskite-Based Devices with Temperature-Dependent Capacitance Measurements: Frequency vs Time Domain. *Journal of Chemical Physics* **2020**, *152* (4). https://doi.org/10.1063/1.5132754.

(44) Siekmann, J.; Ravishankar, S.; Kirchartz, T. Apparent Defect Densities in Halide Perovskite Thin Films and Single Crystals. *ACS Energy Letters*. American Chemical Society September 10, 2021, pp 3244–3251. https://doi.org/10.1021/acsenergylett.1c01449.

(45) Steirer, K. X.; Schulz, P.; Teeter, G.; Stevanovic, V.; Yang, M.; Zhu, K.; Berry, J. J. Defect Tolerance in Methylammonium Lead Triiodide Perovskite. *ACS Energy Lett* **2016**, *1* (2), 360–366. https://doi.org/10.1021/acsenergylett.6b00196.

(46) Kim, G. W.; Petrozza, A. Defect Tolerance and Intolerance in Metal-Halide Perovskites. *Advanced Energy Materials*. Wiley-VCH Verlag October 1, 2020. https://doi.org/10.1002/aenm.202001959.

(47) Boyd, C. C.; Cheacharoen, R.; Leijtens, T.; McGehee, M. D. Understanding Degradation Mechanisms and Improving Stability of Perovskite Photovoltaics. *Chemical Reviews*. American Chemical Society March 13, 2019, pp 3418–3451. https://doi.org/10.1021/acs.chemrev.8b00336.

(48) Xiao, Z.; Zhou, Y.; Hosono, H.; Kamiya, T.; Padture, N. P. Bandgap Optimization of Perovskite Semiconductors for Photovoltaic Applications. *Chemistry - A European Journal*. Wiley-VCH Verlag February 16, 2018, pp 2305–2316. https://doi.org/10.1002/chem.201705031.

(49) Berhe, T. A.; Su, W. N.; Chen, C. H.; Pan, C. J.; Cheng, J. H.; Chen, H. M.; Tsai, M. C.; Chen, L. Y.; Dubale, A. A.; Hwang, B. J. Organometal Halide Perovskite Solar Cells: Degradation and Stability. *Energy and Environmental Science*. Royal Society of Chemistry February 1, 2016, pp 323–356. https://doi.org/10.1039/c5ee02733k.

(50) Jeon, N. J.; Noh, J. H.; Yang, W. S.; Kim, Y. C.; Ryu, S.; Seo, J.; Seok, S. Il. Compositional Engineering of Perovskite Materials for High-Performance Solar Cells. *Nature* **2015**, *517* (7535), 476–480. https://doi.org/10.1038/nature14133.

(51) Dunfield, S. P.; Bliss, L.; Zhang, F.; Luther, J. M.; Zhu, K.; van Hest, M. F. A. M.; Reese, M. O.; Berry, J. J. From Defects to Degradation: A Mechanistic Understanding of Degradation in Perovskite Solar Cell Devices and Modules. *Advanced Energy Materials*. Wiley-VCH Verlag July 1, 2020. https://doi.org/10.1002/aenm.201904054.

(52) Ma, S.; Yuan, G.; Zhang, Y.; Yang, N.; Li, Y.; Chen, Q. Development of Encapsulation Strategies towards the Commercialization of Perovskite Solar Cells. *Energy and Environmental Science*. Royal Society of Chemistry January 1, 2022, pp 13–55. https://doi.org/10.1039/d1ee02882k.

(53) Hoke, E. T.; Slotcavage, D. J.; Dohner, E. R.; Bowring, A. R.; Karunadasa, H. I.; McGehee, M. D. Reversible Photo-Induced Trap Formation in Mixed-Halide Hybrid Perovskites for Photovoltaics. *Chem Sci* **2015**, *6* (1), 613–617. https://doi.org/10.1039/c4sc03141e.

(54) Lu, Y.; Hu, J.; Ge, Y.; Tian, B.; Zhang, Z.; Sui, M. Decisive Influence of Amorphous PbI2−xon the Photodegradation of Halide Perovskites. *J Mater Chem A Mater* **2021**, *9* (26), 15059–15067. https://doi.org/10.1039/d1ta01730f.

(55) Liang, J.; Hu, X.; Wang, C.; Liang, C.; Chen, C.; Xiao, M.; Li, J.; Tao, C.; Xing, G.; Yu, R.; Ke, W.; Fang, G. Origins and Influences of Metallic Lead in Perovskite Solar Cells. *Joule* **2022**, *6* (4), 816–833. https://doi.org/10.1016/j.joule.2022.03.005.

(56) Juarez-Perez, E. J.; Ono, L. K.; Maeda, M.; Jiang, Y.; Hawash, Z.; Qi, Y. Photodecomposition and Thermal Decomposition in Methylammonium Halide Lead Perovskites and Inferred Design Principles to Increase Photovoltaic Device Stability. *J Mater Chem A Mater* **2018**, *6* (20), 9604–9612. https://doi.org/10.1039/c8ta03501f.

(57) Li, Y.; Xu, X.; Wang, C.; Ecker, B.; Yang, J.; Huang, J.; Gao, Y. Light-Induced Degradation of CH3NH3PbI3 Hybrid Perovskite Thin Film. *Journal of Physical Chemistry C* **2017**, *121* (7), 3904–3910. https://doi.org/10.1021/acs.jpcc.6b11853.

(58) Kim, G. Y.; Senocrate, A.; Yang, T. Y.; Gregori, G.; Grätzel, M.; Maier, J. Large Tunable Photoeffect on Ion Conduction in Halide Perovskites and Implications for Photodecomposition. *Nat Mater* **2018**, *17* (5), 445–449. https://doi.org/10.1038/s41563-018-0038-0.

(59) Doherty, T. A. S.; Winchester, A. J.; Macpherson, S.; Johnstone, D. N.; Pareek, V.; Tennyson, E. M.; Kosar, S.; Kosasih, F. U.; Anaya, M.; Abdi-Jalebi, M.; Andaji-Garmaroudi, Z.; Wong, E. L.; Madéo, J.; Chiang, Y. H.; Park, J. S.; Jung, Y. K.; Petoukhoff, C. E.; Divitini, G.; Man, M. K. L.; Ducati, C.; Walsh, A.; Midgley, P. A.; Dani, K. M.; Stranks, S. D. Performance-Limiting Nanoscale Trap Clusters at Grain

Junctions in Halide Perovskites. *Nature* **2020**, *580* (7803), 360–366. https://doi.org/10.1038/s41586-020-2184-1.

(60) Macpherson, S.; Doherty, T. A. S.; Winchester, A. J.; Kosar, S.; Johnstone, D. N.; Chiang, Y. H.; Galkowski, K.; Anaya, M.; Frohna, K.; Iqbal, A. N.; Nagane, S.; Roose, B.; Andaji-Garmaroudi, Z.; Orr, K. W. P.; Parker, J. E.; Midgley, P. A.; Dani, K. M.; Stranks, S. D. Local Nanoscale Phase Impurities Are Degradation Sites in Halide Perovskites. *Nature* **2022**, *607* (7918), 294–300. https://doi.org/10.1038/s41586-022-04872-1.

(61) Ducati, C.; Ferrer Orri, J.; Yang, T.; Doherty, T.; Selby, T.; Chiang, Y.-H.; Anaya, M.; Allen, C. Visualising Nanoscale Bias-Induced Degradation in Halide Perovskite Solar Absorbers. **2023**. https://doi.org/10.21203/rs.3.rs-3224875/v1.

(62) Bai, Y.; Huang, Z.; Zhang, X.; Lu, J.; Niu, X.; He, Z.; Zhu, C.; Xiao, M.; Song, Q.; Wei, X.; Wang, C.; Cui, Z.; Dou, J.; Chen, Y.; Pei, F.; Zai, H.; Wang, W.; Song, T.; An, P.; Zhang, J.; Dong, J.; Li, Y.; Shi, J.; Jin, H.; Chen, P.; Sun, Y.; Li, Y.; Chen, H.; Wei, Z.; Zhou, H.; Chen, Q. *Initializing Film Homogeneity to Retard Phase Segregation for Stable Perovskite Solar Cells*. https://www.science.org.

(63) Frohna, K.; Anaya, M.; Macpherson, S.; Sung, J.; Doherty, T. A. S.; Chiang, Y. H.; Winchester, A. J.; Orr, K. W. P.; Parker, J. E.; Quinn, P. D.; Dani, K. M.; Rao, A.; Stranks, S. D. Nanoscale Chemical Heterogeneity Dominates the Optoelectronic Response of Alloyed Perovskite Solar Cells. *Nat Nanotechnol* **2022**, *17* (2), 190–196. https://doi.org/10.1038/s41565-021-01019-7.

(64) Wang, M.; Fei, C.; Uddin, A.; Huang, J. *Influence of Voids on the Thermal and Light Stability of Perovskite Solar Cells*; 2022; Vol. 8. https://www.science.org.

(65) McGovern, L.; Grimaldi, G.; Futscher, M. H.; Hutter, E. M.; Muscarella, L. A.; Schmidt, M. C.; Ehrler, B. Reduced Barrier for Ion Migration in Mixed-Halide Perovskites. *ACS Appl Energy Mater* **2021**, *4* (12), 13431–13437. https://doi.org/10.1021/acsaem.1c03095.

(66) Mundt, L. E.; Zhang, F.; Palmstrom, A. F.; Xu, J.; Tirawat, R.; Kelly, L. L.; Stone, K. H.; Zhu, K.; Berry, J. J.; Toney, M. F.; Schelhas, L. T. Mixing Matters: Nanoscale Heterogeneity and Stability in Metal Halide Perovskite Solar Cells. *ACS Energy Lett* **2022**, *7* (1), 471–480. https://doi.org/10.1021/acsenergylett.1c02338.

(67) Roose, B.; Dey, K.; Chiang, Y. H.; Friend, R. H.; Stranks, S. D. Critical Assessment of the Use of Excess Lead Iodide in Lead Halide Perovskite Solar Cells. *Journal of Physical Chemistry Letters* **2020**, *11* (16), 6505–6512. https://doi.org/10.1021/acs.jpclett.0c01820.

(68) Donakowski, A.; Miller, D. W.; Anderson, N. C.; Ruth, A.; Sanehira, E. M.; Berry, J. J.; Irwin, M. D.; Rockett, A.; Steirer, K. X. Improving Photostability of Cesium-Doped Formamidinium Lead Triiodide Perovskite. *ACS Energy Lett* **2021**, *6* (2), 574–580. https://doi.org/10.1021/acsenergylett.0c02339.

(69) Kerner, R. A.; Xu, Z.; Larson, B. W.; Rand, B. P. The Role of Halide Oxidation in Perovskite Halide Phase Separation. *Joule*. Cell Press September 15, 2021, pp 2273–2295. https://doi.org/10.1016/j.joule.2021.07.011.

(70) Hoke, E. T.; Slotcavage, D. J.; Dohner, E. R.; Bowring, A. R.; Karunadasa, H. I.; McGehee, M. D. Reversible Photo-Induced Trap Formation in Mixed-Halide Hybrid Perovskites for Photovoltaics. *Chem Sci* **2015**, *6* (1), 613–617. https://doi.org/10.1039/c4sc03141e.

(71) Braly, I. L.; Stoddard, R. J.; Rajagopal, A.; Uhl, A. R.; Katahara, J. K.; Jen, A. K. Y.; Hillhouse, H. W. Current-Induced Phase Segregation in Mixed Halide Hybrid Perovskites

and Its Impact on Two-Terminal Tandem Solar Cell Design. *ACS Energy Lett* **2017**, *2* (8), 1841–1847. https://doi.org/10.1021/acsenergylett.7b00525.

(72) Dubose, J. T.; Kamat, P. V. Hole Trapping in Halide Perovskites Induces Phase Segregation. *Acc Mater Res* **2022**, *3* (7), 761–771. https://doi.org/10.1021/accountsmr.2c00076.

(73) Mathew, P. S.; Mathew, P. S.; Samu, G. F.; Samu, G. F.; Janáky, C.; Kamat, P. V.; Kamat, P. V.; Kamat, P. V. Iodine (I) Expulsion at Photoirradiated Mixed Halide Perovskite Interface. Should i Stay or Should i Go? *ACS Energy Lett* **2020**, *5* (6), 1872–1880. https://doi.org/10.1021/acsenergylett.0c00925.

(74) Samu, G. F.; Balog, Á.; De Angelis, F.; Meggiolaro, D.; Kamat, P. V.; Janáky, C. Electrochemical Hole Injection Selectively Expels Iodide from Mixed Halide Perovskite Films. *J Am Chem Soc* **2019**, *141* (27), 10812–10820. https://doi.org/10.1021/jacs.9b04568.

(75) Barboni, D.; De Souza, R. A. The Thermodynamics and Kinetics of Iodine Vacancies in the Hybrid Perovskite Methylammonium Lead Iodide. *Energy Environ Sci* **2018**, *11* (11), 3266–3274. https://doi.org/10.1039/c8ee01697f.

(76) Elmelund, T.; Seger, B.; Kuno, M.; Kamat, P. V. How Interplay between Photo and Thermal Activation Dictates Halide Ion Segregation in Mixed Halide Perovskites. *ACS Energy Lett* **2020**, *5* (1), 56–63. https://doi.org/10.1021/acsenergylett.9b02265.

(77) Rosales, B. A.; Schutt, K.; Berry, J. J.; Wheeler, L. M. Leveraging Low-Energy Structural Thermodynamics in Halide Perovskites. *ACS Energy Letters*. American Chemical Society April 14, 2023, pp 1705–1715. https://doi.org/10.1021/acsenergylett.2c02698.

(78) Boyd, R. H.; Pant, P. V. K. *Molecular Packing and Diffusion in Polyisobutylene*; 1991; Vol. 24. https://pubs.acs.org/sharingguidelines.

(79) Kempe, M. D.; Nobles, D. L.; Postak, L.; Calderon, J. A. Moisture Ingress Prediction in Polyisobutylene-Based Edge Seal with Molecular Sieve Desiccant. *Progress in Photovoltaics: Research and Applications* **2018**, *26* (2), 93–101. https://doi.org/10.1002/pip.2947.

(80) Liu, Y.; Banon, J. P.; Frohna, K.; Chiang, Y. H.; Tumen-Ulzii, G.; Stranks, S. D.; Filoche, M.; Friend, R. H. The Electronic Disorder Landscape of Mixed Halide Perovskites. *ACS Energy Lett* **2023**, *8* (1), 250–258. https://doi.org/10.1021/acsenergylett.2c02352.

(81) Zeiske, S.; Sandberg, O. J.; Zarrabi, N.; Wolff, C. M.; Raoufi, M.; Peña-Camargo, F.; Gutierrez-Partida, E.; Meredith, P.; Stolterfoht, M.; Armin, A. Static Disorder in Lead Halide Perovskites. *Journal of Physical Chemistry Letters* **2022**, *13* (31), 7280–7285. https://doi.org/10.1021/acs.jpclett.2c01652.

(82) Stoddard, R. J.; Dunlap-Shohl, W. A.; Qiao, H.; Meng, Y.; Kau, W. F.; Hillhouse, H. W. Forecasting the Decay of Hybrid Perovskite Performance Using Optical Transmittance or Reflected Dark-Field Imaging. *ACS Energy Lett* **2020**, *5* (3), 946–954. https://doi.org/10.1021/acsenergylett.0c00164.

(83) Braly, I. L.; Stoddard, R. J.; Rajagopal, A.; Jen, A. K. Y.; Hillhouse, H. W. Photoluminescence and Photoconductivity to Assess Maximum Open-Circuit Voltage and Carrier Transport in Hybrid Perovskites and Other Photovoltaic Materials. *Journal of Physical Chemistry Letters*. American Chemical Society July 5, 2018, pp 3779–3792. https://doi.org/10.1021/acs.jpclett.8b01152.

(84) Aristidou, N.; Eames, C.; Sanchez-Molina, I.; Bu, X.; Kosco, J.; Saiful Islam, M.; Haque, S. A. Fast Oxygen Diffusion and Iodide Defects Mediate Oxygen-Induced Degradation of Perovskite Solar Cells. *Nat Commun* **2017**, *8*. https://doi.org/10.1038/ncomms15218.

(85) Aristidou, N.; Sanchez-Molina, I.; Chotchuangchutchaval, T.; Brown, M.; Martinez, L.; Rath, T.; Haque, S. A. The Role of Oxygen in the Degradation of Methylammonium Lead Trihalide Perovskite Photoactive Layers. *Angewandte Chemie* **2015**, *127* (28), 8326–8330. https://doi.org/10.1002/ange.201503153.

(86) Iqbal, A. N.; Orr, K. W. P.; Nagane, S.; Orri, J. F.; Doherty, T. A. S.; Jung, Y.; Chiang, Y.; Selby, T. A.; Lu, Y.; Mirabelli, A. J.; Baldwin, A.; Ooi, Z. Y.; Gu, Q.; Anaya, M.; Stranks, S. D. Composition Dictates Octahedral Tilt and Photostability in Halide Perovskites. *Advanced Materials* **2024**. https://doi.org/10.1002/adma.202307508.

(87) Dunlap-Shohl, W. A.; Meng, Y.; Sunkari, P. P.; Beck, D. A. C.; Meilă, M.; Hillhouse, H. W. Physiochemical Machine Learning Models Predict Operational Lifetimes of $CH_3NH_3PbI_3$ Perovskite Solar Cells. *J Mater Chem A Mater* **2024**, *12* (16), 9730–9746. https://doi.org/10.1039/D3TA06668A.

(88) Taddei, M.; Smith, J. A.; Gallant, B. M.; Zhou, S.; Westbrook, R. J. E.; Shi, Y.; Wang, J.; Drysdale, J. N.; McCarthy, D. P.; Barlow, S.; Marder, S. R.; Snaith, H. J.; Ginger, D. S. Ethylenediamine Addition Improves Performance and Suppresses Phase Instabilities in Mixed-Halide Perovskites. *ACS Energy Lett* **2022**, *7* (12), 4265–4273. https://doi.org/10.1021/acsenergylett.2c01998.

(89) Martani, S.; Zhou, Y.; Poli, I.; Aktas, E.; Meggiolaro, D.; Jiménez-López, J.; Wong, E. L.; Gregori, L.; Prato, M.; Di Girolamo, D.; Abate, A.; De Angelis, F.; Petrozza, A. Defect Engineering to Achieve Photostable Wide Bandgap Metal Halide Perovskites. *ACS Energy Lett* **2023**, *8* (6), 2801–2808. https://doi.org/10.1021/acsenergylett.3c00610.

(90) Senanayak, S. P.; Dey, K.; Shivanna, R.; Li, W.; Ghosh, D.; Zhang, Y.; Roose, B.; Zelewski, S. J.; Andaji-Garmaroudi, Z.; Wood, W.; Tiwale, N.; MacManus-Driscoll, J. L.; Friend, R. H.; Stranks, S. D.; Sirringhaus, H. Charge Transport in Mixed Metal Halide Perovskite Semiconductors. *Nat Mater* **2023**, *22* (2), 216–224. https://doi.org/10.1038/s41563-022-01448-2.

(91) Dey, K.; Ghosh, D.; Pilot, M.; Pering, S. R.; Roose, B.; Deswal, P.; Senanayak, S. P.; Cameron, P. J.; Islam, M. S.; Stranks, S. D. Substitution of Lead with Tin Suppresses Ionic Transport in Halide Perovskite Optoelectronics. *Energy Environ Sci* **2023**, *17* (2), 760–769. https://doi.org/10.1039/d3ee03772j.

(92) Fu, F.; Pisoni, S.; Jeangros, Q.; Sastre-Pellicer, J.; Kawecki, M.; Paracchino, A.; Moser, T.; Werner, J.; Andres, C.; Duchêne, L.; Fiala, P.; Rawlence, M.; Nicolay, S.; Ballif, C.; Tiwari, A. N.; Buecheler, S. I2 Vapor-Induced Degradation of Formamidinium Lead Iodide Based Perovskite Solar Cells under Heat-Light Soaking Conditions. *Energy Environ Sci* **2019**, *12* (10), 3074–3088. https://doi.org/10.1039/c9ee02043h.

(93) Wang, S.; Jiang, Y.; Juarez-Perez, E. J.; Ono, L. K.; Qi, Y. Accelerated Degradation of Methylammonium Lead Iodide Perovskites Induced by Exposure to Iodine Vapour. *Nat Energy* **2017**, *2* (1). https://doi.org/10.1038/nenergy.2016.195.

(94) Schellenberg, J. J. J.; Kao, K. C. C. On the Relationship between Photoconductivity and Light Intensity in Solids. *J. Phys. D: Appl. Phys* **1988**, *21*, 1764–1768.

(95) Juarez-Perez, E. J.; Ono, L. K.; Qi, Y. Thermal Degradation of Formamidinium Based Lead Halide Perovskites into: Sym -Triazine and Hydrogen Cyanide Observed by Coupled

Thermogravimetry-Mass Spectrometry Analysis. *J Mater Chem A Mater* **2019**, *7* (28), 16912–16919. https://doi.org/10.1039/c9ta06058h.

(96) Cira, S. G.; Meng, Y.; Sunkari, P. P.; Hillhouse, H. W. Photooxidation Reaction Kinetics of Mixed-Cation Mixed-Halide Perovskite. *J Mater Chem A Mater* **2025**, *13* (44), 38436–38445. https://doi.org/10.1039/D5TA05228A.

(97) Abzieher, T.; Moore, D. T.; Roß, M.; Albrecht, S.; Silvia, J.; Tan, H.; Jeangros, Q.; Ballif, C.; Hoerantner, M. T.; Kim, B. S.; Bolink, H. J.; Pistor, P.; Goldschmidt, J. C.; Chiang, Y. H.; Stranks, S. D.; Borchert, J.; McGehee, M. D.; Morales-Masis, M.; Patel, J. B.; Bruno, A.; Paetzold, U. W. Vapor Phase Deposition of Perovskite Photovoltaics: Short Track to Commercialization? *Energy and Environmental Science*. Royal Society of Chemistry January 23, 2024, pp 1645–1663. https://doi.org/10.1039/d3ee03273f.

(98) Eperon, G. E.; Stranks, S. D.; Menelaou, C.; Johnston, M. B.; Herz, L. M.; Snaith, H. J. Formamidinium Lead Trihalide: A Broadly Tunable Perovskite for Efficient Planar Heterojunction Solar Cells. *Energy Environ Sci* **2014**, *7* (3), 982–988. https://doi.org/10.1039/c3ee43822h.

(99) Mahesh, S.; Ball, J. M.; Oliver, R. D. J.; McMeekin, D. P.; Nayak, P. K.; Johnston, M. B.; Snaith, H. J. Revealing the Origin of Voltage Loss in Mixed-Halide Perovskite Solar Cells. *Energy Environ Sci* **2020**, *13* (1), 258–267. https://doi.org/10.1039/c9ee02162k.

(100) Knight, A. J.; Herz, L. M. Preventing Phase Segregation in Mixed-Halide Perovskites: A Perspective. *Energy and Environmental Science*. Royal Society of Chemistry July 1, 2020, pp 2024–2046. https://doi.org/10.1039/d0ee00788a.

(101) Köhnen, E.; Jošt, M.; Morales-Vilches, A. B.; Tockhorn, P.; Al-Ashouri, A.; Macco, B.; Kegelmann, L.; Korte, L.; Rech, B.; Schlatmann, R.; Stannowski, B.; Albrecht, S. Highly Efficient Monolithic Perovskite Silicon Tandem Solar Cells: Analyzing the Influence of Current Mismatch on Device Performance. *Sustain Energy Fuels* **2019**, *3* (8), 1995–2005. https://doi.org/10.1039/c9se00120d.

(102) Tan, W.; Bowring, A. R.; Meng, A. C.; McGehee, M. D.; McIntyre, P. C. Thermal Stability of Mixed Cation Metal Halide Perovskites in Air. *ACS Appl Mater Interfaces* **2018**, *10* (6), 5485–5491. https://doi.org/10.1021/acsami.7b15263.

(103) Pool, V. L.; Dou, B.; Van Campen, D. G.; Klein-Stockert, T. R.; Barnes, F. S.; Shaheen, S. E.; Ahmad, M. I.; Van Hest, M. F. A. M.; Toney, M. F. Thermal Engineering of FAPbI3 Perovskite Material via Radiative Thermal Annealing and in Situ XRD. *Nat Commun* **2017**, *8*. https://doi.org/10.1038/ncomms14075.

(104) De Keersmaecker, M.; Dietrich, P.; Bahri, M.; Browning, N. D.; Armstrong, N. R.; Ratcliff, E. L. Activated Corrosion and Recovery in Lead Mixed-Halide Perovskites Revealed by Dynamic Near-Ambient Pressure X-Ray Photoelectron Spectroscopy. *J Am Chem Soc* **2025**. https://doi.org/10.1021/jacs.5c00668.

(105) Chen, Z.; Yang, Z.; Du, S.; Lin, D.; Zhang, F.; Zeng, Y.; Liu, G.; Nie, Z.; Ma, L. Thermal Stability and Decomposition Kinetics of Mixed-Cation Halide Perovskites. *Physical Chemistry Chemical Physics* **2023**, *25* (48), 32966–32971. https://doi.org/10.1039/d3cp03704e.

(106) Repins, I. L.; Owen-Bellini, M.; Kempe, M. D.; Deceglie, M. G.; Berry, J. J.; Doumon, N. Y.; Silverman, T. J.; Schelhas, L. T. Interpreting Accelerated Tests on Perovskite Modules Using Photooxidation of MAPbI3 as an Example. *Cell Rep Phys Sci* **2024**, *5* (5), 101969. https://doi.org/10.1016/j.xcrp.2024.101969.

(107) Ju, Y.; Hu, X.; Wu, X. gang; Wang, C.; Baranov, A.; Pushkarev, A.; Zhong, H. The Interactions between Halide Perovskites and Oxygen: From Stages to Strategies. *Matter*. Cell Press November 6, 2024, pp 3756–3785. https://doi.org/10.1016/j.matt.2024.08.007.
(108) Aristidou, N.; Sanchez-Molina, I.; Chotchuangchutchaval, T.; Brown, M.; Martinez, L.; Rath, T.; Haque, S. A. The Role of Oxygen in the Degradation of Methylammonium Lead Trihalide Perovskite Photoactive Layers. *Angewandte Chemie* **2015**, *127* (28), 8326–8330. https://doi.org/10.1002/ange.201503153.
(109) Hidalgo, J.; Kaiser, W.; An, Y.; Li, R.; Oh, Z.; Castro-Méndez, A. F.; LaFollette, D. K.; Kim, S.; Lai, B.; Breternitz, J.; Schorr, S.; Perini, C. A. R.; Mosconi, E.; De Angelis, F.; Correa-Baena, J. P. Synergistic Role of Water and Oxygen Leads to Degradation in Formamidinium-Based Halide Perovskites. *J Am Chem Soc* **2023**. https://doi.org/10.1021/jacs.3c05657.
(110) Raval, P.; Akhavan Kazemi, M. A.; Ruellou, J.; Trébosc, J.; Lafon, O.; Delevoye, L.; Sauvage, F.; Manjunatha Reddy, G. N. Examining a Year-Long Chemical Degradation Process and Reaction Kinetics in Pristine and Defect-Passivated Lead Halide Perovskites. *Chemistry of Materials* **2023**, *35* (7), 2904–2917. https://doi.org/10.1021/acs.chemmater.2c03803.
(111) Kim, H. S.; Lee, C. R.; Im, J. H.; Lee, K. B.; Moehl, T.; Marchioro, A.; Moon, S. J.; Humphry-Baker, R.; Yum, J. H.; Moser, J. E.; Grätzel, M.; Park, N. G. Lead Iodide Perovskite Sensitized All-Solid-State Submicron Thin Film Mesoscopic Solar Cell with Efficiency Exceeding 9%. *Sci Rep* **2012**, *2*. https://doi.org/10.1038/srep00591.
(112) Ouyang, Y.; Li, Y.; Zhu, P.; Li, Q.; Gao, Y.; Tong, J.; Shi, L.; Zhou, Q.; Ling, C.; Chen, Q.; Deng, Z.; Tan, H.; Deng, W.; Wang, J. Photo-Oxidative Degradation of Methylammonium Lead Iodide Perovskite: Mechanism and Protection. *J Mater Chem A Mater* **2019**, *7* (5), 2275–2282. https://doi.org/10.1039/c8ta12193a.
(113) Bryant, D.; Aristidou, N.; Pont, S.; Sanchez-Molina, I.; Chotchunangatchaval, T.; Wheeler, S.; Durrant, J. R.; Haque, S. A. Light and Oxygen Induced Degradation Limits the Operational Stability of Methylammonium Lead Triiodide Perovskite Solar Cells. *Energy Environ Sci* **2016**, *9* (5), 1655–1660. https://doi.org/10.1039/c6ee00409a.
(114) Sun, Q.; Fassl, P.; Becker-Koch, D.; Bausch, A.; Rivkin, B.; Bai, S.; Hopkinson, P. E.; Snaith, H. J.; Vaynzof, Y. Role of Microstructure in Oxygen Induced Photodegradation of Methylammonium Lead Triiodide Perovskite Films. *Adv Energy Mater* **2017**, *7* (20). https://doi.org/10.1002/aenm.201700977.
(115) Webb, T.; Haque, S. A. A Comparison of Molecular Iodine Evolution on the Chemistry of Lead and Tin Perovskites. *Energy and Environmental Science*. Royal Society of Chemistry April 24, 2024, pp 3244–3269. https://doi.org/10.1039/d3ee03004k.
(116) Kotz, S.; Johnson, N. L. *Breakthroughs in Statistics: Methodology and Distribution*; Springer: New York, 1992.
(117) Zhang, L.; Sit, P. H. L. Ab Initio Study of Interaction of Water, Hydroxyl Radicals, and Hydroxide Ions with CH3NH3PbI3 and CH3NH3PbBr3 Surfaces. *Journal of Physical Chemistry C* **2015**, *119* (39), 22370–22378. https://doi.org/10.1021/acs.jpcc.5b07000.
(118) Zhang, L.; Sit, P. H. L. Ab Initio Static and Dynamic Study of CH3NH3PbI3 Degradation in the Presence of Water, Hydroxyl Radicals, and Hydroxide Ions. *RSC Adv* **2016**, *6* (80), 76938–76947. https://doi.org/10.1039/c6ra12781a.

(119) McAndrews, G. R.; Guo, B.; Kaczaral, S. C.; Fukuda, K.; Poma, M. R. S.; Belisle, R. A.; Amassian, A.; McGehee, M. D. Moisture Uptake Relaxes Stress in Metal Halide Perovskites at the Expense of Stability. *ACS Energy Lett* **2024**, *9* (8), 4153–4161. https://doi.org/10.1021/acsenergylett.4c01817.

(120) Chin, D.-H.; Chiericato, G.; Nanni, E. J.; Sawyer, D. T. Proton-Induced Disproportionation of Superoxide Ion in Aprotic Media. *J. Am. Chem. Soc.* **1982**, *104* (104), 1296–1299.

(121) Leguy, A. M. A.; Hu, Y.; Campoy-Quiles, M.; Alonso, M. I.; Weber, O. J.; Azarhoosh, P.; Van Schilfgaarde, M.; Weller, M. T.; Bein, T.; Nelson, J.; Docampo, P.; Barnes, P. R. F. Reversible Hydration of CH3NH3PbI3 in Films, Single Crystals, and Solar Cells. *Chemistry of Materials* **2015**, *27* (9), 3397–3407. https://doi.org/10.1021/acs.chemmater.5b00660.

(122) Zhu, Z.; Hadjiev, V. G.; Rong, Y.; Guo, R.; Cao, B.; Tang, Z.; Qin, F.; Li, Y.; Wang, Y.; Hao, F.; Venkatesan, S.; Li, W.; Baldelli, S.; Guloy, A. M.; Fang, H.; Hu, Y.; Yao, Y.; Wang, Z.; Bao, J. Interaction of Organic Cation with Water Molecule in Perovskite MAPbI3: From Dynamic Orientational Disorder to Hydrogen Bonding. *Chemistry of Materials* **2016**, *28* (20), 7385–7393. https://doi.org/10.1021/acs.chemmater.6b02883.

(123) Cao, J.; Zhang, X.; Miao, Y.; Li, W.; Zeng, X.; Yang, S.; Yan, C.; Lu, J.; Yang, W. Interactions between H2O and Lead Halide Perovskites: Recent Progress and Applications. *Matter*. Cell Press November 6, 2024, pp 3728–3755. https://doi.org/10.1016/j.matt.2024.08.001.

(124) Hu, L.; Shao, G.; Jiang, T.; Li, D.; Lv, X.; Wang, H.; Liu, X.; Song, H.; Tang, J.; Liu, H. Investigation of the Interaction between Perovskite Films with Moisture via in Situ Electrical Resistance Measurement. *ACS Appl Mater Interfaces* **2015**, *7* (45), 25113–25120. https://doi.org/10.1021/acsami.5b06268.

(125) Yang, J.; Siempelkamp, B. D.; Liu, D.; Kelly, T. L. Investigation of CH3NH3PbI3degradation Rates and Mechanisms in Controlled Humidity Environments Using in Situ Techniques. *ACS Nano* **2015**, *9* (2), 1955–1963. https://doi.org/10.1021/nn506864k.

(126) Zhang, L.; Ju, M. G.; Liang, W. The Effect of Moisture on the Structures and Properties of Lead Halide Perovskites: A First-Principles Theoretical Investigation. *Physical Chemistry Chemical Physics* **2016**, *18* (33), 23174–23183. https://doi.org/10.1039/c6cp01994c.

(127) Ma, C.; Felix, †; Eickemeyer, T.; Lee, † Sun-Ho; Kang, D.-H.; Kwon, S. J.; Grätzel, M.; Park, N.-G. *Unveiling Facet-Dependent Degradation and Facet Engineering for Stable Perovskite Solar Cells*. https://www.science.org.

(128) Hastie, T.; Tibshirani, R.; Friedman, J. *The Elements of Statistical Learning: Data Mining, Inference, and Prediction*; Springer: New York, 2017.

(129) Hieulle, J.; Krishna, A.; Boziki, A.; Audinot, J. N.; Farooq, M. U.; Machado, J. F.; Mladenović, M.; Phirke, H.; Singh, A.; Wirtz, T.; Tkatchenko, A.; Graetzel, M.; Hagfeldt, A.; Redinger, A. Understanding and Decoupling the Role of Wavelength and Defects in Light-Induced Degradation of Metal-Halide Perovskites. *Energy Environ Sci* **2023**, *17* (1), 284–295. https://doi.org/10.1039/d3ee03511e.

(130) Ouyang, Y.; Li, Y.; Zhu, P.; Li, Q.; Gao, Y.; Tong, J.; Shi, L.; Zhou, Q.; Ling, C.; Chen, Q.; Deng, Z.; Tan, H.; Deng, W.; Wang, J. Photo-Oxidative Degradation of Methylammonium

Lead Iodide Perovskite: Mechanism and Protection. *J Mater Chem A Mater* **2019**, *7* (5), 2275–2282. https://doi.org/10.1039/c8ta12193a.

(131) Cheng, S.; Zhong, H. What Happens When Halide Perovskites Meet with Water? *Journal of Physical Chemistry Letters*. American Chemical Society March 17, 2022, pp 2281–2290. https://doi.org/10.1021/acs.jpclett.2c00166.

(132) Jong, U. G.; Yu, C. J.; Ri, G. C.; McMahon, A. P.; Harrison, N. M.; Barnes, P. R. F.; Walsh, A. Influence of Water Intercalation and Hydration on Chemical Decomposition and Ion Transport in Methylammonium Lead Halide Perovskites. *J Mater Chem A Mater* **2018**, *6* (3), 1067–1074. https://doi.org/10.1039/c7ta09112e.

(133) Zhang, W.; Xiong, J.; Li, J.; Daoud, W. A. Impact of Temperature-Dependent Hydration Water on Perovskite Solar Cells. *Solar RRL* **2020**, *4* (1). https://doi.org/10.1002/solr.201900370.

(134) Stranks, S. D.; Snaith, H. J. Metal-Halide Perovskites for Photovoltaic and Light-Emitting Devices. *Nature Nanotechnology*. Nature Publishing Group May 7, 2015, pp 391–402. https://doi.org/10.1038/nnano.2015.90.

(135) Braly, I. L.; Dequilettes, D. W.; Pazos-Outón, L. M.; Burke, S.; Ziffer, M. E.; Ginger, D. S.; Hillhouse, H. W. Hybrid Perovskite Films Approaching the Radiative Limit with over 90% Photoluminescence Quantum Efficiency. *Nat Photonics* **2018**, *12* (6), 355–361. https://doi.org/10.1038/s41566-018-0154-z.

(136) Li, Z.; Klein, T. R.; Kim, D. H.; Yang, M.; Berry, J. J.; Van Hest, M. F. A. M.; Zhu, K. Scalable Fabrication of Perovskite Solar Cells. *Nature Reviews Materials*. Nature Publishing Group March 27, 2018. https://doi.org/10.1038/natrevmats.2018.17.

(137) Kojima, A.; Teshima, K.; Shirai, Y.; Miyasaka, T. Organometal Halide Perovskites as Visible-Light Sensitizers for Photovoltaic Cells. *J Am Chem Soc* **2009**, *131* (17), 6050–6051. https://doi.org/10.1021/ja809598r.

(138) Koh, T. M.; Fu, K.; Fang, Y.; Chen, S.; Sum, T. C.; Mathews, N.; Mhaisalkar, S. G.; Boix, P. P.; Baikie, T. Formamidinium-Containing Metal-Halide: An Alternative Material for near-IR Absorption Perovskite Solar Cells. *Journal of Physical Chemistry C* **2014**, *118* (30), 16458–16462. https://doi.org/10.1021/jp411112k.

(139) Jeon, N. J.; Noh, J. H.; Yang, W. S.; Kim, Y. C.; Ryu, S.; Seo, J.; Seok, S. Il. Compositional Engineering of Perovskite Materials for High-Performance Solar Cells. *Nature* **2015**, *517* (7535), 476–480. https://doi.org/10.1038/nature14133.

(140) Mcmeekin, D. P.; Sadoughi, G.; Rehman, W.; Eperon, G. E.; Saliba, M.; Hörantner, M. T.; Haghighirad, A.; Sakai, N.; Korte, L.; Rech, B.; Johnston, M. B.; Herz, L. M.; Snaith, H. J. *A Mixed-Cation Lead Mixed-Halide Perovskite Absorber for Tandem Solar Cells*. https://www.science.org.

(141) Braly, I. L.; Hillhouse, H. W. Optoelectronic Quality and Stability of Hybrid Perovskites from MAPbI3 to MAPbI2Br Using Composition Spread Libraries. *Journal of Physical Chemistry C* **2016**, *120* (2), 893–902. https://doi.org/10.1021/acs.jpcc.5b10728.

(142) Beal, R. E.; Slotcavage, D. J.; Leijtens, T.; Bowring, A. R.; Belisle, R. A.; Nguyen, W. H.; Burkhard, G. F.; Hoke, E. T.; McGehee, M. D. Cesium Lead Halide Perovskites with Improved Stability for Tandem Solar Cells. *Journal of Physical Chemistry Letters* **2016**, *7* (5), 746–751. https://doi.org/10.1021/acs.jpclett.6b00002.

(143) Rajagopal, A.; Stoddard, R. J.; Jo, S. B.; Hillhouse, H. W.; Jen, A. K. Y. Overcoming the Photovoltage Plateau in Large Bandgap Perovskite Photovoltaics. *Nano Lett* **2018**, *18* (6), 3985–3993. https://doi.org/10.1021/acs.nanolett.8b01480.
(144) Stoddard, R. J.; Rajagopal, A.; Palmer, R. L.; Braly, I. L.; Jen, A. K. Y.; Hillhouse, H. W. Enhancing Defect Tolerance and Phase Stability of High-Bandgap Perovskites via Guanidinium Alloying. *ACS Energy Lett* **2018**, *3* (6), 1261–1268. https://doi.org/10.1021/acsenergylett.8b00576.
(145) Zhou, Y.; Poli, I.; Meggiolaro, D.; De Angelis, F.; Petrozza, A. Defect Activity in Metal Halide Perovskites with Wide and Narrow Bandgap. *Nature Reviews Materials*. Nature Research November 1, 2021, pp 986–1002. https://doi.org/10.1038/s41578-021-00331-x.
(146) Meggiolaro, D.; Motti, S. G.; Mosconi, E.; Barker, A. J.; Ball, J.; Andrea Riccardo Perini, C.; Deschler, F.; Petrozza, A.; De Angelis, F. Iodine Chemistry Determines the Defect Tolerance of Lead-Halide Perovskites. *Energy Environ Sci* **2018**, *11* (3), 702–713. https://doi.org/10.1039/c8ee00124c.
(147) Zhao, X.; Lu, H.; Fang, W. H.; Long, R. Correlated Organic-Inorganic Motion Enhances Stability and Charge Carrier Lifetime in Mixed Halide Perovskites. *Nanoscale* **2022**, *14* (12), 4644. https://doi.org/10.1039/d1nr07732e.
(148) Johnston, A.; Walters, G.; Saidaminov, M. I.; Huang, Z.; Bertens, K.; Jalarvo, N.; Sargent, E. H. Bromine Incorporation and Suppressed Cation Rotation in Mixed-Halide Perovskites. *ACS Nano* **2020**, *14* (11), 15107–15118. https://doi.org/10.1021/acsnano.0c05179.
(149) Furlan, F.; Nodari, D.; Palladino, E.; Angela, E.; Mohan, L.; Briscoe, J.; Fuchter, M. J.; Macdonald, T. J.; Grancini, G.; McLachlan, M. A.; Gasparini, N. Tuning Halide Composition Allows Low Dark Current Perovskite Photodetectors With High Specific Detectivity. *Adv Opt Mater* **2022**, *10* (24). https://doi.org/10.1002/adom.202201816.
(150) Yang, M.; Zhang, T.; Schulz, P.; Li, Z.; Li, G.; Kim, D. H.; Guo, N.; Berry, J. J.; Zhu, K.; Zhao, Y. Facile Fabrication of Large-Grain CH3 NH3 PbI3-x Brx Films for High-Efficiency Solar Cells via CH3NH3 Br-Selective Ostwald Ripening. *Nat Commun* **2016**, *7*. https://doi.org/10.1038/ncomms12305.
(151) Hidalgo, J.; Breternitz, J.; Többens, D. M.; LaFollette, D. K.; Pedorella, C. N. B.; Sher, M. J.; Schorr, S.; Correa-Baena, J. P. Br-Induced Suppression of Low-Temperature Phase Transitions in Mixed-Cation Mixed-Halide Perovskites. *Chemistry of Materials* **2024**, *36* (20), 10167–10175. https://doi.org/10.1021/acs.chemmater.4c01670.
(152) LaFollette, D. K.; Hidalgo, J.; Allam, O.; Yang, J.; Shoemaker, A.; Li, R.; Lai, B.; Lawrie, B.; Kalinin, S.; Perini, C. A. R.; Ahmadi, M.; Jang, S. S.; Correa-Baena, J. P. Bromine Incorporation Affects Phase Transformations and Thermal Stability of Lead Halide Perovskites. *J Am Chem Soc* **2024**, *146* (27), 18576–18585. https://doi.org/10.1021/jacs.4c04508.
(153) Xu, Z.; Zhong, X.; Hu, T.; Hu, J.; Kahn, A.; Rand, B. P. Correlating Halide Segregation with Photolysis in Mixed-Halide Perovskites via In Situ Opto-Gravimetric Analysis. *J Am Chem Soc* **2024**. https://doi.org/10.1021/jacs.4c08939.
(154) Frolova, L. A.; Luchkin, S. Y.; Lekina, Y.; Gutsev, L. G.; Tsarev, S. A.; Zhidkov, I. S.; Kurmaev, E. Z.; Shen, Z. X.; Stevenson, K. J.; Aldoshin, S. M.; Troshin, P. A. Reversible Pb2+/Pb0 and I−/I3− Redox Chemistry Drives the Light-Induced Phase Segregation in

All-Inorganic Mixed Halide Perovskites. *Adv Energy Mater* **2021**, *11* (12). https://doi.org/10.1002/aenm.202002934.

(155) Abdelhady, A. L.; Afraj, S. N.; Haruta, Y.; Uddin, M. M.; Saidaminov, M. I. Metallic Lead Formation in Perovskites: Mechanisms, Suppression, and Future Directions. *ACS Nano* **2025**. https://doi.org/10.1021/acsnano.5c11320.

(156) Jošt, M.; Lipovšek, B.; Glažar, B.; Al-Ashouri, A.; Brecl, K.; Matič, G.; Magomedov, A.; Getautis, V.; Topič, M.; Albrecht, S. Perovskite Solar Cells Go Outdoors: Field Testing and Temperature Effects on Energy Yield. *Adv Energy Mater* **2020**, *10* (25). https://doi.org/10.1002/aenm.202000454.

(157) Jiang, Q.; Tirawat, R.; Kerner, R. A.; Gaulding, E. A.; Xian, Y.; Wang, X.; Newkirk, J. M.; Yan, Y.; Berry, J. J.; Zhu, K. Towards Linking Lab and Field Lifetimes of Perovskite Solar Cells. *Nature* **2023**, *623* (7986), 313–318. https://doi.org/10.1038/s41586-023-06610-7.

(158) Motti, S. G.; Meggiolaro, D.; Barker, A. J.; Mosconi, E.; Perini, C. A. R.; Ball, J. M.; Gandini, M.; Kim, M.; De Angelis, F.; Petrozza, A. Controlling Competing Photochemical Reactions Stabilizes Perovskite Solar Cells. *Nat Photonics* **2019**, *13* (8), 532–539. https://doi.org/10.1038/s41566-019-0435-1.

(159) Zhou, Y.; van Laar, S. C. W.; Meggiolaro, D.; Gregori, L.; Martani, S.; Heng, J. Y.; Datta, K.; Jiménez-López, J.; Wang, F.; Wong, E. L.; Poli, I.; Treglia, A.; Cortecchia, D.; Prato, M.; Kobera, L.; Gao, F.; Zhao, N.; Janssen, R. A. J.; De Angelis, F.; Petrozza, A. How Photogenerated I2 Induces I-Rich Phase Formation in Lead Mixed Halide Perovskites. *Advanced Materials* **2024**, *36* (1). https://doi.org/10.1002/adma.202305567.

(160) Zhou, Y.; Wong, E. L.; Folpini, G.; Zanolini, M.; Jiménez-López, J.; Treglia, A.; Petrozza, A. Mutual Destabilization of Wide Bandgap Perovskite and PbI2 Inclusions through Interface Carrier Trapping. *Adv Funct Mater* **2024**. https://doi.org/10.1002/adfm.202406317.

(161) Sidhik, S.; Metcalf, I.; Li, W.; Kodalle, T.; Dolan, C. J.; Khalili, M.; Hou, J.; Mandani, F.; Torma, A.; Zhang, H.; Garai, R.; Persaud, J.; Marciel, A.; Alejandra Muro Puente, I.; Manjunatha Reddy, G. N.; Balvanz, A.; Alam, M. A.; Katan, C.; Tsai, E.; Ginger, D.; Fenning, D. P.; Kanatzidis, M. G.; Sutter-Fella, C. M.; Even, J.; Mohite, A. D. *Two-Dimensional Perovskite Templates for Durable, Efficient Formamidinium Perovskite Solar Cells*; 2025. https://www.science.org.

(162) Zhang, Y.; Chen, Y.; Liu, G.; Wu, Y.; Guo, Z.; Fan, R.; Li, K.; Liu, H.; Zhao, Y.; Kodalle, T.; Chen, Y.; Zhu, C.; Bai, Y.; Chen, Q.; Zhou, H. *Nonalloyed A-Phase Formamidinium Lead Triiodide Solar Cells through Iodine Intercalation*. https://www.science.org.

(163) Jain, A.; Ong, S. P.; Hautier, G.; Chen, W.; Richards, W. D.; Dacek, S.; Cholia, S.; Gunter, D.; Skinner, D.; Ceder, G.; Persson, K. A. Commentary: The Materials Project: A Materials Genome Approach to Accelerating Materials Innovation. *APL Materials*. American Institute of Physics Inc. 2013. https://doi.org/10.1063/1.4812323.

(164) Vaitkus, A.; Merkys, A.; Sander, T.; Quirós, M.; Thiessen, P. A.; Bolton, E. E.; Gražulis, S. A Workflow for Deriving Chemical Entities from Crystallographic Data and Its Application to the Crystallography Open Database. *J Cheminform* **2023**, *15* (1). https://doi.org/10.1186/s13321-023-00780-2.

(165) Li, H.; Petrozza, A. Long-Term Stability Hurdles of Metal Halide Perovskite Solar Cells. *ACS Energy Lett* **2025**, *10* (9), 4572–4573. https://doi.org/10.1021/acsenergylett.5c02513.

(166) Li, N.; Niu, X.; Chen, Q.; Zhou, H. Towards Commercialization: The Operational Stability of Perovskite Solar Cells. *Chemical Society Reviews*. Royal Society of Chemistry November 21, 2020, pp 8235–8286. https://doi.org/10.1039/d0cs00573h.
(167) Hardy, J.; Fiedler, H.; Kennedy, J. A Review on the Current Status and Chemistry of Tin Halide Perovskite Films for Photovoltaics. *Progress in Materials Science*. Elsevier Ltd May 1, 2025. https://doi.org/10.1016/j.pmatsci.2025.101446.
(168) Li, Q.; Zheng, Y.; Wang, H.; Liu, X.; Lin, M.; Sui, X.; Leng, X.; Liu, D.; Wei, Z.; Song, M.; Li, D.; Yang, H. G.; Yang, S.; Hou, Y. *Graphene-Polymer Reinforcement of Perovskite Lattices for Durable Solar Cells*. https://www.science.org.
(169) Zai, H.; Yang, P.; Su, J.; Yin, R.; Fan, R.; Wu, Y.; Zhu, X.; Ma, Y.; Zhou, T.; Zhou, W.; Zhang, Y.; Huang, Z.; Jiang, Y.; Li, N.; Bai, Y.; Zhu, C.; Huang, Z.; Chang, J.; Chen, Q.; Zhang, Y.; Zhou, H. *Wafer-Scale Monolayer MoS 2 Film Integration for Stable, Efficient Perovskite Solar Cells*. https://www.science.org.
(170) Liu, C.; Yang, Y.; Chen, H.; Spanopoulos, I.; Bati, A. S. R.; Gilley, I. W.; Chen, J.; Maxwell, A.; Vishal, B.; Reynolds, R. P.; Wiggins, T. E.; Wang, Z.; Huang, C.; Fletcher, J.; Liu, Y.; Chen, L. X.; De Wolf, S.; Chen, B.; Zheng, D.; Marks, T. J.; Facchetti, A.; Sargent, E. H.; Kanatzidis, M. G. Two-Dimensional Perovskitoids Enhance Stability in Perovskite Solar Cells. *Nature* **2024**, *633* (8029), 359–364. https://doi.org/10.1038/s41586-024-07764-8.
(171) Wang, H.; Su, S.; Chen, Y.; Ren, M.; Wang, S.; Wang, Y.; Zhu, C.; Miao, Y.; Ouyang, C.; Zhao, Y. Impurity-Healing Interface Engineering for Efficient Perovskite Submodules. *Nature* **2024**, *634* (8036), 1091–1095. https://doi.org/10.1038/s41586-024-08073-w.
(172) Oxford PV. *20% more powerful tandem solar panels enter commercial use for the first time in the US*.